HIGH HARMONIC GENERATION OPTIMIZATION IN ATOMIC AND MOLECULAR GASES

A Dissertation

by

MUHAMMED SAYRAC

Submitted to the Office of Graduate and Professional Studies of
Texas A&M University
in partial fulfillment of the requirements for the degree of

DOCTOR OF PHILOSOPHY

Chair of Committee,	Hans A. Schuessler
Co-Chair of Committee,	Alexandre A. Kolomenskii
Committee Members,	Rainer J. Fries
	Alvin T. Yeh
Head of Department,	Peter McIntyre

May 2017

Major Subject: Physics

ABSTRACT

High harmonic generation (HHG) is a unique process in which atoms/molecules ionized by an intense laser field at frequency ω_0 emit radiation of higher frequencies, which are multiples of frequency ω_0, at much shorter wavelengths ranging from the ultraviolet to the soft x-ray region (XUV region). These so-called high harmonics (HHs) are very promising for spectroscopic and imaging applications since HHs possess high spatial and temporal coherence. Unfortunately, HHG suffers from its low conversion efficiency of the driving radiation (usually in the IR region) to the XUV range.

This dissertation reports experimental works based on the HHG technique. In this work, we present different experimental approaches, which enhance the output of the HHG radiation, i.e. the conversion efficiency. In the first approach, a differentially pumped gas cell is used to control the pressure in the interaction region. This approach allows us to optimize the efficiency of the HHs yield by finding the optimum atomic/molecular density, taking into account also the absorption and phase matching conditions. In the second approach, gas mixtures of Ne with H_2 are investigated to improve the conversion efficiency of the HHs output. In the third approach, an enhancement of HHs radiation in aligned molecules is investigated. In the fourth approach, the enhancement of even and odd harmonics in a two-color laser field is explored. Finally, the application of the XUV radiation, obtained via HHG with the goal to improve the spatial resolution of imaging of the nano- to micron sized structures is presented.

DEDICATION

To my wife, Habibe and my daughter, Zeynep Beril and my son, Mehmet Ali

ACKNOWLEDGEMENTS

I would like to thank my committee chair, Dr. Hans A. Schuessler, and my committee members, Dr. Alexandre A. Kolomenskii, Dr. Rainer J. Fries, and Dr. Alvin T. Yeh for their guidance and support throughout the course of this research.

I would also like to extend my heartfelt gratitude to my co-advisor, Dr. Alexandre A. Kolomenskii for his great assistance, kindness, and consistent encouragement. Especially, I gratefully acknowledge his enthusiasm in explaining and helping with the preparation of my dissertation as well as my scientific papers. I would also like to thank Dr. James Strohaber for detailed discussions and assistance related to the research.

I would like to extend my thanks to all people in Attosecond ad Few Cycle Laser Laboratory, and my fellow graduate students, Necati Kaya, Yakup Boran, Nathan Hart, Sunilkumar Anumula, and Feng Zhu. Thanks also go to the department faculty and staff for making my time at Texas A&M University a great experience. I also want to extend my gratitude for support to the National Science Foundation, Welch Foundation, Qatar Foundation, and the Ministry of National Education of the Republic of Turkey.

I am deeply grateful to my family for their support and love. Finally, I would like to give special thanks to my soul mate, lovely wife and best friend Habibe for coming into my life. Anything good that has come to my life has been because of your example, guidance, and love.

NOMENCLATURE

ATI	above-threshold ionization
CCD	charge-coupled device
HHG	high harmonic generation
fs	femtosecond
FWHM	full width at half maximum
as	attosecond
I	laser beam intensity
ω_0	laser field frequency
λ	laser field wavelength
n_0	linear refractive index
MCP	microchannel plate
n_2	Nonlinear coefficient
τ	pulse duration
XUV	extreme ultra violet

TABLE OF CONTENTS

Page

LIST OF FIGURES

Page

LIST OF TABLES

Page

CHAPTER I

INTRODUCTION

With the application of an intense laser field ($I>10^{13}W/cm^2$), the laser-matter interaction exhibits highly nonlinear dynamics, opening many research areas such as above-threshold ionization (ATI) -absorption of more photons than the minimum number required for ionization [3], high harmonic generation (HHG)- converting coherent light from visible light to EUV and soft X-ray regions [4], and attosecond pulse generation [5]. Therefore, researchers have been aiming to control these dynamical processes of atomic or molecular systems via manipulating the lasers parameters, such as peak intensity [3, 4, 6, 7], pulse width [4, 6, 8, 9], pulse shape [3, 10], or carrier-envelope phase [11-15] to achieve the desired outcome. The understanding of these laser-matter interactions has opened the door to a host of applications, such as data storage, communication, and image processing.

The femtosecond pulses ($1fs=10^{-15}s$), having only few oscillations of the electromagnetic field [16] allow to capture a "snapshot" of the dynamics of atoms and molecules, because the nuclei appear "frozen" at a given internuclear separation for the duration of the pulse [16]. Specifically, very short laser pulses permit the exploration of molecular motion, since many molecular processes occur in the picosecond (1000fs = 1ps) scale, for example, molecular rotations of N_2 and C_2H_2 molecule is around 8.4ps and 14.2ps, respectively [17, 18]. Recent improvement of femtosecond pulse generation [19] has enabled researchers to understand the mechanism of many processes in photochemistry, photobiology, and physics [16, 19]. In 1999, Prof. Ahmed H. Zewail,

(professor of chemical physics, California Institute of Technology) was awarded the Nobel Prize in Chemistry for his research in studying chemical processes [20] on the femtosecond time scale, thereby founding the science of femtochemistry. Moreover, the Nobel Prize in Physics 2005 was divided, one half awarded to Roy J. Glauber for his contribution to the quantum theory of optical coherence [21], and the other half was shared by two experimental physicists, John L. Hall and Theodor W. Hansch [22, 23] for their contributions to the optical frequency comb technique for spectroscopy. It was a challenge to measure the frequency beyond the microwave region (~GHz= 10^9Hz) until the invention of frequency comb technique, since the field oscillation is too fast to count electronically. Today any optical frequencies can be measured with frequency comb technique due to availability of femtosecond laser pulses [24, 25].

On the other hand, the resolution of time domain measurement beyond the sub-femtosecond level due to advances in the field of HHG. HHG is a unique nonlinear process in which atoms/molecules ionized by an intense laser field at frequency ω_0 produces radiations of higher frequencies $q\omega_0$ where q is an odd integer. HHG driven by IR lasers can span a frequency range from UV to soft X-ray regions [26], and the emitted light bursts are in the form of attosecond or even zeptosecond pulses [27, 28]. HHG is usually realized by using amplified femtosecond laser pulses that can be produced from a table top laser systems. For this reason HHG is considered as a major approach of obtaining a table top source of coherent XUV radiation [29].

Conversion efficiencies of HHG of the driving IR laser radiation into its harmonics can be achieved in the range of 10^{-7} – 10^{-5} per harmonic (with harmonic energy reaching

~μJ), when the frequency conversion process is phase matched. Thus, the possibility to generate a high density photon flux is limited by this low conversion efficiency, and it is further exacerbated by the mismatch of phase velocities of the fundamental and harmonic fields and a large absorption/dispersion in the medium [30]. In addition, geometrical phase shift (Gouy phase) arises when the laser beam is focused into gas medium [31]. The above mentioned de-phasing effects set limitations for the efficient harmonic generation.

Many HHG experiments have been done over the last two decades to increase the efficiency of HHs. Different geometries used for HHG were explored, including free-space gas jet [32], gas filled wave guide [26] and more recently, hollow core photonic crystal fibers [33]. In addition, the use of multi colored fields have piqued significant interest due to the potential of these synthesized wave forms to enhance the high harmonic yield [34]. In view of variety of approaches, there are still many open questions concerning the optimal conditions and configurations for the extension of the cutoff energy to the soft X-ray region and enhancing the efficiency of HHG. These questions should be thoroughly investigated in view of numerous possible applications of HHG sources, such as tracking the dynamics of electrons in atoms, molecules, and materials [35-38], nano-bio imaging [39-41], atomic [42] and molecular [43, 44] spectroscopy. Because different applications require light in different spectral regions, x-ray free electron lasers (FEL) [45] based on accelerator physics and synchrotron light sources [46] have been developed over last decades to generate powerful broadband tunable light. However, FEL are extremely expensive and large devices, and HHG is viable alternative offering XUV light source as a table top installation affordable by many individual laboratories. When the intensity of

HH radiation is optimized/enhanced, HHG can offer broadband and bright table top light source with high photon energies.

In this dissertation, we report an experimental study on the generation of high harmonics. The structure of the thesis is as follows. Chapter II is a literature review on HHG technique, and it begins by summarizing the history of HHG. Then, the principles of HHG are discussed, such as semi classical three-step model and macroscopic phase matching effect. The chapter continues with a description of the high power femtosecond laser system and pulse measurement technique (FROG). Finally, the Chapter II is concluded with explanation of the XUV detection system and estimation of the conversion efficiency of the HHs flux. Chapter III presents enhancement of the HHs yield by using a differentially pumped gas cell. Depending on the phase matching conditions the HHs output can be suppressed or enhanced. Chapter IV investigates the effect of the gas mixing (Ne with H_2) on the HHG output, showing that the HHG yield is enhanced at optimum concentrations of the Ne and H_2 in a gas mixture. Chapter V describes the enhancement of HHG by using the technique of molecular alignment in a pump-probe experiment. Chapter VI investigates the enhancement of even and odd HHs with a two-color field. Chapter VII has initial work towards the application of HHG to imaging of micron to nano sized objects. Finally, Chapter VIII gives the summary of the research work carried out in the dissertation.

CHAPTER II

REVIEW OF HIGH HARMONIC GENERATION TECHNIQUE AND INSTRUMENTATION

This chapter focuses on the review of HHG technique, its experimental setup, employed laser system, and pulse measurement techniques.

2.1 Introduction to High Harmonic Generation

When an intense laser beam is focused into a gas, high harmonic generation (HHG) occurs. HHG is an attractive source of coherent radiation in the extreme ultraviolet (XUV) region, and it has various applications in physics, chemistry, and biology [47]. The typical intensity required for the HHG in the gases is on the order of 10^{13}-10^{15}W/cm^2. HHG phenomena can be understood in a semi-classical picture. An electron is tunnel ionized by the intense electromagnetic field of a laser pulse, and the freed electron is accelerated in the oscillating laser field and gains kinetic energy. If the electron recombines with its parent ion, it subsequently releases its kinetic energy, emitting harmonics of the fundamental field. Bright harmonic radiation is emitted, if the emission from many atoms in the medium adds constructively, i.e. phase-matched [48]. One of the great advantages of HHG source is that the emission is perfectly synchronized to the driving laser field. One can obtain a train of sub-femtosecond pulses of coherent light separated by half of the driving laser cycle when a number of high harmonic fields are phase-locked [49]. Ferenc Krausz and his collaborators created a single XUV pulse of duration 250

attoseconds (1as=10^{-18}s) comparable to the Bohr orbital period of a bound electron (~150as) in 2004 [50, 51]. Their research is leading the field of attophysics, the physics of generation, control, and application of sub-femtosecond laser pulses [52]. In addition, the life time of Auger decay in Krypton atom was measured (~7.9fs) by using an XUV pulse of ~900 as duration [53].

2.2 Details of High Harmonic Generation

2.2.1 Nonlinear Optics

After the invention of the laser in 1960, the nonlinear optic has developed and finds applications in most significant technologies of the 20th century. There is a linear relationship between the applied low-amplitude electric field $(\vec{E})$ of light and the dielectric polarization $\vec{P}$ of a material, and it is given

$$\vec{P}=\varepsilon_0\chi\vec{E}\,, \tag{2.1}$$

where χ is the linear susceptibility, and ε_0 is the permittivity.

However, at high laser intensity at which laser field becomes comparable to the Coulomb field of the electron the nonlinear terms in the induced polarization become important. The polarization term in Eq. (2.1) can be expressed by the Taylor series.

$$\vec{P}=\varepsilon_0(\chi^{(1)}\vec{E}+\chi^{(2)}\vec{E}^2+\chi^{(3)}\vec{E}^3+...)\,. \tag{2.2}$$

The first term in Eq. (2.2) defines the linear susceptibility, and the second term defines the lowest order nonlinear susceptibility, and so on. The optical nonlinearities can be small compared with the first term, however the high order terms (the nonlinear polarization)

induced by the strong laser field can act as a source for the generation of frequency up-conversion of the fundamental field, so that the amplitudes of higher harmonics accumulate with the propagation distance.

HHG is a highly nonlinear optical process which occurs in the strong field regime. The required intensity of the fundamental field for the HHG process can be obtained by focusing a high power femtosecond laser beam. The contributions of higher order nonlinearities becomes significant at high laser intensities. However, there is an upper limit of the laser intensity for HHG. This is due to optical breakdown, when the electron density reaches a critical density and the medium becomes opaque to the laser radiation. Moreover, the increased magnetic component of the laser field is comparable to the electric field at high intensities ~10^{16}W/cm^2, and it prevents recombination with the parent ion, which limits the HHG process.

2.2.2 Three Step Model

At the high intensities, the bound electrons tunnel into the continuum over the Coulomb barrier. High harmonic generation stems from electron-ion interactions, and there is a probability for an electron to return to the parent atom with a high kinetic energy for each laser half-cycle, which results in HHs spectrum. With increasing HHs order the intensity of HHs initially decreases, but then a plateau is observed where the intensity of the HHs remains approximately the same. The plateau ends up with a sharp decrease of HH output called cutoff region, Figure 2.1.

The cutoff energy linearly depends on the ionization potential of the used atom [54], and the ponderomotive energy (U_p) that refers to free electrons averaged kinetic

energy gained in the laser electric field [55]. The cutoff energy ($E_{cutoff} = h\nu_{max}$) is given as [56]

$$E_{cutoff} = I_p + 3.17U_p \tag{2.3}$$

where $U_p = I/4\omega_0^2$ a.u is the ponderomotive energy, I is the laser intensity, ω_0 is the frequency, and the I_p is the atomic ionization potential of considered atom. This shows that harmonics are mostly generated with the highest frequency and the shortest wavelengths. In the HHG process, when the gas atoms or molecules are driven by the intense laser field of frequency ω_0, they emit radiation of higher frequencies $q\omega_0$ where q is odd integer (Figure 2.2).

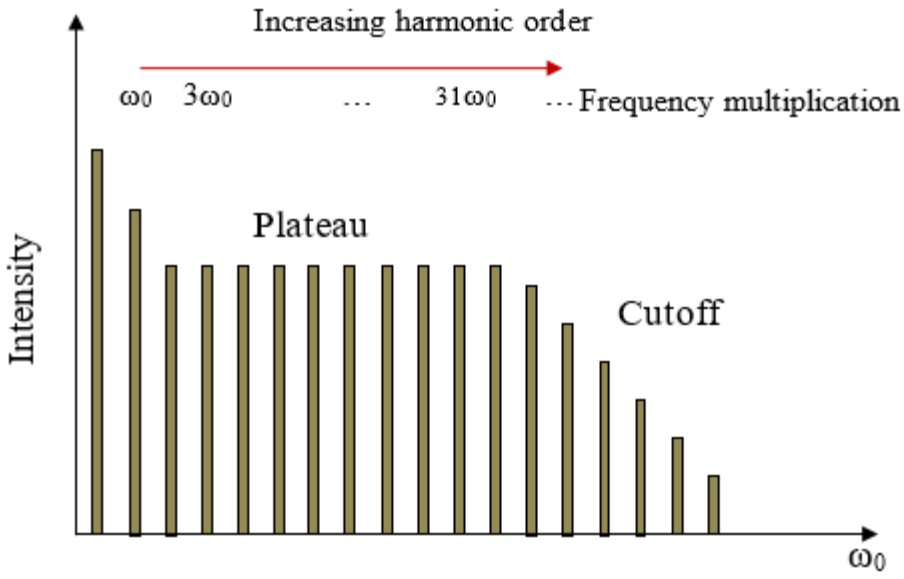

Figure 2.1 Schematic of high harmonic spectrum, where the spacing between the HHs are equal, and the frequency is an odd multiple of the driving laser frequency ω_0

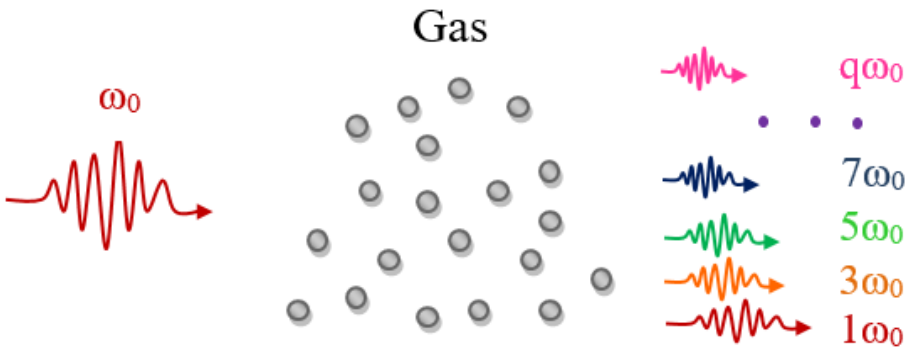

Figure 2.2 High harmonic generation (HHG)

HHG is most accurately described by the numerical integration of the Schrödinger equation, but a three-step model explains general features of HHG and provides a general picture of the process as seen in Figure 2.3 [55]. In the first step, the electron initially confined by the Coulomb potential of the atom, ionizes by absorbing many photons, or by tunneling through the suppressed Coulomb barrier in a strong laser field. In the second step, the laser field accelerates the electron away from the parent ion and drives back when the electric field sign is changed. For intense laser field after the electron is ionized the Coulomb potential of the atom can be ignored, so the electron can be considered as a free particle in this step. In the third step, the electron recombines with the parent ion, releasing its kinetic energy and the energy equals to the ionization potential, so the maximum harmonic (cutoff) energy is given $E_{max}=I_p+3.17U_p$ where I_p is the ionization potential of the atom, and as $3.17U_p$ is the maximum kinetic energy of the electron due to the oscillating laser field [55]. This coherent three step process occurs every half cycle of the laser pulse, leading to emission of odd harmonics, when the medium is statistically symmetric in the

polarization plane of the laser field. The three step model has been extensively used to describe HHG process.

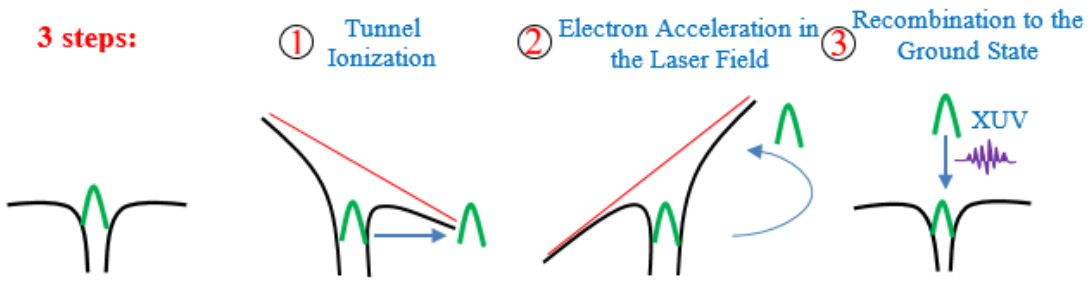

Figure 2.3 Schematic illustration of the three step model of HHG

2.2.3 Strong Field Approximation (SFA) Model (Lewenstein's Model)

The three-step model gives the basic explanation of the HHG process. However, it is not enough to explain the spectral characteristics for which, a quantum mechanical theory has been developed within the strong field approximation by Lewenstein et al. [57]. This model gives quantum-mechanical justification of the three-step model [57]. In this model, Lewenstein et al. solved numerically the time dependent Schrödinger equation (TDSE) in a strong field with three assumptions:

- The contribution of all the excited states except ground state can be neglected.
- The depletion of the ground state can be neglected.
- In the continuum states, the electron can be treated as a free particle moving in the electric field with no effect of the atomic potential, so the effect of the atomic potential on the electron can be neglected.

Under this approximations, Lewenstein et al. described quantum mechanically how an electron is promoted into a continuum state by the intense laser field, then propagates in the laser field, and finally recombines with the parent ion by a dipole transition. Also, the Lewenstein model predicts a cutoff energy, $E_{cutoff} = h\nu_{max} = FI_p + 3.17U_p$, slightly higher than that in the three-step model, and the factor $F(I_p/U_p)$ is equal to 1.3 for $I_p << U_p$, and it approaches unity as I_p grows [57].

2.2.4 Macroscopic Response (Phase Relations in HHG)

2.2.4.1 Introduction to Phase Matching

The description of the HHG process with the SFA theory provides the estimated shape of the harmonic spectrum. However, propagation effects needs to be considered for obtaining harmonic emission in the medium. For coherent buildup of the harmonic emission, the wave fronts of the fundamental laser and the generated harmonics must be properly maintained in phase, and achieving and maintaining a constant phase shift between the fundamental and the harmonics fields as they propagate is called the phase matching. When phase matching conditions are fulfilled, there is constructive interference of partial contributions to HHs, and these harmonics combine constructively to build up the harmonic emission, as depicted in Figure 2.4.

The distance over which the fundamental wave front and the harmonic wave front preserve coherence is called coherence length, $L_{coh} = \pi / \Delta k$ where Δk characterizes the phase mismatch. The phase matching condition in the HHG process is $\Delta k = k_q - qk_0 = 0$ where

q is the harmonic order, k_q is the wave vector of the q^{th} harmonic, and k_0 is the wave vector of the fundamental beam.

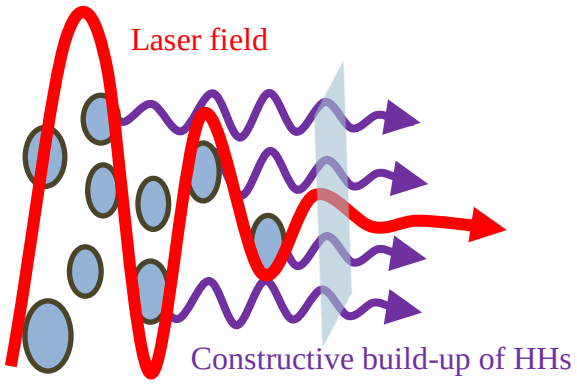

Figure 2.4 Macroscopic phase matching

2.2.4.2 Phase Mismatch

The harmonic flux is strongly affected by phase mismatch. Under high laser intensity the gas medium is partially ionized and becomes a mixture of ions and ionized electrons, i. e. acquires plasma component. In general total phase mismatch is the sum of four terms and can be expressed as [58].

$$\Delta k=\Delta k_{at}+\Delta k_{elec}+\Delta k_{Gouy}+\Delta k_{dip} \tag{2.4}$$

where Δk_{at} is neutral (atomic) gas dispersion phase mismatch, Δk_{elec} is plasma (electronic) dispersion phase mismatch, Δk_{Gouy} is geometrical phase mismatch, and Δk_{dip} is atomic dipole phase mismatch. The phase matching of HHG can be achieved by balancing the de-phasing terms presented in Eq. (2.4) to reach a zero phase mismatch.

The neutral gas dispersion phase mismatch is due to the material dispersion and is given by $\Delta k_{at} = \frac{2\pi qP}{\lambda_0}(1-n_f)(n_{IR}-n_q)$ where P is the gas pressure, and λ_0 is the fundamental wavelength, and q is the harmonic order, and $n_f = N_e/N_a$ is the ionization fraction that is ratio of electron density to the density of neutral atoms, and $(n_{IR}-n_q)$ is the difference between the refractive indexes of the gas per bar at the fundamental and harmonic fields.

Plasma dispersion phase mismatch is due to production of free electrons during the ionization process, and it is given by $\Delta k_{elec} = PqN_e r_e \lambda_0$ where r_e is the classical electron radius, and N_e is the free electron density per bar [58]. The free electrons cause plasma dispersion which can reduce the harmonic yield.

The geometrical phase mismatch arises from the Gouy phase shift when the Gaussian laser beam is focused, and it is given by $\Delta k_{Gouy} \sim (q-1)\frac{\tan^{-1}(z/z_R)}{z}$ where z_R is the Rayleigh range ($z_R = (\pi\omega_0^2/\lambda_0)$), and z is the displacement from the focal point along the laser beam.

The atomic dipole phase mismatch is an intensity dependent phase mismatch in HHG process, and it depends on the quantum path of the electron before it comes to the parent atom core, and this quantum path is different for long or short trajectories. It is given by $\Delta k_{dip} \sim -\alpha \nabla I$ where ∇I is the variation of the intensity along the beam in the gas cell, and α is the nonlinear coefficient depending on the quantum path corresponding to the short and long trajectories of the electrons. For example, for proper laser intensity and return time of the electrons, electrons following the short trajectory $\alpha \sim 2\times10^{-14} cm^2/W$ and

for those travelling along the long trajectory $\alpha \sim 22\times10^{-14}cm^2/W$ [59-61]. Above reasons prevent the efficient phase matching conditions in the laser focal region and restrict the efficiency for the generated XUV light.

2.2.4.3 Absorption of Harmonic Radiation

In addition to the phase matching phenomena, the efficiency of the harmonic radiation is still limited by absorption of the harmonic emission in the gas medium. For the phase matched harmonic emission, the harmonic signal grows with increasing interaction length and with increasing pressure. However, the harmonic signal is attenuated due to the absorptive medium. Thus, it is not worth trying to improve the output photon yield by increasing the interaction length and the gas pressure since the harmonic signal has reached the absorption limit after the harmonic signal is optimized in terms of pressure and interaction length.

2.3 General Experimental Equipment

2.3.1 Laser Systems

Our laser system consists of four lasers feeding each other. They are named by the manufacturer as Millenia V, Kapteyn-Murnane (KM oscillator), Evolution and Spitfire (regenerative amplifier) [2].

2.3.1.1 Millenia V

The Millennia V is a solid-state, high power, visible continuous wave (CW) laser that supplies larger than 5W of 1064nm output pulse from the output of a diode pumped intracavity Nd:YAG laser. The emission is then frequency doubled by a temperature tuned

lithium triborate (LBO) crystal resulting in radiation at 532nm. In our system, Millennia V is used to pump the femtosecond oscillator Kapteyn-Murnane (KM) with a continuous optical power of 5.5W at a 532nm wavelength [2].

2.3.1.2 Kapteyn-Murnane (KM) Oscillator

Kapteyn-Murnane (KM) is a mode-locked Ti:Sapphire femtosecond oscillator pumped by Millennia V. To achieve the Kerr lens effect, concave mirrors, which form the telescope with the crystal in the focal plane are placed. The Ti:Sapphire femtosecond oscillator is shown in Figure 2.5 where M1, M2, M3, M4, M5 are the cavity mirrors, and where M3 is also the output mirror. The group velocity dispersion experienced by the laser pulse traveling inside the crystal is compensated by a pair of prisms P1 and P2 that are also used to compensate the dispersion in the crystal. The output of the oscillator is a train of pulses at a particular chosen wavelength in the region from 780nm to 830nm, the pulse duration is about 35fs, the repetition rate is close to 80MHz, the pulse energy 5nJ/pulse and the average power is about 400mW [2].

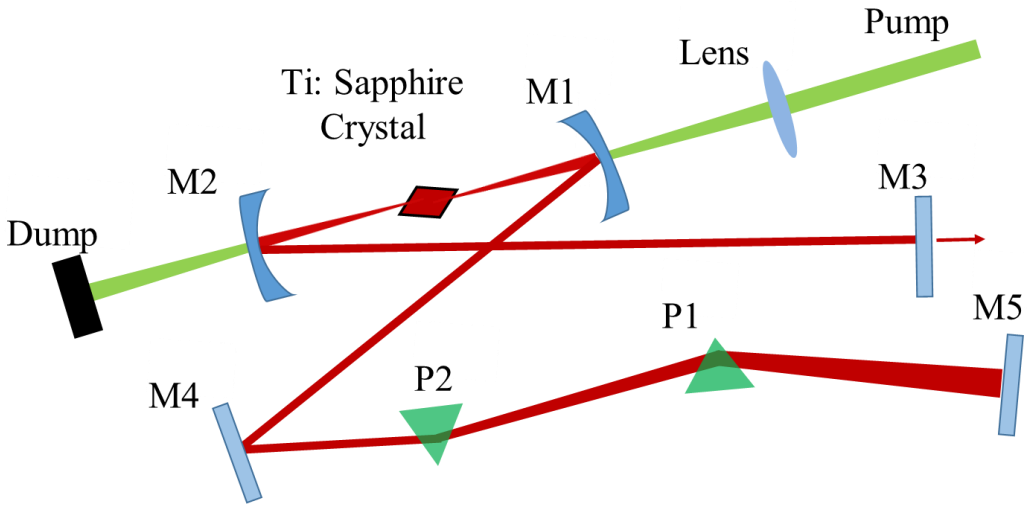

Figure 2.5 The outline of the Ti:sapphire femtosecond oscillator (KM oscillator). M1, M2, M3, M4, M5 are the cavity mirrors, where M3 is at the same time the output coupler. The group velocity dispersion experienced by the laser pulse traveling inside the crystal is compensated by a pair of prisms P1 and P2

2.3.1.3 Evolution 15

The Evolution is a Q-switched Nd:YAG laser (Spectra Physics, Merlin) at a repetition rate 1kHz, output power 10W emitting at a 532nm wavelength with ~10ns pulse duration. The gain medium and pump lasers are enclosed inside the laser head and co-located in a directly water cooled resonant cavity. The evolution is used to pump the spitfire [2].

2.3.1.4 Spitfire (Regenerative Amplifier)

The regenerative amplifier technique is used to amplify femtosecond pulses. In our system (Figure 2.6) [2] it is used to amplify a seed pulse (KM Oscillator) that generates thousands of pulses with repetition rate around 80MHz. However, the amplifier is pumped by evolution that has repetition rate of several kHz. Thus, only small part of the pulses from the oscillator is allowed to be amplified. The seed pulse will be inside the cavity when the

pump pulse passes through the crystal. When the gain is saturated, the amplified pulses are let out of the cavity. For this reason a fast optical switch that has a response time in the nanosecond range is required. The Spitfire consist of three main parts: stretcher, regenerative cavity and compressor. The seed pulses are expanded in a gain stretcher during the time. A photodiode that is placed behind one of the cavity mirrors helps one to monitor trace of the femtosecond pulses on the oscilloscope. The Pockels cell changes the refractive index of the material under the applied electric field. So the linearly polarized pulse is generated. The amplifier is pumped by evolution at a 1kHz repetition rate. The output of the amplifier is a train of the pulses having repetition rate ~1kHz, pulse duration of ~50fs and pulse energy of ~1mJ [2].

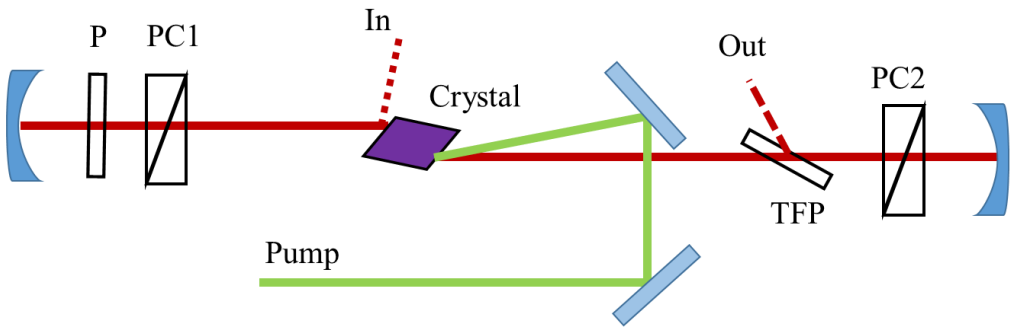

Figure 2.6 Schematic of regenerative cavity. In: incident beam, P: photodiode, PC: Pockels cell

2.3.2 Frequency Resolved Optical Gating (FROG) – GRENOUILLE

Frequency resolved optical gating (FROG) helps researchers characterize the pulses in the temporal domain. FROG has the ability to measure femtosecond pulse's intensity vs. time [2, 62]. The FROG setup shown in Figure 2.7 consists of an auto-correlation unit and a spectrometer Autocorrelation separate a laser pulse in two and delayed one pulse with

respect the other, and then focusing and recombining them on the nonlinear medium (Second Harmonic Generation Crystal (SHG)). The SHG crystal produces twice the frequency of the input laser, and the spectrometer determines the shape and the phase of the laser pulse. The FROG is updated by Trebino et al. They replaced the beam splitter, delay line and beam combining optics with Fresnel biprism [2, 62].

In this device the beam splitter, delay line and beam combining optics are replaced with a Fresnel biprism and with a thick SHG crystal. Thus, GRENOUILLE is a combination of two cylindrical lenses, Fresnel biprism, and the SHG crystal. The first lens focuses the beam into the SHG crystal, the Fresnel biprism splits the beam, and delays one pulse relative to the other, and the second lens focuses the beam onto a CCD camera. In Figure 2.8, we show the results of the measurements with the Grenouille (8-20, Swamp Optics) [2].

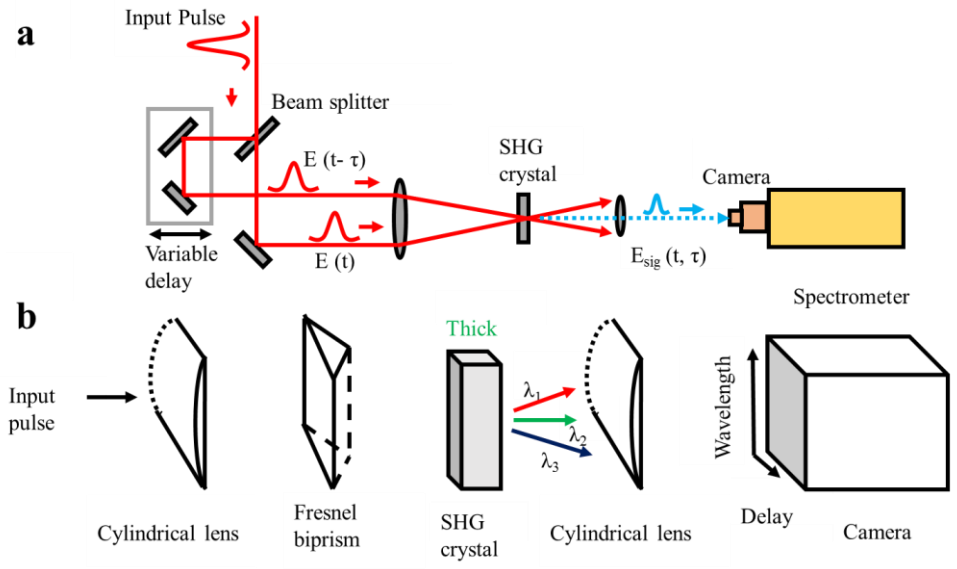

Figure 2.7 (a) Optical scheme of SHG FROG. (b) GRENOUILLE is the simplest version of the FROG

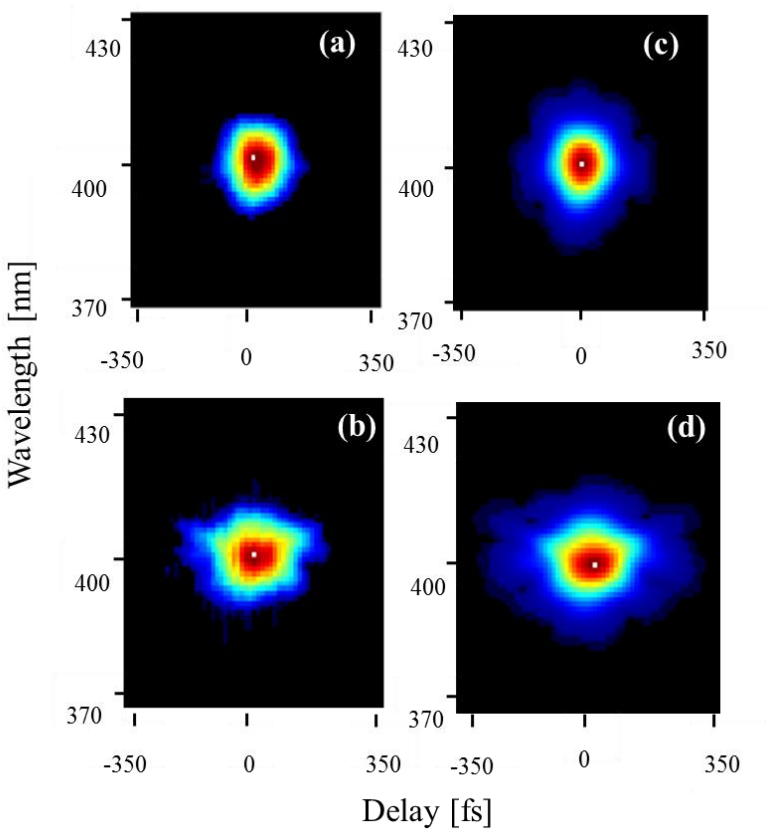

Figure 2.8 Images of femtosecond pulse taken from GRENOUILLE. (a) Compressed pulse at 52fs. (b) Stretched at 81fs. (c, d) Retrieved images are from compressed pulse and the stretched pulse, respectively [2]

2.4 Basic Experimental HHG Setup

The HHG setup consist of two separate chamber, namely interaction chamber and detection chamber. In the interaction chamber, there is a needle made of 1mm thickness nickel tube that supplies gas to the gas jet (Figure 2.9). The focused laser beam makes holes in to nickel tube, so the gas is ejected from both sides, and the radiation can pass through the holes. Then, the nonlinear interaction between high density gas atoms and intense laser field produces high harmonic generation. The operating ambient pressure in

the interaction chamber is on the order of 2.5×10^{-3}mbar that corresponds to the pressure in the gas jet of ~50mbar.

The generated harmonics propagate to detection chamber with a McPherson XUV spectrometer. The operating pressure in this chamber is below $<5\times10^{-6}$mbar. The low pressure is required, first, to reduce the absorption of the generated HHs and, second, to operate the micro channel plate (MCP) in the detection chamber, since the MCP can be damaged at higher pressure.

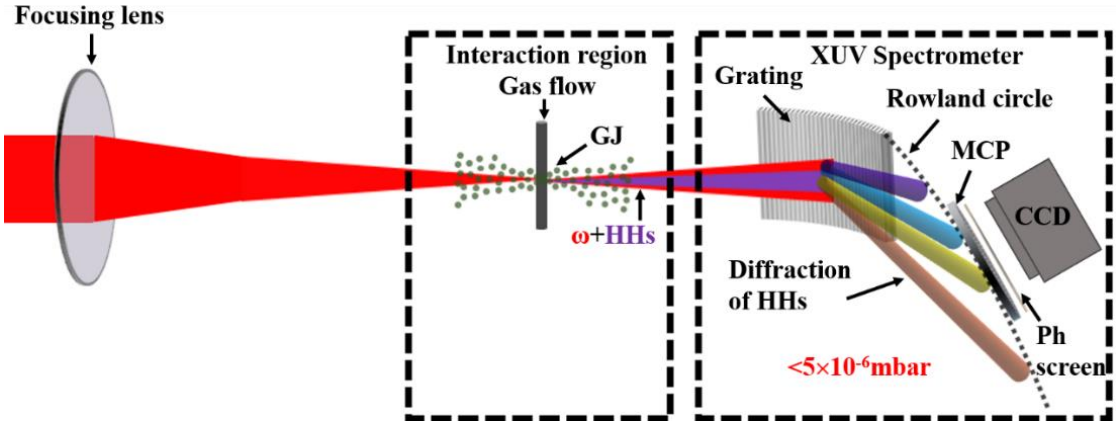

Figure 2.9 Experimental setup of HHG. GJ: gas jet, HHs: high harmonics, MCP: micro channel plate, Ph: phosphor screen, CCD: charge coupled device

2.4.1 Gas Jet (Estimation of Pressure in the Gas Jet)

The gas jet is efficient for the HHG process due to its short interaction length (<1mm). The gas jet used in the experiment has a simple design, which consists of a short piece of nickel (Ni) tube (From GoodFellow Company) with an inner diameter of 1.1mm, and outer diameter of 1.3mm, and a length of ~4cm, which carriers the gas, and the Ni tube is sealed at the end to allow the expansion of the gas through the holes produced by the laser, Figure 2.10. The interaction chamber has a background pressure $<10^{-6}$mbar when the gas flow is

turned off and a pressure of ~10^{-3}mbar when the gas is flowing. The large turbo molecular pump reduces the background pressure in the chamber, and allows a supersonic expansion.

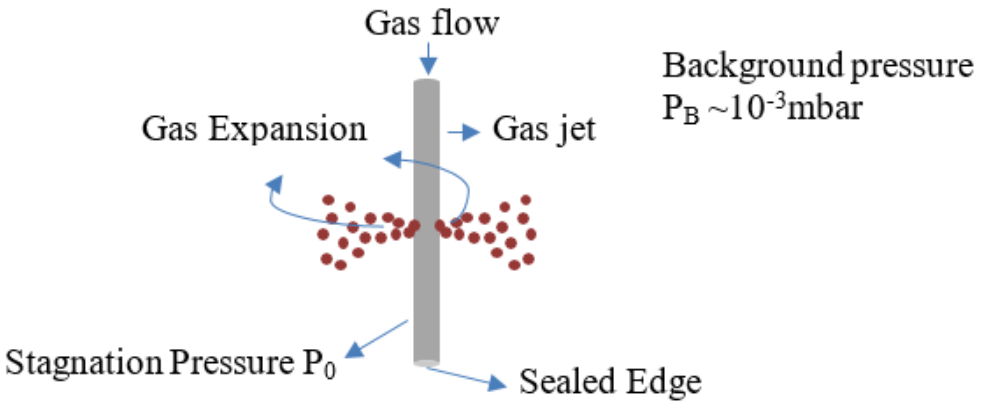

Figure 2.10 Diagram of a free gas jet

The stagnation pressure of the gas jet P_0 is estimated from consumption of a gas from a small size lecture bottle. The gas jet is at a high pressure compared to a low ambient background pressure, and it is at negligibly small velocity, which is called a stagnation state (P_0), and the flow is created by the pressure difference (P_B-P_0), where P_B is the background chamber pressure. The gas ejection is accepted ideally sonic, and we can estimate the pressure at the gas jet by using the mass flow equation [63] as

$$\dot{m} = P_0 A \left[\left(\frac{\gamma M}{RT} \right) \left(\frac{2}{(\gamma+1)} \right)^{(\gamma+1)/(\gamma-1)} \right]^{1/2}, \qquad (2.5)$$

where A is the area of the opening, M is the molar mass of the used gas, R is gas constant, T is the temperature, and the $\gamma=1.667$ that comes from the ratio of the specific heat capacity at constant pressure to constant volume c_p/c_v. $\dot{m}$ is experimentally determined

by observing the consumption of gas from a small size lecture bottle providing backing pressure. Figure 2.11 shows the plot for the backing pressure dependence as a function of time, and we can determine the fit function from experimental dependence. The linear dependence of the pressure is determined as, P=at+b where a=-0.00178 and b=1.855 are constants determined from the blue line in Figure 2.11. By using the ideal gas equation, $PV = \frac{m}{M} RT$, we determine the $\dot{m}$ in terms of $\dot{P}$, $\left(\dot{m} = \dot{P} VM/RT \right)$, where $\dot{P} = a$, which is determined from the fit function, Figure 2.11. Then, putting $\dot{m}$ into above Eq.(2.5), we estimate the stagnation pressure at the gas jet as P_0~50mbar.

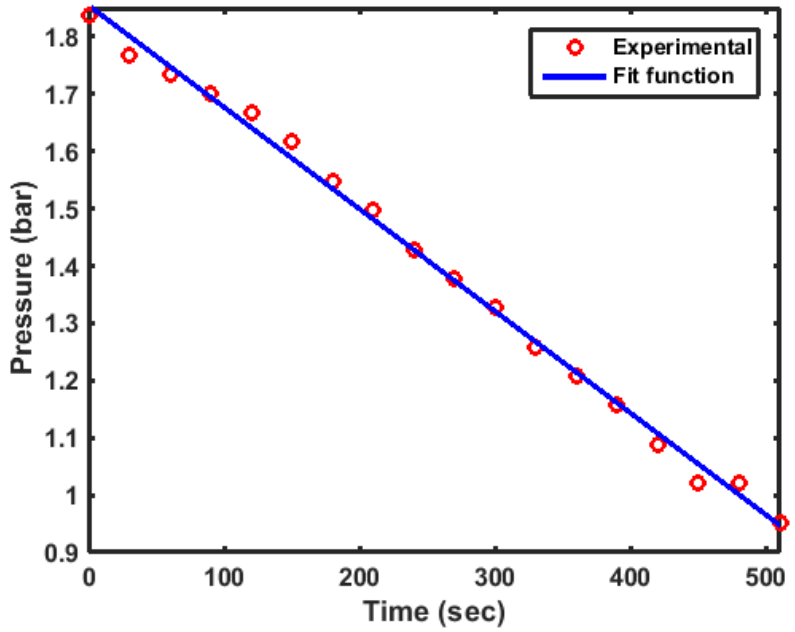

Figure 2.11 Consumption of mass. Red is experimental data, blue is fit function

2.4.2 Determination of the Beam Size and Intensity

In laser physics, laser beams can be often described in the form of a Gaussian beam. The radial intensity distribution of the Gaussian beam can be written as

$$I(r)=I_0 e^{-2r^2/r_0^2}. \tag{2.6}$$

To determine the radius of the beam r_0 one can use an aperture and measure the power of the beam limited by this aperture. Beam power passing through a circle with a radius r is:

$$P(r)=P_0[1-e^{-2r^2/r_0^2}], \tag{2.7}$$

where $P_0=\frac{1}{2}\pi I_0 r_0^2$ is the total power of the beam, r_0 is the beam radius. The intensity of the beam drops to $1/e^2$ at $r=r_0$. If the Eq.(2.7) is solved in respect to r_0, one gets [2]

$$r_0=\sqrt{\frac{2r^2}{-\log(1-\frac{P}{P_0})}} \tag{2.8}$$

In calculating the beam radius, we use an iris to block part of the beam, Figure 2.12. We change the radius of the iris in small steps from 0 to 3.5mm. Then, we measure the power for set of values of r. When the iris radius is 0mm, the beam is completely blocked, but if it is >3.5mm, the whole beam almost goes through the iris. Total average power of the beam is around 400mW when the iris is completely open. Calculating the

beam radius according to Eq.(2.8) for each (r, P) pair, where eight pairs were taken, the beam radius is determined as r_0=3.33±0.18mm [2].

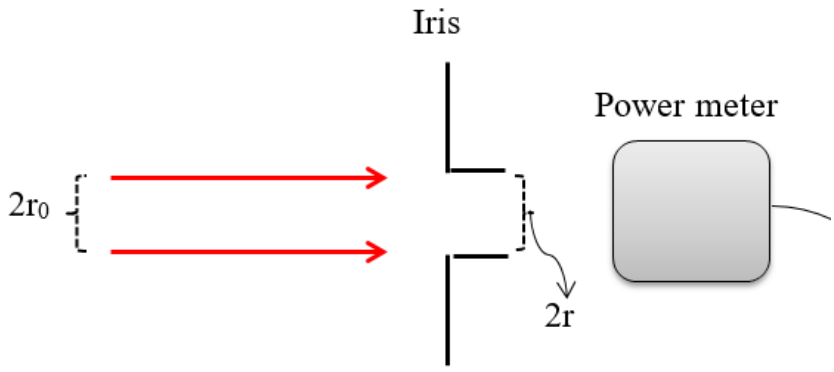

Figure 2.12 Schematic of the beam size evaluating with an iris

2.4.3 McPherson XUV Spectrometer

An important tool in our setup is the XUV McPherson monochromator (model 248/310G) that is designed to cover wavelength region from 1nm to 300nm. This monochromator has the grating nominal radius of R_G=998.8 mm or 39.323 inches. The counter reading of the McPherson monochromator is related to actual wavelength by a relationship **[**2**]** (see Appendix B for the code calculating HH spectrum)

$$\lambda = d\left(\sin[\alpha_i] - \sin\left[\frac{\pi}{2} - \sin^{-1}\left[\frac{L}{2R_R}\right]\right]\right) \qquad (2.9)$$

where λ is the wavelength, d is the grating period (1/133.6 mm), $\alpha_i = 87.6^{\circ}$ is the angle of incidence of the XUV radiation, L is the counter reading in inch, $R_R = R_G/2$ is the radius of the Rowland circle, and R_G is the grating radius. The McPherson spectrometer employs a MCP detector positioned on the Rowland circle, (see the next section 2.4.3.1 for the

description of this arrangement with the Rowland circle). The wavelength-counter reading dependence of Eq. (2.9) is plotted in Figure 2.13.

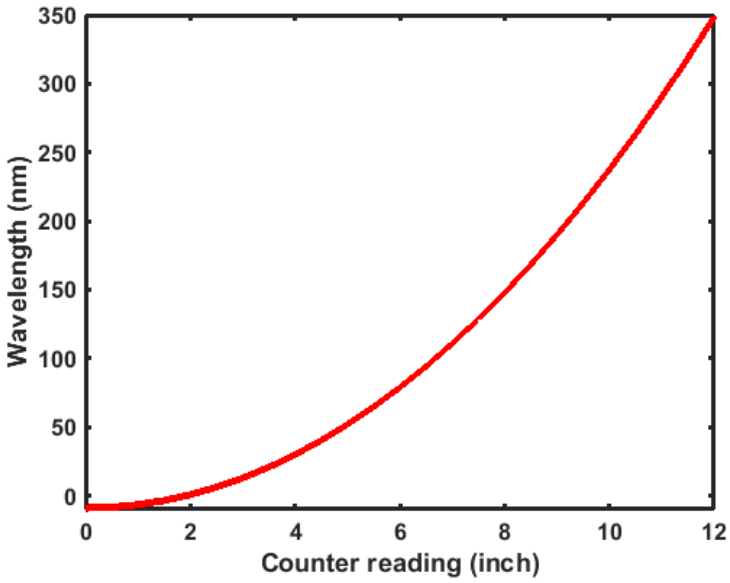

Figure 2.13 A typical wavelength calibration chart for the distance reading in term of inches along the Rowland circle

2.4.3.1 Rowland Circle

Henry Augustus Rowland (1848–1901) devised an instrument that allows the use of a single optical element that combines diffraction and focusing, i.e. concave grating (Figure 2.14). There are several advantages of using Rowland optical element in optical experiments, since it does both focuses and separates radiation of different wavelengths. This reduces the cost of the optical components in the instrument, reduces alignment time, and also minimizes reflective and refractive energy losses as well. The initial radiation is dispersed by the grating (133.6 groove/mm) into spectra, which are then focused on the input surface of the micro channel plate (MCP).

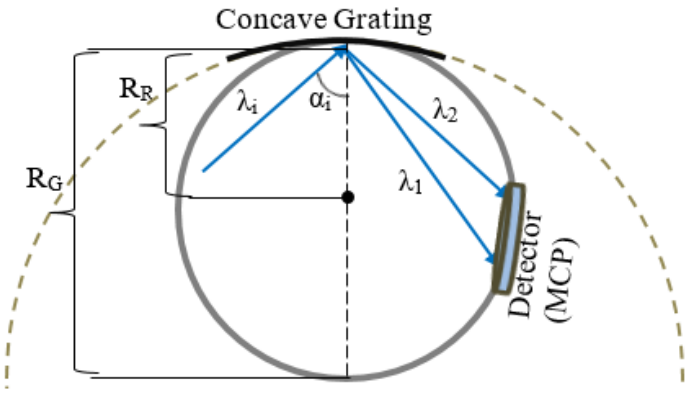

Figure 2.14 An illustration of the Rowland circle: The initial radiation is dispersed into a spectrum due to the concave grating, and the spectra are focused onto the MCP detector. λ_i depicts the initial radiation, λ_1 and λ_2 show the dispersed radiation. R_R and R_G are radii of the Rowland circle and the grating, respectively, and α_i is the incidence angle

The McPherson spectrometer (Model 248/310) that we use in the setup is built with the Rowland circle configuration. The radiation propagating through the entrance slit is dispersed by the grating and also focused in an arch of the Rowland circle. Each position of the MCP detector covers only some interval of the wavelength, while by moving it over the Rowland circle allows to cover the full spectral range of the spectrometer. The relation that the Rowland circle diameter is equal to the diffraction grating radius insures the best focusing and spectral resolution at the wavelength of interest [64]. The groove density of the grating determines its dispersion properties. Higher groove densities result in greater dispersion [65]. In our McPherson spectrometer, there are two different gratings: one has grooves of 133.6g/mm, and the other has 600g/mm. We used the grating having groove density 133.6 g/mm which allowed measurements in the wavelength region relevant to our experiments.

2.4.3.2 Image Intensifier

The image intensifier is made of three parts, a photocathode input coated with semiconductor, an electron multiplying MCP (two-stage chevron type), and a phosphor screen. Initially, the incident photons strike the photocathode where photons are converted into electrons due to the photoelectric effect. The released electrons are accelerated by the applied MCP voltage, and they are multiplied by a high gain (~10^6) factor of the MCP after travelling through the MCP channels. Finally the multiplied electrons fall on the phosphor screen due to voltage difference between the MCP (~2kV) and phosphor screen (~4kV), and partially convert their kinetic energy into photons emitted from the phosphor screen. Finally, an optical lens transfers the image from the phosphorous screen onto the CCD camera, Figure 2.15.

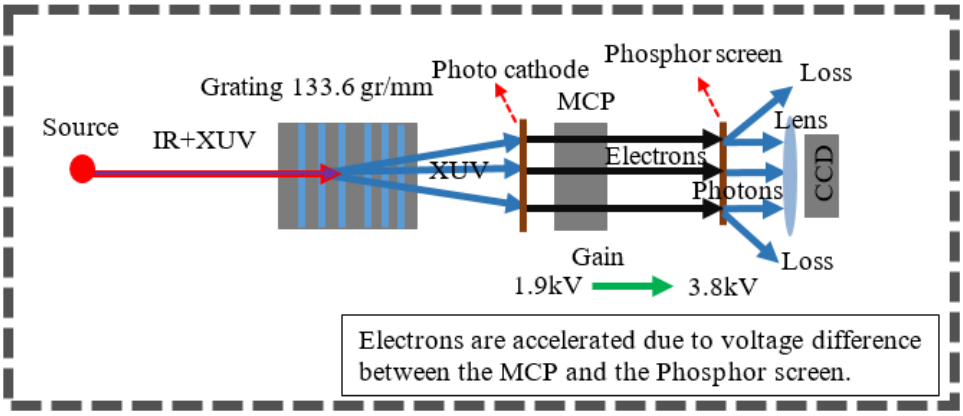

Figure 2.15 Demonstration of photon detection principle by MCP and formation of image on the CCD camera

2.4.3.2.1 Photocathode

The photocathode is the first major component of the image intensifier that converts a portion of photons of the incident light into electrons. Photons that are not captured by photocathode are lost in the final produced signal. The quantum efficiency (QE) is defined as the percentage of incident photons converted into electrons.

2.4.3.2.2 Micro Channel Plate (MCP)

The second important component of the image intensifier is a micro channel plate (MCP). The MCP consists of millions of ultra-small (~10 micron) diameter glass capillaries (channels), which are put together forming a thin disk with the diameter of 40mm. When the radiation enters one of this traversing channel, electrons are released from the channel wall. These electrons are accelerated by the electric field applied to both end faces of the MCP, and they strike the wall of the channel multiple times while traveling in it and release secondary electrons, Figure 2.16. This process is repeated many times along the channel, and finally the cascade of electrons is emitted from the output side. The number of the exiting electrons depends on the gain of the MCP that is different for different types of MCP. For example, a single MCP that stands up to voltage of 1kV gives gain in the order of ~10^4. To get higher gain, two or three MCP should be used in a stacked configuration. For example, the two stage MCP gives the gain ~10^6, and three stage MCP gives the gain in excess of more than ~10^7.

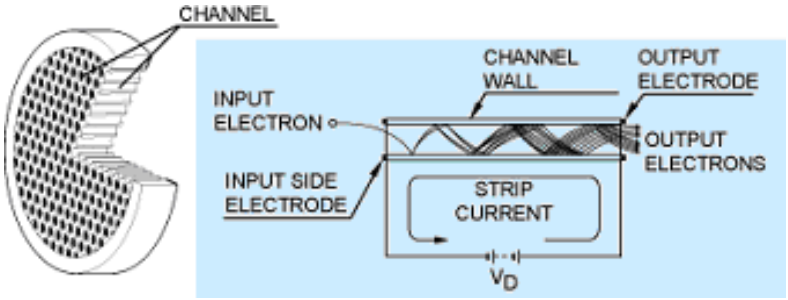

Figure 2.16 Schematic construction and operating principle of MCP. The image is adopted from [1]

2.4.3.2.3 Phosphorous Screen

The third major component of image intensifier is phosphorous screen. The screen is made of phosphor material coated onto a glass plate of a fiber optic plate (FOP), which is used to convert output signal (electrons) from the MCP into visible image (photons) instead of detecting as electrical signal. A high accelerating voltage (~4kV) is applied across the MCP and phosphor screen to get two dimensional high resolution image. Electrons leaving the MCP are zoomed by this voltage to the phosphorous screen, where they are converted back to photons. The optical images obtained on the phosphorous screen can be observed with an imaging system using a charged coupled device (CCD camera).

2.5 Estimation of HHG Conversion Efficiency

To be able to calculate conversion efficiency of the total generated high harmonic signal (total XUV flux), we need to know the efficiencies of the components of the image intensifier.

Since the McPherson XUV spectrometer consists of several parts, namely the grating, the micro channel plate (MCP) with CsI photocathode coating, the phosphorous

screen (P43), and the charged coupled device (CCD camera), and each spectrometer part has efficiency loss or gain (spectrometer factor), we can estimate the total photon flux by using the sum of the pixels of the harmonic image captured by the CCD camera with considering the spectrometer factor. Additionally, the divergence of the XUV radiation on the experimental system cause the loss of the efficiency of the total flux, and we need to take into account this factor, which is experimentally calculated by inserting a knife edge plate into path of the XUV radiation. We experimentally determine the divergence of the XUV beam, ~0.2 degree as shown below, Figure 2.17. Moreover, there is the entrance slit (2mmx2mm) before the spectrometer, and the beam size at the slit is about 5mm, and the slit is substantially smaller than the size of the beam. The slit loss factor is calculated that the percentage of XUV light passing through the slit is the ratio of the slit area to the beam area, and that is $2\times 2/\pi(5/2)^2$, and it is ~20%. The loss factor is the geometrical loss due to position of the CCD camera to the spectrometer, and it is about %20.

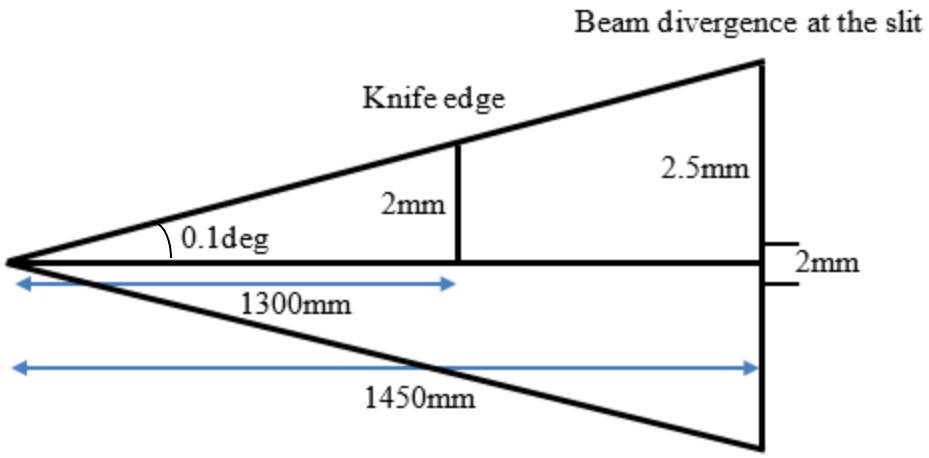

Figure 2.17 Estimation of the beam size at the slit

The required parameters for calculating the total XUV signal are given in Table 2.1 and 2.2. We can estimate total photon flux by using these parameters.

Table 2.1. Required parameters to estimate the efficiency of the HHG's flux

MCP Volt	MCP efficiency	MCP Gain	Phosphor Volt	Phosphor Efficiency	Repetition Rate	CCD Gain
1.9kV	0.01%	10^{15}	3.8kV	0.01%	1kHz	1

Table 2.2. Required parameters to estimate the efficiency of the HHG's flux

CCD Efficiency	Exposure time	Grating efficiency	Slit loss	Geometrical factor	Averaged total pixels
0.01%	2sec	0.3%	20%	20%	~10^{15}

So, the approximate total photon flux (Ph_{flux}) is

$$Ph_{flux} = \frac{Pixel_{total}}{Spect_{factor}} \tag{2.10}$$

where $Pixel_{total}$ is the total pixel measured on the CCD camera, and $Spect_{factor}$ is the loss factor of the spectrometer due to the parts of the spectrometer, and it is given as

$$Spect_{factor} = MCP_{eff} \times MCP_{gain} \times Phs_{eff} \times Cam_{gain} \times Cam_{eff} \times Geo_{fac} \times Slit_{loss} \times Grat_{eff} \times Exp \times Rep \tag{2.11}$$

where MCP_{eff} is the MCP efficiency, MCP_{gain} is the MCP gain, Phs_{eff} is the phosphor screen efficiency, Cam_{gain} is CCD camera gain, Cam_{eff} is CCD camera efficiency, Geo_{fac} is the geometrical factor due to position of the CCD to the spectrometer, $Slit_{loss}$ is the loss

due to slit, $Grat_{eff}$ is the grating efficiency, Exp is the exposure time of the CCD camera, and Rep is the repetition rate of the laser.

Then, the total photon flux for Ar gas is estimated about $1.64x10^{8}$ photons per laser shot, and total photon energy by considering the mean energy of the generated harmonics from 17^{th} to 29^{th} order (E_{mean}=36eV) is given

$$E_{XUV} = E_{mean} \times 1.6 \times 10^{-19} \times Ph_{flux} \times 10^{9} \quad (2.12)$$

Total photon energy for the Ar gas is about 0.94nJ. Finally, since we have ~0.6mJ pulse energy before the gas jet, we can estimate the conversion efficiency that is $0.94nJ/0.6mJ \sim 1.5x10^{-6}$.

By using the above formula, we make a similar estimate for the H_2 molecule. The total photon flux for H_2 is $1.93x10^{7}$ photons per laser shot, and the average of the generated harmonic energy from 17^{th} to 25^{th} harmonic is 32.55eV. By taking into account the total photon flux and average photon energy for H_2 gas, we found that the total XUV energy is 0.10nJ. Then, the conversion efficiency is about $1.6x10^{-7}$ (0.1nJ/0.6mJ) for H_2 molecule.

CHAPTER III

PRESSURE OPTIMIZATION OF HIGH HARMONIC GENERATION IN A DIFFERENTIALLY PUMPED AR OR H_2 GAS JET*

3.1 Introduction

High harmonic generation (HHG) in argon and molecular hydrogen on pressure changes in a gas jet is studied. Various experiments have been carried out using different laser intensities, pulse durations, wavelengths, and gas media, and their results have shown to be in qualitative agreement with the cutoff law [66-68]. On the other hand, experimentally obtained cutoff energies can deviate from calculated values due to such factors, i.e. the geometrical phase (Gouy phase) and the divergence of the laser beam that together with optical imperfections cause a lower laser intensity and a lower HH yield than expected in the medium [68-70].

The importance of focusing conditions for the output of HHs has been investigated previously by other groups [66, 71]. Since the XUV output inherently has a quadratic dependence on the atomic density [72] as it is expected for a coherent process, and an increase in the atomic density of the gas medium seems to be a straightforward way to increase the HH output [73]. However, enabling this seemingly simple approach depends

* Reprinted with permission from "Pressure optimization of high harmonic generation in a differentially pumped Ar or H_2 gas jet" by M. Sayrac, A. A. Kolomenskii, S. Anumula, Y. Boran, N. A. Hart, N. Kaya, J. Strohaber and H. A. Schuessler, 2015, Rev. Sci. Instrum. 86, 043108, Copyright 2015 by AIP Publishing LLC.

on several factors such as gas dispersion and absorption, which modify the phase matching conditions and limit the quadratic dependence [74] of the harmonic signal.

In this study we aim at increasing the HH output by optimizing the pressure of Ar or H_2 in a gas jet. Several experiments have been performed to improve conversion efficiency by optimizing gas pressure in the interaction region for different experimental configurations, and the results clearly depend on the generation geometry of the medium [75-78]. We confined our study to one particular geometry, where the gas jet is enclosed in a differentially pumped cell to enable measurements over a wide range of pressure values.

3.2 Experimental Setup

We used a Ti:Sapphire laser system that produces pulses of 1mJ in energy, 50fs in duration, and at a repetition rate of 1kHz, which were spectrally centered around a wavelength of 800nm. Harmonics were generated in a gas jet produced by burning holes with the laser beam in a squeezed nickel (Ni) tube (0.8mm outer and 0.6mm inner size), which carried the gas. The laser beam was focused by a 40cm focal length lens yielding an estimated peak intensity at the focus of 1.5×10^{14}W/cm^2. The gas jet (GJ) was enclosed, as is shown in Figure 3.1, in a cell having a volume of about 20cm^3 with the main portion of the ejected gas removed by a separate roughing pump (Oerlikon, Scroll 15), which enabled working at relatively high pressures in the interaction region (R2). The input hole (IH) and the output hole (OH) of the cell for passing the radiation are of 1.5mm diameter (see Figure 3.1 (b)). The cell has also a 1.5mm tube hole (TH) on the top for the Ni tube, sealed at the end. A bottom hole (BH) with a similar diameter is used for centering the Ni

tube. The laser beam was focused on the gas jet to produce high harmonics which were detected using an XUV spectrometer (McPherson, 248/310G). In this spectrometer, XUV radiation was diffracted by a grating (133.6groves/mm) to a micro-channel plate (MCP), which detected the different HHs. The image from the phosphorous screen mounted at the back side of the MCP was projected onto a charge-coupled device (CCD) camera; this latter image of spectrally resolved HHs was acquired with a LabVIEW program for subsequent processing.

Pumping of the main chamber, containing the gas jet cell, and a two-stage differential pumping on the path of the XUV radiation to the spectrometer are needed to reduce the absorption due to the gas and to maintain low pressure ($\leq 5\times10^{-6}$mbar) at the microchannel plate (MCP) of the XUV spectrometer. The pressure requirements of the MCP and pressure loads on the turbo molecular pump (Pfeiffer, TMU-521-YP) determines the upper limit of the achievable pressure in the gas jet. Maximum pressure limit ($\sim 7\times10^{-3}$mbar) in the main chamber is directly related to the load on the turbo molecular pump that was determined mainly by the flow to the main chamber through the holes IH and OH. The large front and back openings in the gas jet cell, directly connected through the tubing to the roughing pump, as is shown in Figure 3.1 (b), assuring that only a small portion of the total gas flow leaks to the main chamber.

The maximum pressure reached in the interaction region (R2) is estimated to be ~1.5bar for Ar, and ~0.5bar for H_2. The main reason for the dependence of the upper pressure limit on the gas type is due to the fact that the compression ratio (K) for the turbo molecular pump, which is defined as the ratio of the outlet pressure to the inlet pressure,

and it is determined by the formula: $K \sim \exp(f v_B / v_m)$ [58], where V_B is the blade speed of the pump, $v_m = \sqrt{8RT/\pi M}$ is the mean molecular speed, R is the molar gas constant, T is the temperature, M is the molar mass of the gas, and the factor f depends on the numbers and configuration of blades of the pump. Thus, the K-value is exponentially increasing with the square root of the molar mass of the gas via the dependence on the mean molecular speed of the gas, and as a result, the compression ratio for Ar gas is a factor ~ 130 higher than for H_2, meaning that H_2 is harder to pump than Ar owing to a 20 times smaller molar mass of H_2 compared to Ar.

The gas leakage due to the openings in the gas cell (IH and OH) to the main chamber (R1) (see Figure 3.1) determines the maximal pressure ratio in the gas jet, when the valve to the additional roughing pump is open or closed. This ratio is experimentally determined by comparing the outputs of HHs in two different cases with open or closed valve by adjusting the flow through the gas jet and measuring the pressure in the main chamber. This pressure ratio, or more precisely the pressure gain, is found to be ~15 for Ar, and ~5 for H_2. The gas jet pressure (region R2) is estimated by measuring the consumption of gas from a small size lecture bottle (in this case, additional pumping from region R3 is disabled), taking into account the diameters of the IH and OH holes in the Ni tube (~100μm). This gas jet pressure is determined to be ~50mbar, which corresponded to the pressure in the main chamber (R1) $\sim 2.5 \times 10^{-3}$ mbar.

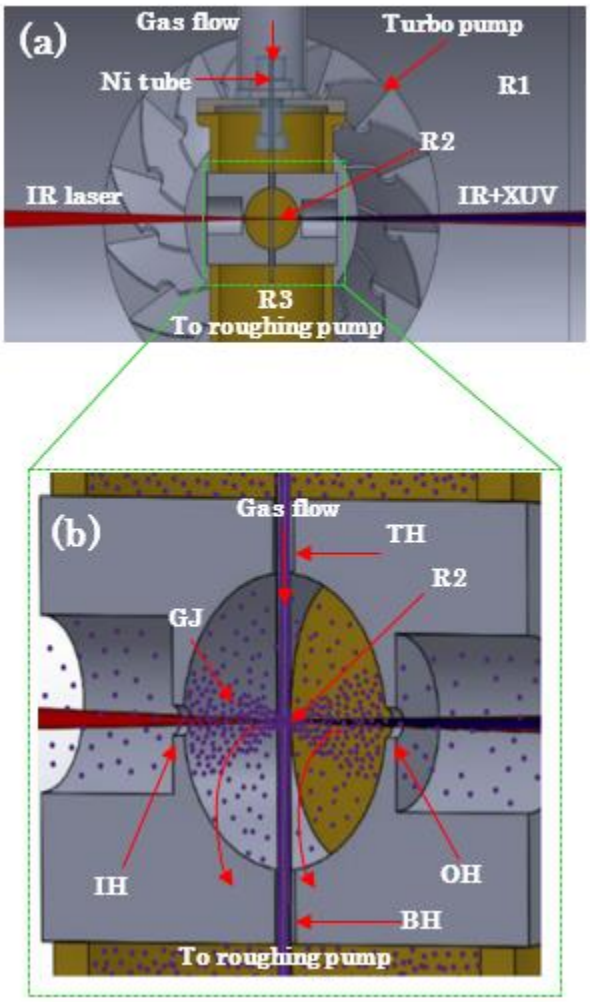

Figure 3.1 Schematic of the experimental arrangement of the gas jet assembly and differential pumping: (a). Front view of the inside of the main chamber containing the gas jet cell and the turbo molecular pump behind it. The differential pumping is created between the region of high pressure R2 and the pressure in the main chamber, region R1; region R3 is connected to an additional roughing pump, removing the main portion of the gas directly from the gas jet cell before it reaches region R1; IR: infrared radiation, XUV: extreme ultraviolet radiation. (b) Enlarged oblique view of the central part of the gas jet cell. IH: input hole, OH: output hole, TH: tube hole, BH: bottom hole, GJ: gas jet

3.3 Experimental Results

Harmonic generation was measured and compared for two cases, corresponding to different gas jet pressures (in R2): (1) the additional pumping with the roughing pump is disabled (the valve to the roughing pump is closed) and (2) the additional pumping is enabled (the valve to the roughing pump was opened).

The HHs spectra for Ar gas are shown in Figure 3.2. In the Ar gas jet without additional pumping we reach pressures of up to ~0.12bar, while with additional pumping we reach up to ~1.5bar. The pressure dependence of the HH output for Ar gas is shown in Figure 3.3; we observe odd harmonics from the 17th to 29th order. The maximum output is achieved at an optimum pressure of ~0.2bar (~5×10^{18}atoms/cm^3) for all harmonics Figure 3.3.

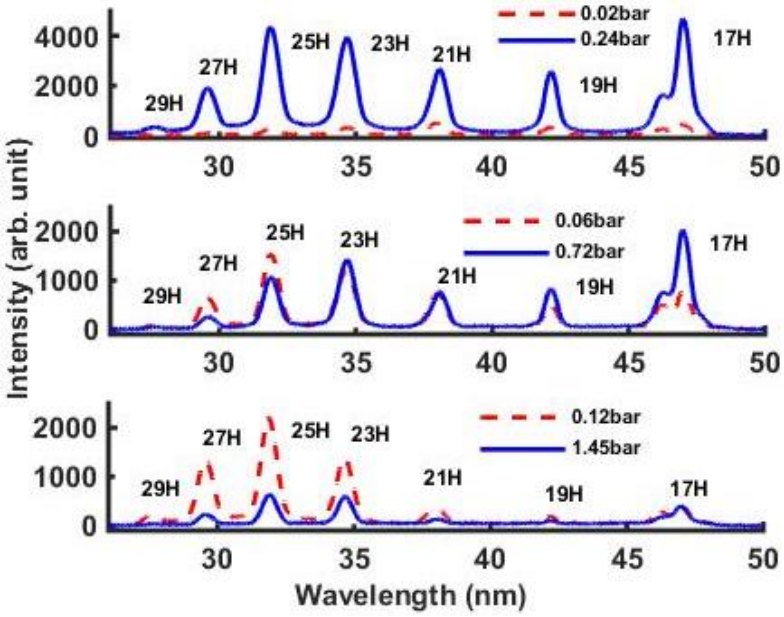

Figure 3.2 HHG spectra at different gas jet pressures of Ar gas. Red lines are for disabled additional pumping, and blue lines are for enabled additional pumping

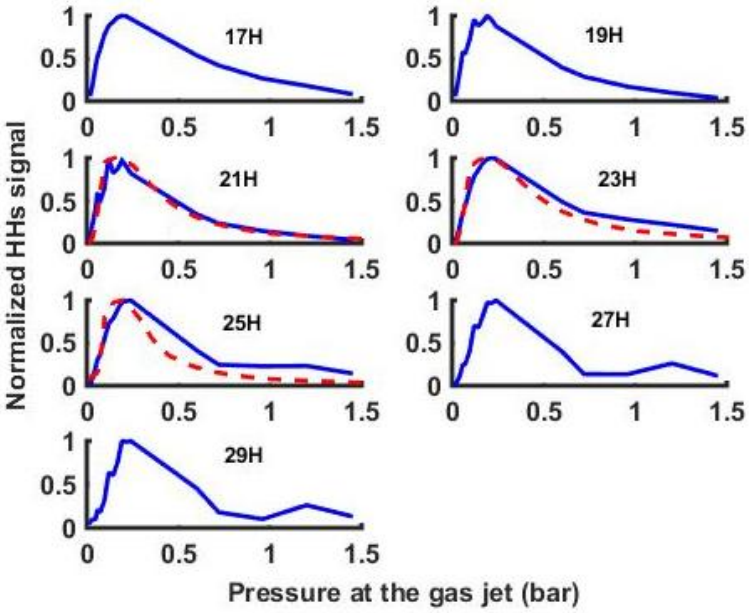

Figure 3.3 Ar pressure dependence of HHs output normalized to the maximum output, reached at optimum pressure ~0.2bar. Blue solid lines are experimental results, and red dashed lines are calculations with the 1D-model. Further explanations are given in the text

For H_2 gas jet without additional pumping we reach pressures up to~0.09bar, while with additional pumping pressures up to ~0.5bar could be reached. The HHs spectra for H_2 are presented in Figure 3.4. The pressure dependences of the HHs output for H_2 gas are shown in Figure 3.5. We observe odd HHs from the 17th to the 25th orders with their output exhibiting saturation at a pressure approaching ~0.5bar (~1.25×10^{19}atoms/cm^3) (Figure 3.5).

Since both gases have similar ionization potentials (I_p~15.6eV for Ar [79] and I_p~15.4eV for H_2 [80]), the above-mentioned formula for the cutoff energy gives, for both gases, about 42eV. The experimentally observed cutoffs are 29^{th} HH (~45eV) for Ar, and 25^{th} (~39eV) for H_2. The highest harmonics are also more difficult to observe for H_2, since HH signal is about 20 times lower than for Ar.

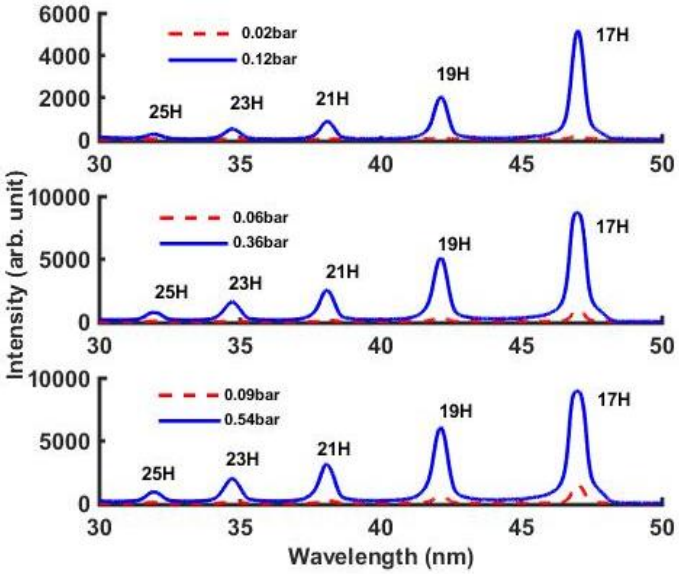

Figure 3.4 HHG spectra at different gas jet pressures of H_2. Red lines are for disabled additional pumping, and blue lines are for enabled additional pumping

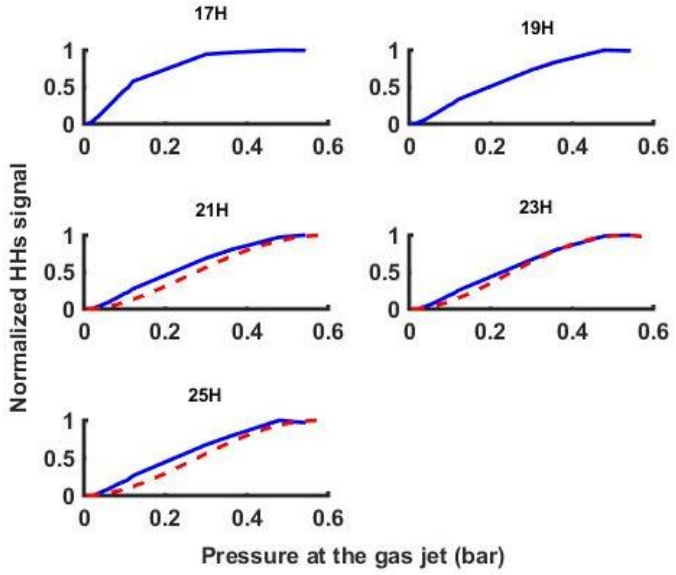

Figure 3.5 H_2 pressure dependence of HHs output normalized to the maximum output, reached at ~0.5bar. Blue solid lines are experimental results, and red dashed lines are calculations with the 1D model. Further explanations are given in the text

3.4 Theoretical 1D Model

To calculate the pressure dependence of the HHs, we used the one dimensional model of Ref [72].

$$S_{HHG} \sim \frac{4L_{abs}{}^2 P^2 A_q{}^2}{\left[1+4\pi^2\left(\frac{L_{abs}{}^2}{L_{coh}{}^2}\right)\right]} \times \left(1+e^{\frac{-L_{med}}{L_{abs}}} - 2\cos\left(\pi\frac{L_{med}}{L_{coh}(t)}\right)e^{\frac{-L_{med}}{2L_{abs}}}\right) \quad (3.1)$$

Here P is the gas pressure in the jet, A_q is the dipole amplitude of the q^{th}-order harmonic; L_{abs} and L_{med} are the absorption length and the medium length, respectively and L_{coh} is the coherence length $L_{coh}=\pi/\Delta k$, where the wave vector mismatch Δk between infrared and XUV light is given as

$$\Delta k=\Delta k_{at}+\Delta k_{elec}+\Delta k_{Gouy}+\Delta k_{dip} \quad (3.2)$$

The first term in Eq.(3.2) is the atomic dispersion given by $\Delta k_{at} \sim 2\pi qP(1-n_f)(n_{IR}-n_q)/\lambda$ [81, 82], where q is the harmonic order, (n_{IR}-n_q) is the difference between the refractive indexes of the gas per bar at the fundamental and harmonics wavelengths, and n_f (~0.2) is the ionization fraction of Ar^+ at intensity ~1.5×10^{14}W/cm^2 [83].

The second term in Eq.(3.2) is the electronic dispersion given by $\Delta k_{elec} \sim PqN_e r_e \lambda$ [81, 82], which besides P and q depends also on the free electron density per bar (N_e) in the interaction region, classical electron radius (r_e), and the wavelength (λ).

The third term in Eq.(3.2) is the geometrical phase shift (Gouy phase) contribution that depends on the laser focusing conditions, and it is given by

$\Delta k_{Gouy} \sim (q\text{-}1)\tan^{-1}(z/z_R)/z$ where z_R is the Rayleigh range and z is the displacement from the focal point along the laser beam [70, 84, 85].

The last term in Eq.(3.2), referred to as atomic phase, depends on the quantum path and is different for short and long trajectories [59]. This is given by $\Delta k_{dip} = -\alpha \nabla I$, [60] where ∇I is the variation of the intensity along the beam in the gas cell. For electrons following the short trajectory $\alpha \sim 2\times10^{-14} cm^2/W$ and for those travelling along the long trajectory $\alpha \sim 22\times10^{-14} cm^2/W$ [60, 61].

Evaluating all the contributions to the wave vector mismatch in Eq.(3.2) allowed us to determine the coherence length and the absorption length calculated from available data [86] (Figure 3.6). It is assumed that the long and short trajectories equally contribute to the total harmonic signals [61, 87].

Figure 3.3 and Figure 3.5 show the comparison of calculations with the 1D model and the experimental results for HHs orders pressure dependence for Ar and H_2, respectively. The results of calculations (red dashed lines) are in reasonable agreement with the experimental data (blue solid lines).

The calculations were performed with the 1D model of Eq.(3.1), assuming that for each harmonic A_q is constant. For the observed maximum harmonic output, the pressure at the gas jet was such that the concentration of the gas atoms was relatively high, providing a stronger output. On the other hand, the absorption and phase-mismatch were not yet affecting the HHG output too strongly.

One of the main difficulties of the harmonic generation is due to re-absorption of XUV radiation in the gas medium. Without the additional pumped cell enclosing the gas jet, the gas jet extends to a larger distance, thus increasing the re-absorption effect of the generated XUV radiation. This decreases the efficiency of the HHs. With the differential pumping, the gas density is more localized within the enclosing cell, and thus the HHs' propagation length within the region with elevated pressure is reduced, thereby reducing reabsorption.

An important point is that the maximum of the HHs' output peak was observed for about the same pressure value for all harmonic orders as shown in Figure 3.3 and Figure 3.5 for Ar and H_2, respectively. This indicates that reabsorption is not playing an essential role in the HHG signal, since otherwise the maximal outputs for different harmonics would correspond to different pressures.

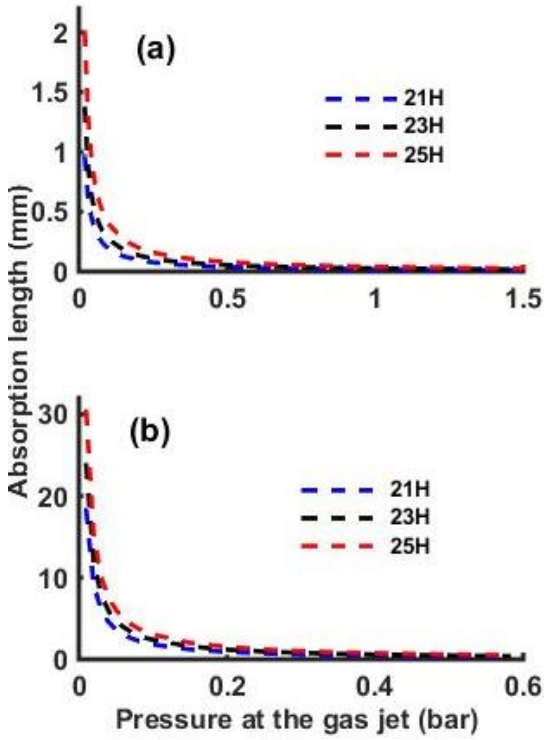

Figure 3.6 Absorption length (L_{abs}) as a function of gas jet pressure for 21st, 23rd, and 25th HHs. (a) for Ar gas, (b) for H_2 gas (blue dashed line for 21st harmonic, black dashed line for 23rd harmonic, and red dashed line for 25th harmonic)

3.5 Conclusion

In this study we experimentally investigated pressure-dependence effect on the output of HHG for two gases (Ar and H_2) and compared the experimental results with a 1D theoretical model. Argon is often used for HHG since it produces relatively high HHs outputs. Although Ar and H_2 have similar ionization potentials, they exhibited different HHs outputs and pressure dependences at the same experimental conditions. We have shown that at intensities ~1.5×10^{14}W/cm^2, and for our experimental conditions, the optimum pressures yielding a tenfold increase in the HH output are found to be ~0.2bar for Ar, and ~0.5bar for H_2, as compared to direct employment of the gas jet without a

differentially pumped cell. The HH signal in the case of H_2 is about 20 times lower than for Ar for the same experimental conditions. Maximal outputs for different harmonics are reached at about the same pressure values, which provides evidence that the XUV radiation reabsorption is relatively weak. The optimum pressure that maximizes the HHs signals reflects the trend of quadratic increase with the gas density on the one hand and the effect of the phase mismatch and absorption that tend to increase with pressure on the other hand [26, 88]. The observed experimental pressure dependences are in agreement with simulations based on the 1D model.

The described optimized XUV radiation source can find applications in bio-, and nano-imaging, investigations of fast dynamical processes in a pump-probe scheme as well as for spectroscopy experiments in the XUV region.

CHAPTER IV

HIGH HARMONIC GENERATION IN NE AND H_2 GAS MIXTURES*

4.1 Introduction

High harmonic generation (HHG) enables the production of coherent light in the extreme ultraviolet (XUV) spectral region. However, the radiation conversion efficiency from infrared to the XUV is low. We observed enhancement of HHG in gas mixtures of H_2 and Ne compared to pure gases H_2 or Ne. Our experiment shows that at intensities of ~1.5×10^{14}W/cm^2 and in mixtures of gases with significantly different ionization potentials (IP), the initial HHG takes place in the component with the lower IP (H_2), inducing excited states and facilitating ionization and HHG in the component with higher IP (Ne). We show that the combination of the two gas components results in an enhancement or suppression of the output of high harmonics as compared to pure gases, which is also confirmed by the employed phenomenological model.

A dramatically enhanced HHG in He^+ with simultaneous irradiation by the fundamental IR and the produced high harmonics (HHs), 13th or 27th, was theoretically described in [89] with enhancement factors of several orders of magnitude. This was attributed to the excitation of intermediate excited states in He^+ by an intense high harmonic order (13th or 27th). An enhancement effect up to a factor of ~4×10^3 was observed in a He-Xe mixture compared to pure He with the mixing ratio of the Xe and He partial

---

pressures being ~0.04 [90]. This enormous enhancement was ascribed to boosting the first ionization step of the three step model. In a dual-cell setup with cascade generation of HHs, i.e. first in Ar gas and then in Ne gas, an up to three-fold enhancement of the conversion efficiency of HHs was observed [91]. Such an increase was explained by the generation of a low-order harmonic (3^{rd}), provided that it has the proper phase required in agreement with phase matching conditions. However, it was also shown that the interaction of two gas components in a mixture can reduce HH output [92].

In this work, we report an improvement in conversion efficiency of the fundamental IR light into high harmonics by using a gas mixture consisting of a gas with low ionization potential (H_2 , I_p=15.4eV) [80] and another one with high ionization potential (Ne, I_p=21.6eV) [79]. The HHG in pure H_2 [93] and Ne [94, 95] is studied previously. The use of H_2 in the mixture is of particular interest since this is the simplest molecular system for comparison with theory [96, 97].

4.2 Experimental Setup and Results

Over the barrier tunneling ionization predicts a saturation intensity of $I_{sat}=2.2\times10^{14}W/cm^2$ for H_2 and $I_{sat}=8.7\times10^{14}W/cm^2$ for Ne [98]. To obtain intensities approaching this range, we use a Ti:sapphire laser system emitting pulses with a duration of ~50fs and having a central wavelength of 800nm, an output pulse energy of up to ~1mJ at a 1kHz repetition rate. Radiation is focused onto a gas jet of pure H_2, Ne, or their mixtures using a lens with a focal length of 40cm. The high harmonics are detected by an XUV McPherson spectrometer with the MCP output followed by a fluorescent screen and imaged by a CCD camera. In all experiments a peak laser intensity of $1.5\times10^{14}W/cm^2$ is used. The

experiments are performed at different partial pressures and for various total pressures of the mixtures and show an enhancement or reduction of the HH output compared to using pure gases. To achieve this the backing gas pressures are varied, while all other experimental conditions are kept identical. Each result is averaged over five measured spectra each of which taken with an integration time of 1s, except for measurements with pure Ne that requires the longer integration time of 30s due to high ionization potential of Ne compared to H_2.

The experimental setup (gas line and mixture bottle) as shown in Figure 4.1 is completely exhausted by a separate roughing pump (Oerlikon, Scroll 15), and they are baked by a heating gun before the experiment to eliminate the background gas contamination. Then, the gas mixture is prepared, and it sends through the gas jet for harmonic generation. The volume of the small size lecture bottle (mixture bottle) is $V=\pi r^2 L=376cm^3$, where r and L are radius and length of the mixture bottle, respectively.

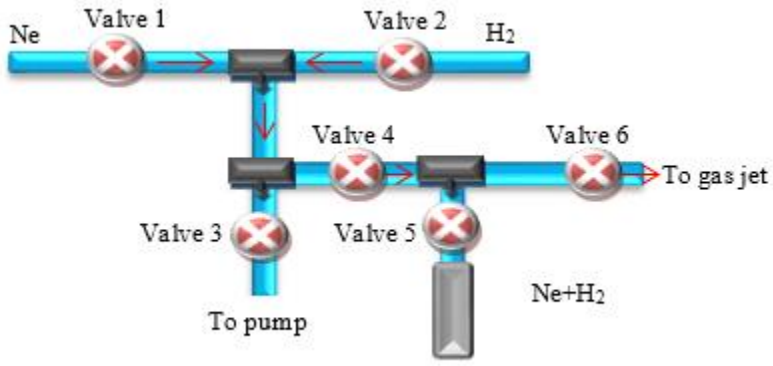

Figure 4.1 Schematic demonstration of the gas mixture setup

The pressure at the periphery of the interaction chamber was kept low enough (2.5×10^{-3}mbar) to reduce the re-absorption of XUV radiation produced by HHG. The local pressure (p_j) at the gas jet where HHs are produced is about 50mbar, which is estimated under the assumption that the gas jet is proportional to the pressure in the interaction chamber by measuring the temporal dependence of the gas consumption from a small size container with similar initial backing and interaction chamber pressures [58]. When the laser beam is focused on the gas jet, the emission of high harmonics of orders from 11^{th} to 21^{st} is observed, Figure 4.2. At a laser intensity of 1.5×10^{14}W/cm^2 only weak HHs are observed in Ne gas (green curve in Figure 4.2). In the gas mixture (blue curve in Figure 4.2) with 37.5% Ne and 62.5% H_2 partial pressures a noticeable enhancement of the HH output (HH output normalized to output for pure H_2) of up to a factor ~1.5 (for 11^{th} HH) occurred compared to the case when only pure H_2 gas (red curve in Figure 4.2) at the same total backing pressure is measured. The enhancement factor for Ne is more significant ($\sim3\times10^3$).

Figure 4.3 shows the enhancement factors of harmonics from the 11^{th} to the 21^{st} order for gas obtained by mixing H_2 with the backing pressure fixed at ~0.7bar and Ne with the backing pressure increasing in steps of ~0.4bar up to ~2.8bar. The pressure in the interaction chamber is kept at 2.5×10^{-3}mbar, which corresponded to the pressure in the gas jet of 50mbar. The HH output was normalized to the output of pure H_2 at the same total backing pressure for all HHs. All data in Figure 4.3 show an initial rise of the enhancement factor with increasing Ne partial pressure (reaching the maximum in the range of ~30-60%), which is followed by a drop in the enhancement factor when the partial pressure of

Ne exceeded ~60%. The maximum values of the enhancement factor varied from ~1.2 for 11H to ~2 for 21H.

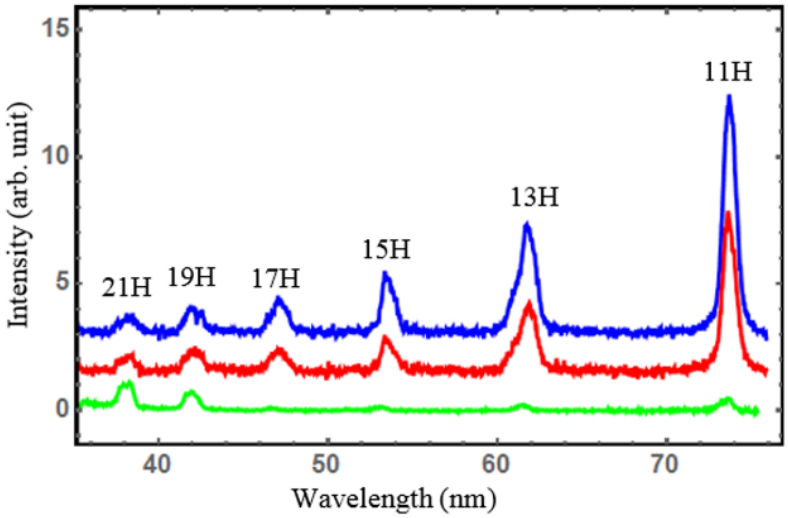

Figure 4.2 Measured HHG spectra (from top to bottom) for a mixture with partial pressures 37.5% Ne and 62.5% H_2 (blue), pure H_2 (red), pure Ne (green, measured with 30s integration time and magnified by a factor of 10). The spectra have the same baseline and are vertically shifted for better viewing. The total backing pressure is 2.8bar, and the gas jet pressure is p_j~50mbar

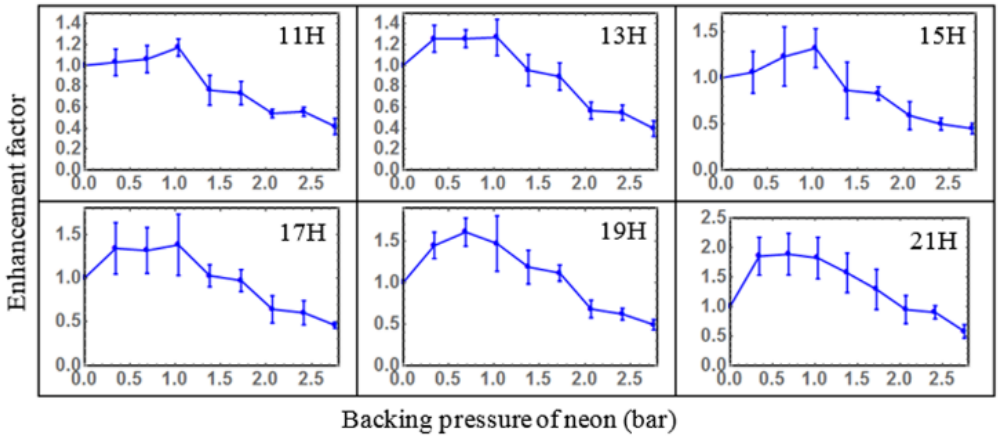

Figure 4.3 Enhancement factor for harmonics from 11th to 21st, i.e. their output normalized to output for pure H_2, in gas mixtures of Ne and H_2 with backing pressure of Ne increasing in steps of 0.4bar, and the pressure of H_2 fixed at 0.7bar. The solid line is a guide to the eye

The enhancement is also studied for a fixed total pressure where the Ne partial pressure is increased in 12.5% increments. It is assumed that the gas mixture ratio, which is determined by the partial pressures in the container before the gas jet is preserved in the gas jet. This is carried out for three different pressures in the gas jet chamber that are set by changing the gas flow while the total backing pressure is fixed at 2.8bar. The most pronounced enhancement effect is observed at intermediate values of Ne concentrations and decreased with increasing total pressure in the gas jet chamber. For the value of this pressure of 1×10^{-3}mbar (Figure 4.4 (a)) the peak is observed at 37.5% of Ne and 62.5% of H_2, while for the higher pressure of 5×10^{-3}mbar Figure 4.4 (c)), the maximum shifted to lower Ne concentration: ~12.5% of Ne and ~87.5% of H_2. The HH output drop at Ne concentrations above a value which depended on the gas jet chamber pressure: above ~60% for 1×10^{-3} mbar (p_j=20mbar), above ~40% for 2.5×10^{-3}mbar (p_j=50mbar) and above ~20% for 5×10^{-3} mbar (p_j=100mbar).

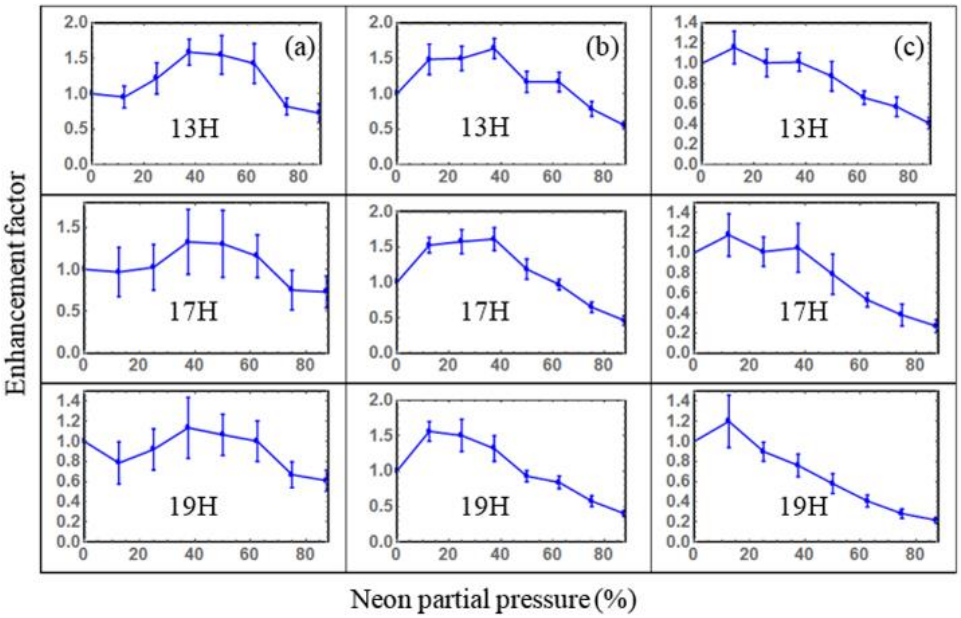

Figure 4.4 Enhancement factor for 13th, 17th and 19th harmonics in gas mixtures of Ne and H_2 for three different pressures (columns) in the gas jet: (a) p_j=20mbar, (b) p_j=50mbar and (c) p_j=100mbar. The total backing pressure was 2.8bar. The vertical axis shows HH output normalized on output for pure H_2; the horizontal axis shows in percentage the Ne partial pressure in the mixture

4.3 Interpretation, Model Simulation and Discussion

We attribute the observed HHG enhancement effect to HHG in hydrogen molecules, which have a lower ionization potential; this booster XUV radiation induces excited states in Ne, which together with the IR radiation facilitates ionization of Ne. Because of the larger ionization potential of Ne, there is weak HH signal from pure Ne gas with the used driving laser parameters, whereas for H_2, a significant HH output is theoretically [99] and experimentally [93] found at this intensity level. The ionization of Ne can be enabled via several channels: (1) the generated 11th harmonic leads to a resonant transition from the ground $2p^6$ state of Ne to an intermediate 3s state, from which the ionization can then be performed with a photon of the third harmonic; (2) the 13th harmonic can excite from the

ground $2p^6$ state to a 3d state with subsequent ionization by a single photon of the fundamental radiation; (3) direct multiphoton excitation of other than 3s and 3d energy levels in Ne; (4) production of an excited state followed by tunneling ionization from this excited state, which has a higher probability than from the ground state; (5) generation of low order harmonics (i.e. 3^{rd}) that can enhance or reduce the ionization and HH output due to various phase matching conditions with respect to the field at the fundamental wavelength [100]. We note that the laser-induced dynamic Stark shift also affects the probabilities of the induced transitions [101]. Any significant contribution of collisional energy transfer is highly unlikely because of the extremely short interaction time, which is also confirmed by the fact that the HH enhancement effect does not necessarily increase with increasing gas pressure.

A careful consideration of the possible ionization channels allows selection of only those phenomena that are most likely. The first step of channels 1 and 4 of the $2p^6 \rightarrow 3s$ transition has the lowest photon multiplicity (11 photons) compared to other transitions (channels 2, 3) and therefore should have the higher probability. The transition $2p^6 \rightarrow 3d$ has somewhat higher photon multiplicity (13 photons) and thus should have lower probability. For channel 5 a strong dependence on the gas pressure that allows to tune the phase matching between the fundamental and low order harmonics can be expected, as is observed in Ref. [102], however, we observe only a rather gradual pressure dependence. Consequently, channels 1 and 4 through the excitation of $2p^6 \rightarrow 3s$ transition as the first step are the remaining candidates to dominate the ionization process. There is the difference between these two channels in the expected dependence on the density of the

low IP gas component (H_2). For channel 1 the probability of the transition $2p^6 \rightarrow 3s$ can be expected to be proportional to the intensity of the respective XUV resonance radiation, which for coherent summation of contributions from individual molecules should be proportional to the square of the density of H_2 molecules. For a two-step ionization process this leads to forth-order power dependence, provided that neither of the two transitions experiences saturation. For channel 4 with a single excitation step a square dependence for the ionization probability can be expected.

Using the approach outlined in Ref. [92], we have developed a phenomenological 1D model and applied it to describing HHG for a mixture of gases (H_2 and Ne). We assume that H_2 gas (with low IP) is ionized and produces HHs first, so that the produced HHs facilitate the HHG in Ne gas (with high IP), together with the incident IR pulse. The output of HH of order q propagating in the x-direction is described by

$$I_q = \left| \int_0^{l_m} A_q(x) \times \exp\{-\int_x^{l_m} [x'/l_a(x') + ix'/l_c(x'))] dx'\} dx \right|^2 \tag{4.1}$$

where $A_q(x)$ is the complex amplitude of the partial atomic contribution to the HH output from the element of the medium in the longitudinal direction dx, and l_m is the total length of the gaseous medium, which affects the HHs' propagation. For a mixture of two gases using the description of Ref. [90], we assume

$$A_q(x) \sim \left(n_{H_2} d_{H_2} a_{H_2} + n_{Ne} d_{Ne} a_{Ne} e^{i\Delta\varphi} \right) E^{\gamma/2} \tag{4.2}$$

where $n_{H_2,Ne}$ are the molecule densities of H_2 and Ne gases respectively, $d_{H_2,Ne}$ are the induced dipoles, and $a_{H_2,Ne}$ are the probability amplitudes of the electron recombination for the

species of the H_2 and Ne, which take place with phases $\varphi_{H_2,Ne}$ respectively, so that $\Delta\varphi=\varphi_{H_2}-\varphi_{Ne}$. Here we assume that $n_{H_2,Ne}$ have the following distribution

$$n_{H_2,Ne}=n_{0H_2,0Ne}[l_{m0}^{\ 2}/(x^2+l_{m0}^{\ 2})] \tag{4.3}$$

where $n_{0H_2,0Ne}$ are the maximal densities of H_2 and Ne in the gas jet, $l_{m0}<<l_m$ and that the laser field E has a longitudinal spatial distribution

$$E=E_0\,[l_R^2/(x^2+l_R^2)]^{0.5} \tag{4.4}$$

Here l_R is the Rayleigh range, which determines the extension of the high intensity region with the main contribution to the HHG process. The power law for the dependence of the HH output on intensity around value $\sim 1.5\times10^{14} W/cm^2$ is experimentally measured to be $\gamma\approx 3$.

In Eq. (4.1) the absorption length is $l_a=\alpha^{-1}$, where α is the absorption coefficient, and the coherence length is $l_c=\pi/\Delta k$, where the wave vector mismatch Δk between infrared and XUV light depends on several contributions [81, 82]. For the 19th harmonic (used in further simulations and comparison with experimental results) the largest contribution to Δk is expected from the difference of the refractive indexes for the fundamental and HH radiation **[**2**]**, which is proportional to the gas density. In general (for other harmonics, densities or other gas mixtures), this relation may not hold, then also other contributions to the mismatch Δk must be taken into account.

At relatively low pressures the contributions to the total absorption and Δk from both gases sum up. Consequently, we use the approximations: $l_a\sim\left(l_{a,H_2}^{-1}+l_{a,Ne}^{-1}\right)^{-1}$, and

$l_c \sim \left(l_{c,H_2}^{-1} + l_{c,Ne}^{-1}\right)^{-1}$, where $l_{a,H_2;Ne}$ and $l_{c,H_2;Ne}$ are absorption and coherence lengths for H_2 and Ne gas, and they are calculated for partial pressures $p_{H_2;Ne}$ in the assumption that $l_{a,c;H_2,Ne} \sim l_{a,c;0H_2,0Ne}(p_0/p_{H_2,Ne})$ with $l_{a,c;0H_2,0Ne;}$ being the absorption or coherence length for the reference pressure of p_0~50mbar for H_2 or Ne respectively. The corresponding molecule density for p_0 we label as n_0.

When species with low IP are added to species with high IP, the probability of ionization of the latter also changes due to HHG in the former. In two-step ionization (i.e. with 11th HH to an intermediate level and then ionization with 3rd HH) the total probability will be proportional to the product of the intensities of 11th and 3rd HHs, and since due to the coherent superposition, each is proportional to the square of the density of H_2 gas (we assume absence of any saturation effects, because the efficiency of HHG is low), then for Δa_{Ne}, the contribution to the ionization probability amplitude of Ne due to HHG in H_2, we accept $\Delta a_{Ne} \sim n_{H_2}^2$, with n_{H_2} being the density of H_2 gas. Then, the total probability amplitude of ionization of Ne gas, a_{Ne} can be presented as

$$a_{Ne} \sim a_{Ne,d} + \Delta a_{Ne}, \Delta a_{Ne} = Q a_{H_2} n_{H_2}^2 \qquad (4.5)$$

where Q is a proportionality factor. The term due to direct ionization of Ne gas, $a_{Ne,d}$ is small which is confirmed by our experimental data shown in Figure 4.2, from which an estimate $d_{Ne} a_{Ne,d} / d_{H_2} a_{H_2} \sim 0.08$ is inferred.

When $l_{m0} >> l_a$ or $l_{m0} >> l_c$, the output is reduced due to significant absorption and accumulated phase mismatch. For a uniform gas medium with constant gas density, the

expression of Eq. (4.1) can be factorized so that the factor due to local HH and the propagation factor can be considered separately [90, 92] with $|A_q|^2$ constant within the length of the medium (l_m). The propagation factor for a uniform medium can show strong oscillations, originating from the stepwise density distribution. For a smooth density distribution, as is realized in our experiments, the oscillations are suppressed, which is also confirmed by our observations and calculations. Based on this model and our experimental results, we perform simulations of the dependences of the HH output (19th HH) on Ne pressure and Ne fractional content similar to Figure 4.3 and Figure 4.4. The following values are used for the calculations $l_{a,0H_2}$=10mm, $l_{c,0H_2}$=0.4mm, $l_{a,0Ne}$=1.8mm, $l_{c,0Ne}$=2.2mm, l_{m0}=l_R=0.4mm. As a fitting parameter we use $\left(Qn_{0H_2}^2 d_{Ne}/d_{H_2}\right)$ with the best fitting value ~4.6.

Figure 4.5 shows the calculated harmonic enhancement as a function of the Ne pressure for the 19th harmonic (black solid line) in comparison with the experimentally observed dependence (green triangles with connecting line; data from Figure 4.3). The calculation is performed employing Eqs. ((4.1)-(4.5)) for the 19th harmonic (λ~42nm) for which the refractive index and absorption could be obtained from the literature [103, 104]. The phase difference $\Delta\varphi$ can be expected to be different for different harmonics [105], and fitting experimental data for the 19th harmonic is consistent with the value $\Delta\varphi = 1.4\text{rad}$. The red dashed line shows the result of calculations with the same Eqs. ((4.1)-(4.5)), but with factor $Q=0$. The difference between the black solid line and the red dashed line shows the effect of the additional contribution due to initial HHG in H_2 that boosts also HHG in

Ne and thus overall the enhancement factor, providing a better agreement to experimental data.

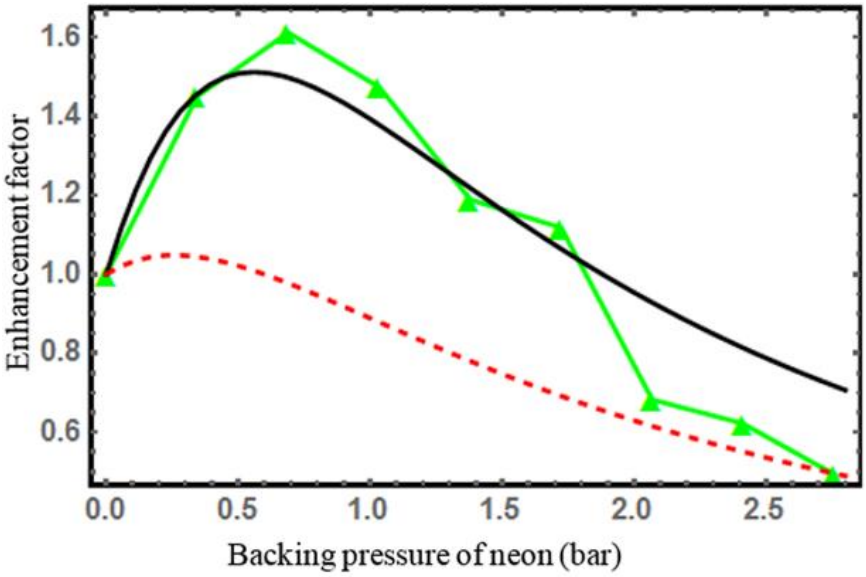

Figure 4.5 Calculation of the dependence of the enhancement factor for the 19th harmonic on the Ne pressure for experimental conditions of Figure 4.3. Black solid line is the result for the model of Eqs. ((4.1)-(4.5)), red dashed line is a similar calculation, but with factor Q=0, and green triangles are the experimental results for the 19th harmonic from Figure 4.3 (green solid line is a guide to the eye)

Figure 4.6 shows results of the model calculation of the enhancement factor for varying partial pressure of Ne. The meaning of the shown curves is similar to those in Figure 4.5. Again, the black solid line that takes into account the boosting effect of the initial HHG in H_2 gives a better agreement with experimental data. Note that the regression analysis for the fitting curves in Figure 4.5 and Figure 4.6 (black solid line for both figures) gives R-squared values of 96% and 89%, respectively.

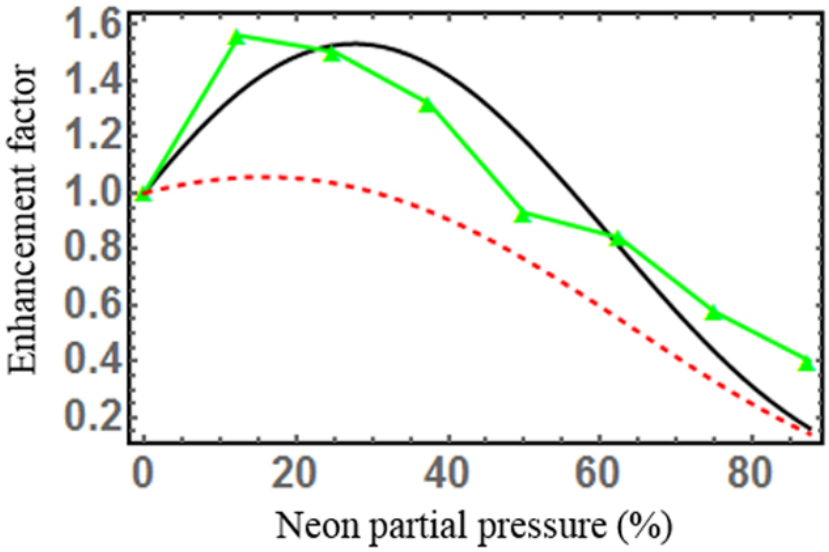

Figure 4.6 Calculation of the dependence of the enhancement factor for the 19th harmonic on Ne fractional pressure for the experimental conditions of Figure 4.4 (b). Black solid line is the result for the model of Eqs. ((4.1)-(4.5)), and red dashed line is a similar calculation, but with factor Q=0, and green triangles are the experimental results for the 19th harmonic of Figure 4.4 (b) (green solid line is a guide to the eye)

The output of HH can be enhanced or reduced depending on the phase relations of the partial contributions from gas components. The initial drop in the enhancement, especially pronounced at a lower pressure, (see Figure 4.4 (a)) can be explained by the phase shift between partial contributions to HHs from two different species. Thus, in a gas mixture, a component with well-known characteristics can serve as a probe to test the characteristics of another component contained in a mixture, which has not been well studied. The dipole phase shift reflects also the contributions of the short and long electron trajectories and varies for different harmonics, and thus contributes also to the HH chirp [105]. The maximum in the HHs outputs at intermediate fractional pressures of Ne arises from an increase of the contribution of Ne, which on the one hand requires the initial HH

generation in H_2 and thus significant density of H_2 molecules, and on the other hand requires a considerable concentration of Ne atoms as well. With an increase in Ne pressure, the HH absorption becomes more and more important [106, 107], and reduces the overall HH output as is observed also in the experiment (Figure 4.3 and Figure 4.4).

4.4 Conclusion

In conclusion, the HHG yield in mixture of H_2 and Ne are studied for various total and partial pressures. We observed up to a 2-fold enhancement of HHs output compared to pure H_2 and up to ~3×10^3 enhancement compared to pure Ne when using a laser pulse with a peak intensity of 1.5×10^{14} W/cm^2. The enhancement effect is most pronounced for mixtures with intermediate partial pressures of Ne (in the range 12-40%). The maximum output is observed to shift to lower partial pressures of Ne with increasing total pressure. We relate the enhancement mechanism to a more efficient ionization process of Ne due to HHs produced initially in H_2. Among different possible ionization channels, ionization through intermediate excited states seems to be the most likely mechanism. Thus, mixing of gases with low and high ionization potentials opens new possibilities for studying relative contributions of different gas components and for enhancement of the HHG process efficiency without any increase in the driving laser energy.

CHAPTER V

COMPARISON OF HHG SIGNAL FROM ALIGNED NITROGEN AND ACETYLENE MOLECULES

5.1 Introduction

Studies of the high harmonic generation with the molecular alignment technique can provide not only an understanding of the microscopic and macroscopic processes but also provide sensitive information about the electronic and geometrical structure of the molecules [43] with a high temporal and spatial resolution. HHG from randomly aligned molecules have similar characteristic to HHG from atoms, however HHG for aligned molecules is influenced by the angle between the molecular axis and the polarization direction of the laser field [108, 109]. This spectroscopy method can be used to determine molecular rotational constants with high precision, and it can reveal important structural analysis about large molecules [110]. Studies on aligned molecules [111, 112] have attracted interest due to variety of applications such as imaging of molecular structures [113], controlling chemical reactions [114], pulse compression [115] nanolithography with molecular beams [116], and quantum interference [117, 118]. HHG for the field-free aligned molecules can be experimentally produced by interaction of the molecules with a short and relatively weak pulse to create a rotational wave packet. HHG with aligned molecules is observed when a delayed high intensity laser pulse is used to produce HHG at different delay time after the pre-aligning pulse when there is a rapid change in alignment of molecule.

HHG can microscopically explained with three step model, ionization and recombination of an electron, but it also depends on the macroscopic condition that depends on the alignment of the molecules, i.e. phase matching. Phase matching of HHG depends on the harmonic order and on several experimental parameters, namely the geometry, the atomic and molecular dispersion, the absorption coefficient of the gas medium at different harmonics, the ionization fraction, and the atomic and molecular intensity dependent dipole phase. Some of the above parameters depend on the molecular alignment and the molecular structure. Therefore, in addition to microscopic single atom response to the laser field the macroscopic phase matching of the harmonics play crucial role in determining the HHG from the aligned molecules.

When the linear molecules are excited by a short laser field, a modulation of the refractive index in space and time is induced along the polarization direction of the laser electric field. In this study, we experimentally investigate the alignment dependent high harmonic (HH) spectrum generated from aligned molecules around the full and half revival time. We theoretically report both the microscopic single atom response and the importance of macroscopic phase matching condition on the study of HHG from aligned nitrogen and acetylene molecules.

5.2 Alignment of Molecules with a Pump-Probe Intense Laser Field

There is an alignment of molecules if an intense laser field interacts with molecules. There are two kinds of molecular alignment: an adiabatic alignment and a non-adiabatic alignment. Adiabatic alignment occurs when the laser pulse duration is much longer than

the rotational period of the molecule. On the other hand, non-adiabatic alignment requires that a laser pulse duration is much shorter than the rotational period of the molecule.

5.2.1 Adiabatic Alignment

The laser pulse duration is much longer than the rotational period of the molecules. In this adiabatic alignment, the degree of alignment follows the instantaneous laser intensity, and therefore the alignment depends on the intensity, the wavelength, and the duration of the optical field [113]. Adiabatic alignment has experimentally some advantage. For instance, the alignment lasts as long as the laser field is applied, but using an intense laser beam can destroy the alignment process because the duration of the strong field is so long compared the rotational period of the molecule.

5.2.2 Non-Adiabatic Alignment

Contrary to adiabatic alignment, non-adiabatic alignment occurs when the optical field pulse duration is much shorter than the rotational period. This alignment is also known as field free alignment as the presence of the laser field is very short.

In a classical model, the laser electric field $\vec{E}(t)$ induces a dipole moment $\vec{d}(t) = \alpha \vec{E}(t)$ in the molecule, and the dipole experiences a torque $\vec{\tau}(t) = \vec{d}(t) \times \vec{E}(t)$ [113] where α is the polarizability tensor of the molecule. This torque leads the alignment of the molecule along the polarization axis in the presence of the laser field. The polarizability can be described by a polarizability parallel $\alpha_{\parallel}$ to and a polarizability perpendicular $\alpha_{\perp}$ to the molecular axis. The polarizability $\Delta\alpha$ is defined as the difference between parallel

$\alpha_{\parallel}$ and perpendicular $\alpha_{\perp}$ polarizability components with respect to the molecular axis. The classical model explains the alignment of the molecule under the field free condition, but it is unable to present the revival which has been observed due to the discrete rotational energy levels [110, 119].

In the quantum mechanical model, a coherent rotational wave packet is created if the molecule experiences an impulse toward alignment, and this rotational wave packet is preserved after the laser pulse are gone since the laser pulse duration is much shorter than the rotational period of molecule [120].

5.3 Theory (Rotational Wave Packet Dynamics)

We consider that a linear molecule is subjected to a linearly polarized laser field with the Gaussian distribution $\varepsilon(t)=g(t)\varepsilon_0\cos(\omega t)$, where ε_0 is the electric field amplitude, ω_0 is the laser central frequency, and $g(t)=\exp\left[(-2\ln 2)t^2/\tau^2\right]$, τ is the pulse duration. Therefore, the time-dependent Schrödinger equation governing a molecule subject to an intense laser field can be written based on the rigid rotor model as [114, 121]

$$i\hbar\frac{\partial}{\partial t}\Phi_{JM}(t)=\left(H_R^{(0)}+V_{N\text{-}L}(t)\right)\Phi_{JM}(t) \tag{5.1}$$

where the field-free rotational Hamiltonian of the molecule $H_R^{(0)}=B\hat{J}^2$ with B and $\hat{J}$ being the rotational constant and the angular momentum operator, respectively; $V_{N\text{-}L}(t)=-\frac{1}{2}\left(\Delta\alpha\cos^2\theta+\alpha_{\perp}\right)\left\langle\varepsilon^2(t)\right\rangle$ is the interaction term of a linear symmetric top molecule subjected to linearly polarized laser field $\varepsilon(t)$ of the pump pulse [114, 122]. $\Delta\alpha$

is the difference between parallel and perpendicular polarizability components with respect to the molecular axis, and θ is the angle between the molecular axis and the laser field polarization. The time evolution of a rotational wavefuction $\Phi(t)$ can be expanded in terms of a series in free-field rotor functions $|\mathrm{JM}\rangle$ with eigen energy $\mathrm{E_J}=\mathrm{hBcJ(J+1)}$, B is the ground state rotational constant. The evolution of the initial state, $|\Phi_{\mathrm{J_0M_0}}(\mathrm{t})\rangle$ created by the pump pulse is described by an expansion in the rotational wave packets states [113, 123]

$$|\Phi_{\mathrm{J_0M_0}}(\mathrm{t})\rangle = \sum_{JM} \mathrm{d}_{\mathrm{JM}}^{\mathrm{J_0M_0}}(\mathrm{t}) \exp\left(-\mathrm{i}\frac{\mathrm{E_J t}}{\hbar}\right)|\mathrm{JM}\rangle \tag{5.2}$$

where the expansion coefficients $\mathrm{d}_{\mathrm{JM}}^{\mathrm{J_0M_0}}(\mathrm{t})$ are determined by solving the set of differential equations [124] stemming from the time-dependent Schrödinger Eq. (5.1).

When there is a laser field, the coefficients are time independent. Each constituent free-field rotor state $|\mathrm{JM}\rangle$ accumulates phase with a different angular frequency when interacting with the aligning laser pulse. These rotational $|\mathrm{JM}\rangle$ states rapidly dephase with respect to each other and the initial net alignment quickly disappears. Since the wave packet evolves in a field-free, the $|\mathrm{JM}\rangle$ states starts to re-phase. The alignment dynamics comes from interference between these states. Once the accumulated phase of $|\mathrm{JM}\rangle$ state are equal to each other, the initial alignment is reproduced.

The degree of alignment is characterized by the alignment parameter $\langle\cos^2\theta\rangle$, where θ is the angle between the molecular axis and the laser polarization direction

[113]. $\langle \cos^2\theta \rangle = 1$ represents complete alignment along the polarization axis, $\langle \cos^2\theta \rangle = 0$ shows perfect alignment perpendicular to the polarization axis, and $\langle \cos^2\theta \rangle = 1/3$ indicates to an isotropic distribution. In other words, if $\langle \cos^2\theta \rangle > 1/3$, the molecule is mostly aligned along the laser polarization, and if $\langle \cos^2\theta \rangle < 1/3$, the molecule is predominantly aligned perpendicular to the laser polarization [125, 126]. Thus, the degree of alignment evolving from a given initial state $|J_0 M_0\rangle$ is characterized by

$$\langle \cos^2\theta \rangle_{J_0 M_0}(t) = \langle \Phi_{J_0 M_0}(t) | \cos^2\theta | \Phi_{J_0 M_0}(t) \rangle \tag{5.3}$$

Before the interaction, the gas ensemble is assumed to be in thermal equilibrium with Boltzmann distribution at temperature T. In quantum-mechanical approach the ensemble is described by a statistical mixture of states $|J_0 M_0\rangle$ angular momentum with J_0 =0, 1, 2, ... and $M = -J_0, -(J_0 - 1), ..., 0, ...(J_0 - 1), J_0$ with the probabilities of these states following Boltzmann distribution $P_{J_0} \sim g_{J_0}(2J_0+1)\exp(-E_{J_0}/kT)$, where E_{J_0} is the rotational energy of $|J_0 M_0\rangle$ state and k is the Boltzmann constant. The $(2J_0+1)$ term accounts for the degeneracy within a given J_0 state. In the case of a molecule containing two identical nuclei, g_{J_0} is the relative weight between odd and even J states, which comes from nuclear spin statistics as an additional factor [127, 128]. Finally, the alignment degree of the ensemble, at temperature T, can be found by averaging the alignment degree of a single initial state (Eq. (5.3)) over the Boltzmann distribution, including spin nuclear statistics, as

$$\left\langle\left\langle \cos^2\theta \right\rangle\right\rangle(t) = \frac{\sum_{J_0}\sum_{M_0=-J_0}^{J_0} g_{J_0}\left\langle \cos^2\theta \right\rangle_{J_0M_0}(t)\exp\left(-BJ_0\left(J_0+1\right)/kT\right)}{\sum_{J_0}\sum_{M_0=-J_0}^{J_0} g_{J_0}\exp\left(-BJ_0\left(J_0+1\right)/kT\right)} \tag{5.4}$$

where $\left\langle \cos^2\theta \right\rangle_{J_0M_0}(t)$ is the alignment degree for a single individual state. For nitrogen molecule, g_{J_0} =6 for even J's and g_{J_0} =3 for odd J's [127, 128]. The ratio of even to odd states is therefore 2:1, whereas for acetylene, both odd and even J states are populated with the ratio of odd J-states to even J-states 3:1 [129]. It is important to note that the alignment degree is sensitive to molecular properties (i.e. rotational constant B and nuclear statistics g), the "kick" parameter proportional to $\Delta\alpha$ and the laser flux [130], and the ensemble temperature (T).

5.4 Experimental Details

The experiments have been performed by using an amplified Ti:Sapphire laser system generating with a pulse duration of 50fs and a central wavelength of 800nm having output energy per pulse up to 15mJ at a 10Hz repetition rate. The output of the laser energy is split into two arms as a pump beam and a probe beam by using 50% beam splitter, and a motorized translational stage on the probe arm is used to scan pump-probe delay. A polarizer is placed on the pump arm to reduce the intensity of the pump beam with respect to the probe beam.

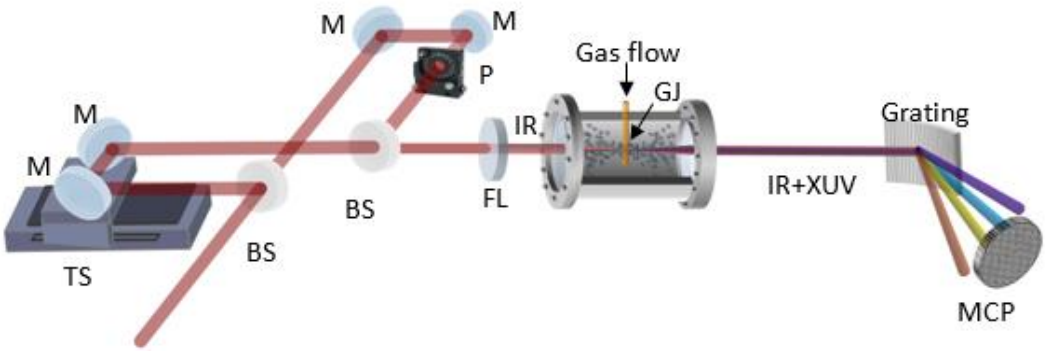

Figure 5.1 Schematic illustration of the experimental setup for molecular alignment. BS: beam-splitters, TS: translational stage, λ/2: half wave plate, M: flat mirrors, P: Polarizer, FL: Focusing lens, GJ: gas jet

The pump beam energy varies between 0.5-0.6mJ, and the probe beam energy is fixed ~0.8mJ. Both beams are spectrally and spatially overlapped on another 50% beam splitter. These overlapped beams are focused into a gas jet (~1mm thickness) with a ~40cm focal length lens. The gas pressure in the gas jet is set ~50mbar that is optimum operating pressure for the experimental HHG setup, and the pressure of the interaction chamber is kept low enough (2.5×10^{-3}mbar) to reduce the reabsorption of XUV radiation produced by HHG. The generated HH radiation travels through a grating where it is spectrally dispersed. The portion of the dispersed radiation is detected by an imaging micro-channel plate (MCP). The detected harmonics are output by a fluorescent screen, and harmonics images were captured by a CCD camera. All devices are controlled simultaneously by using a LABVIEW program. We integrate the harmonics in the direction perpendicular to the dispersion axis to generate the high-harmonic spectrum. The experimental setup discussed in this paper is presented in Figure 5.1. The intensity of the pump (aligning) beam is 9×10^{13}W/cm^2, and the intensity of the probe beam is 1.6×10^{14}W/cm^2. Both pump and probe beams are linearly polarized.

5.5 Results and Discussion

We run the experiments to investigate how the structures of the rotational half and full revival of N_2 and C_2H_2 molecules change with pump-probe delay scans. Measurements for both gases were made for different harmonic orders which showed evidence of similar magnitude of alignment effect. We presented here only harmonics orders from 15^{th} to 19^{th} orders for both gases, resulting in the optimum signal-noise ratio. In Figure 5.2 shows the revival of N_2 gas for harmonic from 15^{th} to 19^{th} orders. We observe the half revival around 4.2ps (left hand side of Figure 5.2) and full revival around 8.4ps (right hand side of Figure 5.2).

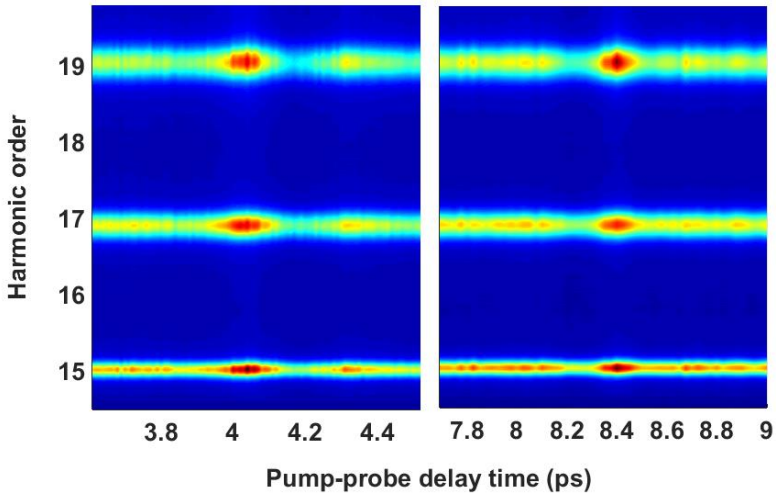

Figure 5.2 Different harmonic orders (15^{th}, 17^{th}, and 19^{th}) as a function of pump-probe delay at half and full revival for N_2 molecule. Bright colors show the enhancement of harmonic yield caused by the aligning pulse

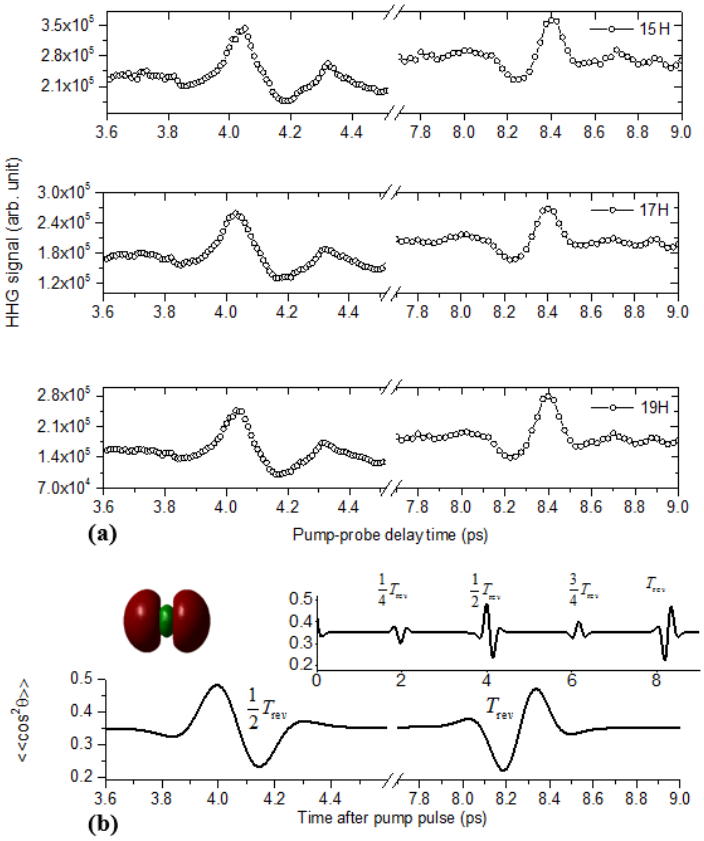

Figure 5.3 Temporal evolution of the rotational wave packet in N_2. (a) observed high harmonic signal from 15th to 19th harmonics. (b) calculated molecular alignment parameter $<<\cos^2\Theta>>$

Neutral nitrogen molecule has σ_g HOMO symmetry, where the easiest place to donate electrons. It has no nodal plane along internuclear axis. The polarization of pump and probe pulses are parallel to each other so molecular ionization rate is supposed to be maximum when molecules are aligned along laser polarization direction for the molecules have maximum electron density along internuclear (molecular) axis, and it makes possible to eject electron easily. So, our measured HH intensity (in Figure 5.3-a) modulates in phase with time dependency of molecule alignment after the pump (aligning) laser pulse (in

Figure 5.3-b). The harmonic intensity is enhanced when the molecule is aligned along the laser polarization direction, and it increase the harmonic efficiency about ~2 fold compared to the anti-aligned N_2 with respect to the laser polarization direction as seen in Figure 5.3-a.

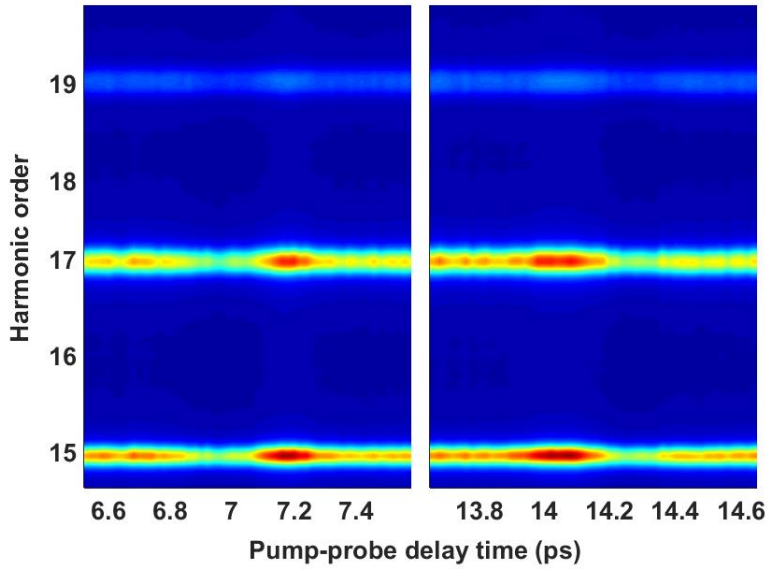

Figure 5.4 Different harmonic orders (15^{th}, 17^{th}, and 19^{th}) as a function of pump-probe delay at half and full revival for C_2H_2 molecule. Bright colors show the enhancement of harmonic yield caused by the aligning pulse

For the C_2H_2 molecule, the structures of half and full revival with respect to the pump-probe delay for different harmonics were studied. Figure 5.4 shows the revival of C_2H_2 gas for harmonic from 15^{th} to 19^{th} orders. We observe the half revival around 7ps (left hand side of Figure 5.4) and full revival around 14ps (right hand side of Figure 5.4).

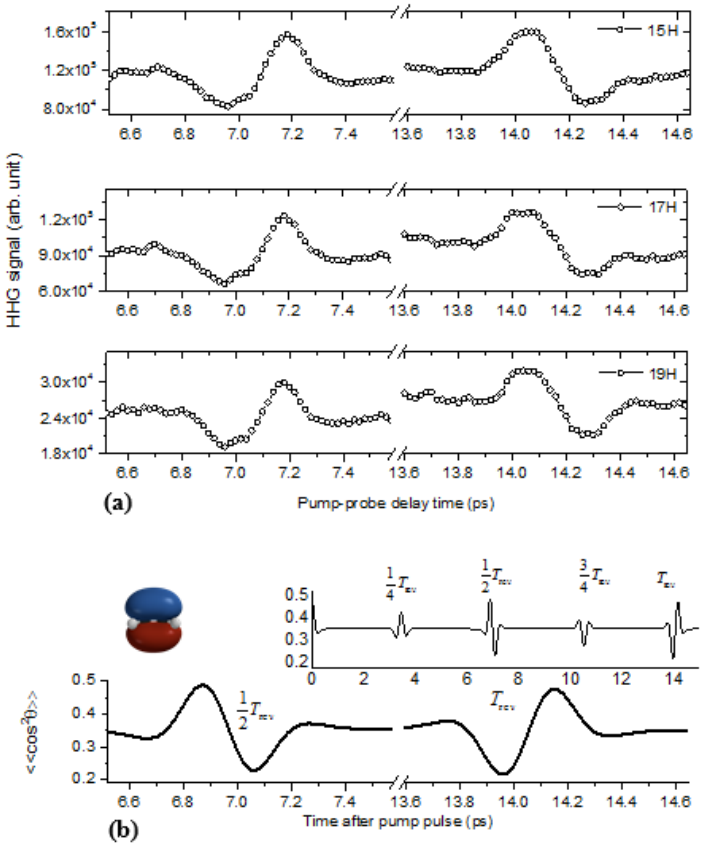

Figure 5.5 Temporal evolution of the rotational wave packet in C_2H_2. (a) Observed high harmonic signal from 15th to 19th harmonics. (b) Calculated molecular alignment parameter <<cos^{2}Θ>>

We can clearly see that the experimental result of molecular revivals of C_2H_2 molecules at half revival and full revivals (Figure 5.5-a) are in good agreement with the calculated time dependency of molecular alignment $\langle\langle \cos^2\theta \rangle\rangle$ parameter (Figure 5.5-b) but in reverse phase structure. So the harmonic intensity for C_2H_2 molecule is maximum when the molecule is anti-aligned along the laser polarization direction, and it increases the harmonic efficiency about ~2 fold compared to the aligned C_2H_2 with respect to the laser polarization direction as seen in Figure 5.5-a. This can be understood from HOMO

of acetylene which is dominated by π_u orbital [131]. π_u molecular orbitals have electron density surrounding the bond axis (increased electron density above/below internuclear axis), with a node along the internuclear axis. Then, we can conclude that the reverse structure of C_2H_2 with respect to the time dependency of molecule alignment $\langle\langle \cos^2\theta \rangle\rangle$ after the pump pulse (Figure 5.5). This is the antisymmetric nature of HOMO orbitals in C_2H_2 since C_2H_2 has electron density around the bond axis other than molecular axis as seen in N_2 molecule. That explains observation of a reduced HHG signal when the molecular axis is parallel to electric field for C_2H_2, and observation of enhanced HHG signal when the molecular axis is parallel to electric field for N_2.

5.6 Conclusion

We studied the effects of electronic structure and symmetry in femtosecond laser driven photoelectron ionization yields for laser aligned conjugated linear molecules. HOMOs are the easiest place to donate electrons so we considered HOMO symmetry of the molecules. The molecule N_2 has maximum electron density along internuclear (molecular) axis due to σ_g HOMOs, so molecular ionization rate is maximum when molecules are aligned along laser polarization direction for the molecules, and it makes possible to eject electron easily. Therefore our measured HH intensity are observed to modulate in phase with time dependency of molecule alignment parameter after the pump laser pulse. Due to π_u HOMO symmetry of C_2H_2 which has electron density surrounding the bond axis with a node along the bonding axis, our experimental result for C_2H_2 show that the ionization

rate is in the reverse structure of C_2H_2 with respect to the time dependency of molecule alignment $\langle\langle \cos^2\theta \rangle\rangle$ after the pump pulse.

CHAPTER VI

GENERATION OF ENHANCED EVEN AND ODD HARMONICS IN TWO COLOR LASER FIELDS

6.1 Introduction

High harmonic generation (HHG) results from the interaction between driving intense laser field with atoms or molecules, and it can produce coherent radiation in the XUV spectral region. This light source possesses unique properties such as coherence and ultrashort pulse duration ranging from femtoseconds to attoseconds [19]. The HHG has been investigated for the development of attosecond physics [132], microscopic imaging [39-41, 133], interferometry [134], and also for the exploration of atomic and molecular structures [50, 53, 135].

However, HHG source has significant disadvantage of low conversion efficiency of the fundamental radiation into XUV radiation. Several approaches have been developed to improve this efficiency in order to make it a practical useful source of coherent radiation, i.e. mixed gas medium or two gas cells [91, 104], improvement of the phase matching between a driving laser pulse and generated harmonics [58, 136]. Another proposed approach to significantly enhance harmonic efficiency is by using synthesized laser field, a two-color laser field, formed of the fundamental (ω_0) laser field and its second harmonic (SH) [137, 138]. It efficiently generates even harmonics besides the odd harmonics due to breaking of the inversion symmetry [139].

HHG with two-color fields has been shown that application of HHG experiment with bichromotic field can be used for imaging atomic wave function [140] or the generation of shorter attosecond pulses [141, 142]. We present results on generation of high harmonic (HHs) with a two-color laser fields of fundamental (ω_0) and its second harmonic ($2\omega_0$) in argon (Ar), molecular nitrogen (N_2) and carbon dioxide (CO_2) gases having close ionization potentials. High harmonic spectra were measured for parallel and perpendicular relative polarizations of the fundamental and the second harmonic fields. With the combined (ω_0+$2\omega_0$) fields more than an order of magnitude enhancement of the HHs signal was observed compared to the ω_0 or $2\omega_0$ field alone. An increased conversion efficiency into HHs, notably of the even orders of 2(2m+1) (m=1-3) was found for the latter case. We also discuss similarities and differences of the HH generation in the three gas media with a single and two-color fields. HHG experiment with two color fields brings additional degrees of freedom to experimental parameters to control the HHG emission, such as relative polarization, intensities, phases and wavelengths.

6.2 Experimental Setup

The driving laser system consists of a 1kHz Ti:Sapphire chirped pulse amplification (CPA) system that delivered 1mJ pulse energy at 800nm wavelength (ω_0) in 50fs FWHM pulse duration. The laser intensity of the fundamental radiation (ω_0) at the focus in the single color case was 1.5×10^{14}W/cm^2. For the doubling the frequency of the IR laser pulse and generating additional beam at 400nm with ~15% conversion efficiency, we use a β-barium borate (BBO) crystal, (type I, 150μm thickness).

The BBO crystal is placed between the focusing lens (f=40cm) and the gas jet, so after this crystal the laser field consists of both the SH beam ($2\omega_0$) and the fundamental (ω_0) beam. The harmonic spectrum with a single-color field is obtained by removing the BBO crystal from the beam line. The generated SH beam is orthogonally polarized, and the polarization of the fundamental field is monitored by inserting a half wave ($\lambda/2$) plate after the BBO crystal as depicted in Figure 6.1. Thus, we are able to rotate the polarization of the fundamental laser field, while maintaining the polarization of SH field. This setup allows two color HHG experiment in parallel and orthogonal polarization conditions of the fundamental and SH fields. To obtain only second harmonic radiation we use a blue filter, which blocked 800nm radiation, but also reduce the output at 400nm to 65%. The polarization of the fundamental field is checked by inserting a polarizer and a power meter after the filter. To check the IR beam polarization, we use an infrared filter to block the blue beam, and polarization of IR beam is monitored with controlling the half wave plate, the polarizer and the power meter. The similar polarization check has been performed for the blue beam. By this way the polarization of the both fields are determined such that the polarization of the blue beam has always vertical polarization, and the polarization of the IR beam has horizontal polarization. After inserting the doubling crystal, the laser intensity of the residual fundamental field is in the range of ~7-9×10^{13}W/cm^2, and the intensity of second harmonic field is in the range of ~0.3-7×10^{13}W/cm^2. The gas pressure in the interaction region of the gas jet made with a 1mm thickness nickel (Ni) tube burned through by the laser pulses is estimated to be 50mbar. A constant gas flow is maintained

by the backing pressure of about ~2bar. More details of our setup and the optimization of its operation can be found elsewhere [58].

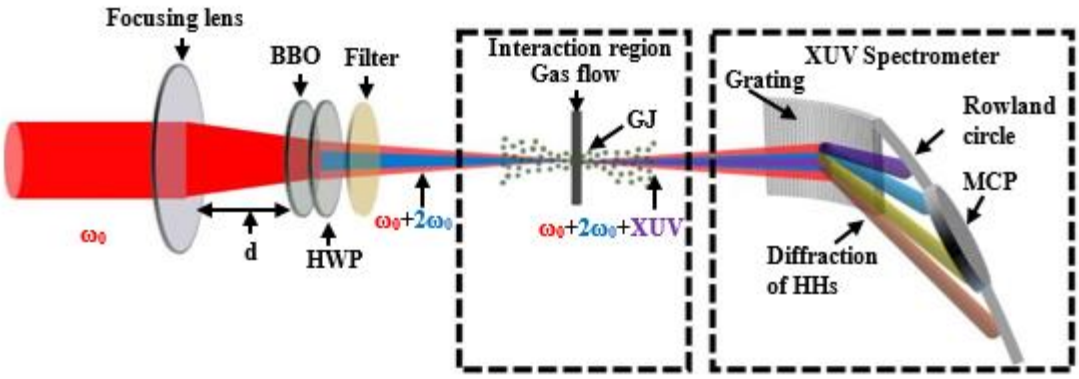

Figure 6.1 Experimental setup of harmonic generation in the two-color (ω_0+$2\omega_0$) case. d is distance between the focusing lens and the BBO doubling. BBO: Beta barium borate doubling crystal, HWP: Half-wave plate, GJ: Gas jet, HHs: High harmonic, MCP: Micro channel plate

The high harmonics (HHs) produced in a gas jet are detected with an XUV spectrometer (McPherson, 248/310G). In this spectrometer, XUV radiation is diffracted by a grating (133.6 groves/mm) to an imaging micro-channel plate (MCP). At one position of the MCP only a portion of the full spectrum could be acquired. When needed, the MCP is moved along the Rowland circle (where HHs are well focused) to capture the full set of generated HHs. The phosphorous screen mounted at the back side of the MCP produced an image of sequence of HHs projected onto a charge-coupled device (CCD camera), and the image from the CCD is processed for the spectrum analysis.

To compensate for the dispersion due to the doubling crystal, the lens and the entrance window of the interaction chamber, the chirp of the pulse is adjusted with the compressor to produce the highest HHs signal. Since the electron plasma density causes

defocusing of the propagating intense laser pulse, the target is placed at an optimum position to get maximum HHs output signal. Since the fundamental field is much stronger than that of its second harmonic field, the phase matching conditions are not changed significantly when the $2\omega_0$ field is added.

6.3 Experimental Results

The images of the HHs from the CCD camera obtained in N_2 gas are shown in Figure 6.2. All experiments are carried out at similar parameters, and the integration time for each measurement is adjusted to acquire the brightest harmonic signal just below the saturation of the CCD camera. Only ω_0 field having intensity of $I(\omega_0)=1.5\times10^{14}W/cm^2$ produces only odd harmonics, and the spectra is taken at 10sec integration time, Figure 6.2 (a). When the two color fields are used, not only odd harmonics but also even harmonic (14^{th}) is observed, and intensity of the ω_0 field is $I(\omega_0)=9\times10^{13}W/cm^2$ and of the $2\omega_0$ field is $I(2\omega_0)=3\times10^{13}W/cm^2$. Integration time of the CCD is adjusted to 5sec, Figure 6.2 (b). When only $2\omega_0$ field having intensity of $I(2\omega_0)=3\times10^{13}W/cm^2$ is used, the generation of 14^{th} order is produced, and the integration time of the CCD is set to 180sec integration time, Figure 6.2 (c)).

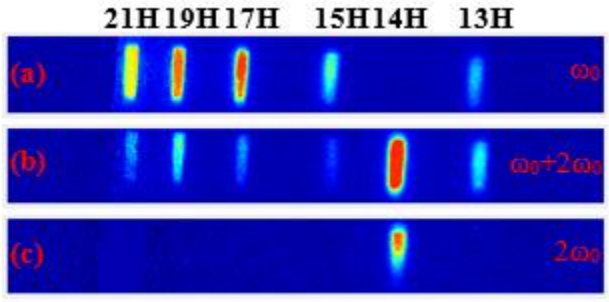

Figure 6.2 Harmonic spectra for N_2 gas from 13^{th} to 21^{st} odd orders and 14^{th} even order, in the case of (a) single-color fundamental field (800nm) with intensity of $I(\omega_0)=1.5\times10^{14}W/cm^2$ at 10sec integration time (b) two-color field (800nm+400nm) with intensity of $I(\omega_0)=9\times10^{13}W/cm^2$ and $I(2\omega_0)=3\times10^{13}W/cm^2$ at 5sec integration time (c) single-color (400nm) with intensity of $I(2\omega_0)=3\times10^{13}W/cm^2$ at 180sec integration time. For (a-c) the spectra were captured at one position of the MCP

In Figure 6.3 the complete observed spectra of HHs are shown from N_2 gas. The polarization of $2\omega_0$ field is vertical, and ω_0 field is horizontal. Besides odd harmonics from 5^{th} to 21^{st} orders, even harmonics of 6^{th}, 10^{th} and 14^{th} orders are also observed. The orders of these even harmonics satisfy the formula 2(2m+1) (m=1-3) showing that these are odd harmonics of the $2\omega_0$ field, which are also generated with only second harmonic field. The 14^{th} harmonic is dominating the spectrum, which can be related to a resonance excitation. In this case we observe suppression rather than enhancement of odd harmonics.

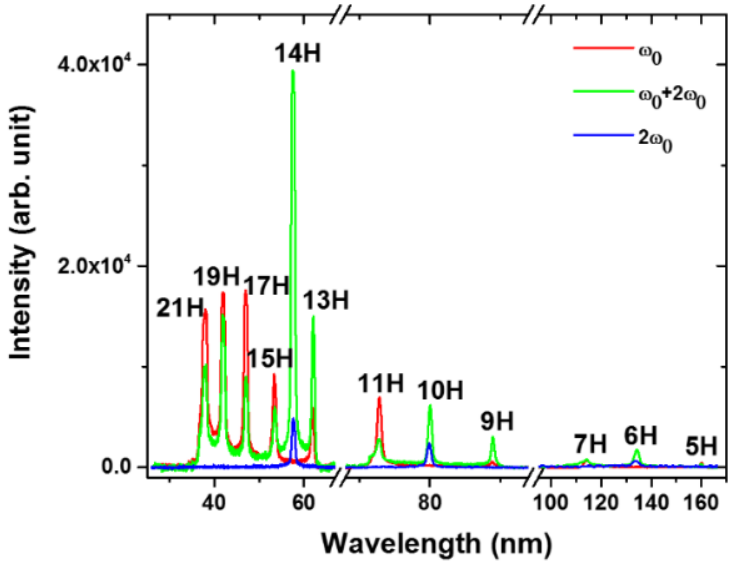

Figure 6.3 Nitrogen harmonic spectra of odd (from 5th to 21st) and even (6th, 10th and 14th) harmonics orders. Both fields are perpendicularly polarized. The intensity of ω_0 field with single-color case is $I(\omega_0)=1.5\times10^{14}W/cm^2$ (red line). With the two-color case, the intensity of ω_0 field is $I(\omega_0)=9\times10^{13}W/cm^2$, and the intensity of $2\omega_0$ field is $I(2\omega_0)=3\times10^{13}W/cm^2$ (green line). The intensity of $2\omega_0$ field with only $2\omega_0$ excitation is $I(2\omega_0)=3\times10^{13}W/cm^2$. (The values of blue line is magnified 18 times compared to red and green plots)

Harmonic spectra from Ar gas obtained using two-color excitation beams with parallel and orthogonal polarization (different polarization $\theta=0^o$, 45^o, 90^o) are shown in Figure 6.4; the doubling crystal is positioned at d=15cm after the focusing lens, and the $\lambda/2$ plate is placed after the crystal to change the polarization of the ω_0 beam. The BBO crystal is adjusted to generate even harmonic (14th order), in this case both fields are orthogonally polarized. The even harmonic is only observed when both fields has orthogonal polarization ($\theta=90^o$), and only odd harmonics are generated with the parallel polarization ($\theta=0^o$) of both fields. With the orthogonal polarization even harmonic is the dominating harmonic of the neighbor harmonics (for example 13th and 15th orders for the 14th harmonic). The even harmonic signal is decreased for the $\theta=45^o$ and disappears when

the $\theta=0^o$, but the amplitude of the neighbor harmonics of the 14^{th} order as well as other odd harmonics yields are increased when polarization of both fields are approaching the parallel polarization case.

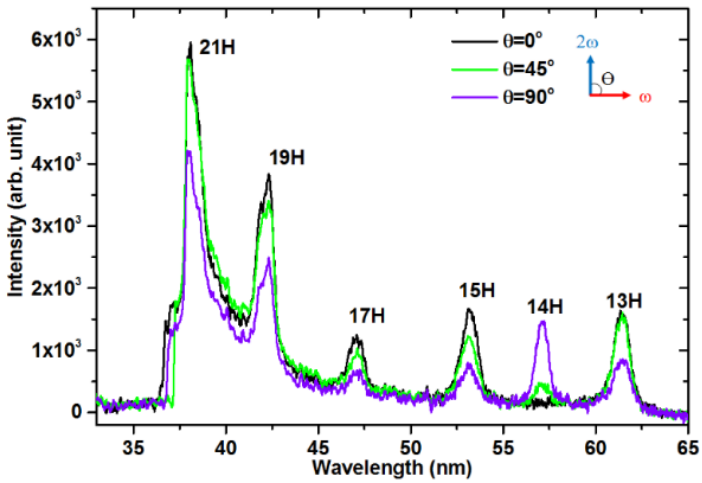

Figure 6.4 Harmonic spectra of Ar gas for two-color excitation beam with different polarizations (0^o, 45^o, 90^o) of ω_0 beam. Polarization of $2\omega_0$ field is always vertical, while the polarization of ω_0 field is horizontal ($\theta=90^o$, purple line), or $\theta=45^o$ (green line), or vertical ($\theta=0^o$, black line). The distance of the doubling crystal from the focusing lens is d=15cm. The intensity of the fundamental beam is $I(\omega_0)=1\times10^{14}W/cm^2$, and intensity of SH beam with parallel and perpendicular polarizations are $I(2\omega_0)=2.6\times10^{13}W/cm^2$; the integration times for both plots are 20sec

We have investigated the output of the HHs in Ar depending on the amount of fundamental radiation converted into the second harmonic for perpendicular (Figure 6.5) polarization of the ω_0 and $2\omega_0$ fields. The crystal is placed after the focusing lens at varying distance, namely at d=9cm, 12cm, 15cm from the focusing lens. The yield of the 14^{th} HH is increased with an increase of the rate of conversion into the second harmonic, while the output of the odd harmonics are decreased.

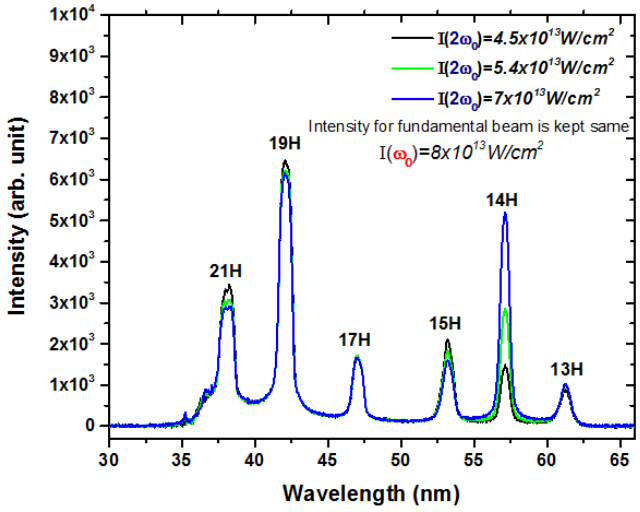

Figure 6.5 Harmonic spectra for Ar gas with the single-color and the two-color laser field. Distance between the SHC and the focusing lens is changed to get maximum conversion rate into SH field (i.e to get optimum 14th even order amplitude). Both fields are perpendicularly polarized. With the two-color case, the intensity of ω_0 field is $I(\omega_0)=8\times10^{13}W/cm^2$, and the intensities of the $2\omega_0$ fields are $I_{d=9}(2\omega_0)=4.5\times10^{13}W/cm^2$, $I_{d=12}(2\omega_0)=5.4\times10^{13}W/cm^2$, and $I_{d=15}(2\omega_0)=7\times10^{13}W/cm^2$. The integration time for all plots is 10sec

Figure 6.6 shows the effect of the IR beam on the even harmonics signal. The intensity of blue beam is kept same for both plots. The intensity of the red beam is changed, and it is $I(\omega_0)=9\times10^{13}W/cm^2$ for the black plot, and $I(\omega_0)=1.1\times10^{14}W/cm^2$ for the green plot. Contribution of the IR beam on the even harmonics is reasonable such that we observe the more even harmonic signal as well as the more odd harmonic signal from 5th to 21st odd orders with 6th, 10th and 14th even orders.

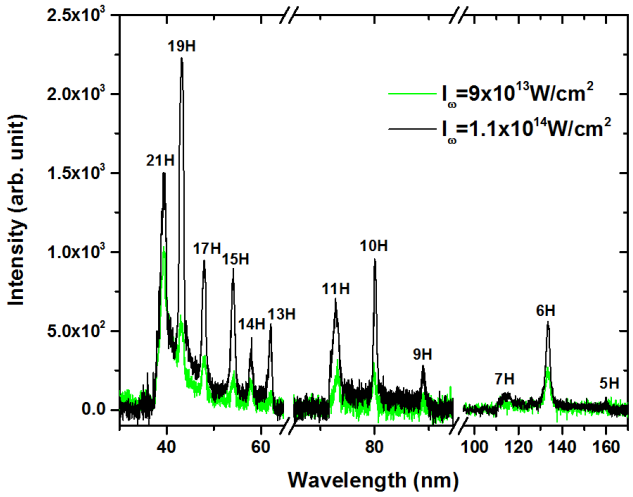

Figure 6.6 Argon harmonic spectra of odd (from 5th to 21st) and even (6th, 10th and 14th) harmonics orders. Both fields are perpendicularly polarized. The intensity of $2\omega_0$ field is kept same for both case ($I(2\omega_0)=1.7\times10^{13}W/cm^2$), and the intensity of the ω_0 field is changed, so the intensity of the black plot is $I(\omega_0)=9\times10^{13}W/cm^2$, and $I(\omega_0)=1.1\times10^{14}W/cm^2$

Figure 6.7 and Figure 6.8 show the complete measured spectra of HHs for Ar and CO_2 gases for perpendicular polarizations of the ω_0 and $2\omega_0$ fields. As in the case with N_2, harmonics of 2(2m+1) (m=1-3) orders were observed, however in Ar the 14th harmonic was not dominating, and in CO_2 10th harmonic was the strongest, followed in strength by 14th HH. Thus, the relative outputs of even harmonics depend on the gas species. Remarkably, the action of a two-color beam produces many times more intense output of even HHs compared to the action of the second harmonic alone. If either the fundamental beam or second harmonic beam alone is applied, the permitted orders are restricted to (2m+1)th or 2(2m+1)th, respectively, where m is an integer. The most interesting spectra of HHG with orthogonally polarized two color case is the generation of unusually strong signal at the 2(2m+1)th orders, i.e 14th order for N_2 and Ar, and 10th order for CO_2. These

harmonics corresponds to the odd harmonics of the SH field, showing strong influence of the SH field.

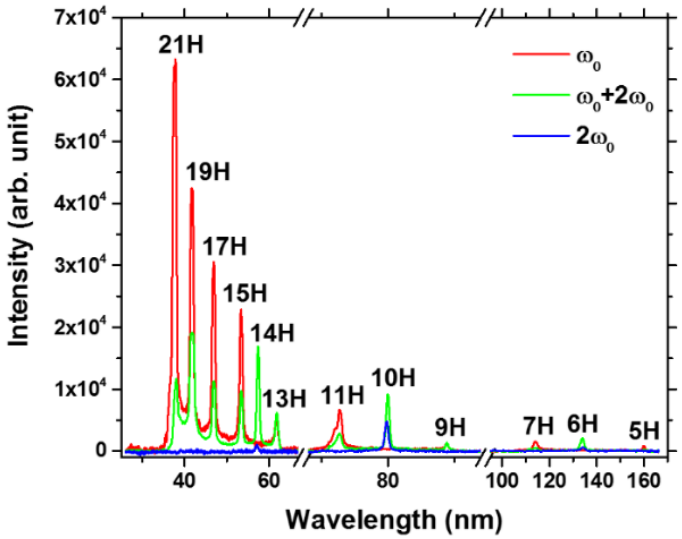

Figure 6.7 Argon harmonic spectra of odd (from 5th to 21st) and even (6th, 10th and 14th) harmonics orders. Both fields are perpendicularly polarized. The intensity of ω_0 field with single-color case is $I(\omega_0)=1.5\times10^{14}W/cm^2$ (red line). With the two-color case, the intensity of ω_0 field is $I(\omega_0)=9\times10^{13}W/cm^2$, and the intensity of $2\omega_0$ field is $I(2\omega_0)=3\times10^{13}W/cm^2$ (green line). The intensity of $2\omega_0$ field with only $2\omega_0$ excitation is $I(2\omega_0)=3\times10^{13}W/cm^2$ (blue line is magnified 18 times compared to red and green plots)

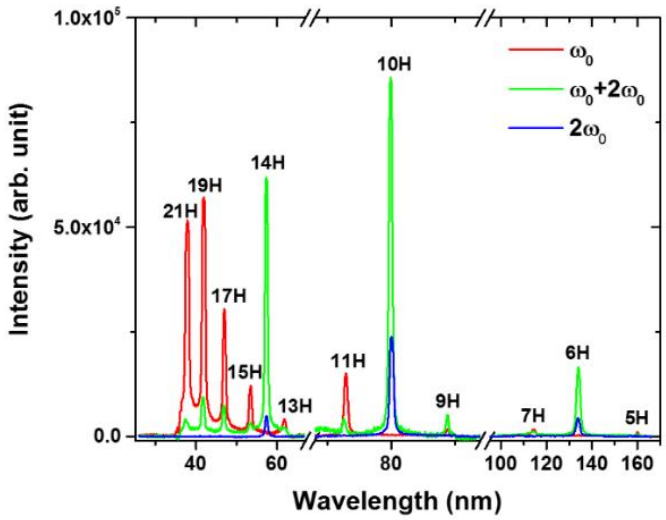

Figure 6.8 Carbon dioxide harmonic spectra of odd (from 5th to 21st) and even (6th, 10th and 14th) harmonics orders. Both fields are perpendicularly polarized. The intensity of ω_0 field with single-color case is $I(\omega_0)=1.5\times10^{14}W/cm^2$ (red line). With the two-color case, the intensity of ω_0 field is $I(\omega_0)=9\times10^{13}W/cm^2$, and the intensity of $2\omega_0$ field is $I(2\omega_0)=3\times10^{13}W/cm^2$ (green line). The intensity of $2\omega_0$ field with only $2\omega_0$ excitation is $I(2\omega_0)=3\times10^{13}W/cm^2$ (blue line is magnified 18 times compared to red and green plots)

6.4 Discussion

The optimization of the intensity of the two-color pulses was performed by optimizing the conversion efficiency of the fundamental field into the second harmonic field by rotating the BBO crystal to its optimum value before the $2\omega_0$ entered into the vacuum chamber. The strength of the $2\omega_0$ field has significant effect on the high harmonic signal. As we increased the intensity of the $2\omega_0$ beam, the even harmonic amplitudes could be increased as shown in Figure 6.5 for perpendicular polarizations of the ω_0 and $2\omega_0$ fields. The amplitude of the odd harmonics could be expected to be considerably stronger than that of the even harmonics because the intensity of the fundamental beam is significantly higher than that of the second harmonic beam. Indeed, when the second harmonic beam

acts alone, only very weak HHG is observed. However, for a two-color excitation even order harmonics become comparable and surprisingly can be even dominating in the spectrum. Even harmonics come from the $2\omega_0$ field, and the effect of the fundamental field (ω_0) in addition to $2\omega_0$ field is significant. The two-color excitation produced much stronger even harmonics (6^{th},10^{th}, and 14^{th}) than only $2\omega_0$ field, giving enhancement of the even harmonic by a factor of about 30-300 depending on the used gas and the even harmonic orders.

The estimate of the relative time delay at our experimental conditions shows that the ω_0 and the $2\omega_0$ beams are well separated in time so that the 800nm pulse comes first and the blue (400nm) pulse comes with about 500fs delay. It was estimated that both beam pass through a BK7 glass window (having x~6-7mm thickness) before they focused the gas jet, and the refractive index of BK7 glass for ω_0 and $2\omega_0$ fields are 1.5108 and 1.5308, respectively. The time delay is estimated for both beam with the formula of $\Delta t_{delay} = x/c\,(n_{2\omega} - n_{\omega})$ where c is the speed of light. The separation of the pulses is additionally confirmed by introducing with wedges additional layer of glass on the path of the beam after the doubling crystal, which introduce a delay between the red and blue pulses equal to many wavelength and nevertheless do not significantly affect the generated HHs output, and this confirmation is checked for parallel and perpendicular polarization of ω_0 and $2\omega_0$ fields, and the results are the same for both case. The relatively small delay, which is much shorter than the typical revival times in the investigated gases, also makes unlikely significant influence of the alignment of the gas molecules.

In view of a strong influence of the red beam on the generation of even harmonics, this means that the 800nm pulse should modify the gas medium making it more efficient for HHG with a 400nm pulse. The likely explanation is that the 800nm pulse produces excited states, which are easier to ionize with the subsequent 400nm pulse. Interesting effect is that the enhancement of the even harmonics strongly depends on the relative orientation of polarizations of the ω_0 and $2\omega_0$ fields. This means that the excitations induced by the red beam preserve their polarization orientation for times larger than the delay between the red and blue pulses (about 500fs).

According to the Ammosov-Delone-Krainov (ADK) formula [143], the tunneling ionization rate for the two color case is much larger than that for the one color field –the electron wave packet at the time of ionization is significantly denser. Thus orthogonally polarized two-color fields generate much stronger even harmonic than the second harmonic field alone.

High harmonic generation results from recombination of an electron to its ground state [55], and the single XUV photon is emitted through this dipolar transition. The maximum harmonic energy in the monochromatic field is theoretically given as I_P+U_P (α=3.17) where IP is the ionization potential of the atoms, and U_P is ponderomotive potential in electron volts and given

$$U_p = \frac{q^2 E_{\omega_0}^2}{4m\omega_0^2} = 9.33\times10^{-14} I[\mathrm{Wcm^{-2}}]\lambda^2[\mu\mathrm{m}] \qquad (6.1)$$

The Eq. (6.1) corresponds to the cutoff of the square of atomic dipole moments. However, the observed spectrum results from the phase matching term in addition to the single atom response, and the experimental value of the α is less than the theoretically determined one. The small value of α comes from the difference in the phase matching length between the beam and the gas medium, and the imperfect optical condition due to the divergence of the laser beam. The maximum value of the U_p for the long pulses is limited by the intensity determined with dc tunneling theory, but atoms can survive under higher laser intensities under the ultrashort pulses [144, 145]. Then the electron is exposed to strong increasing laser field before reencountering its parent ion, resulting in the generation of intense and high energy harmonics radiation. With all three gases: molecular nitrogen, argon and carbon dioxide gases, we observed generation of even harmonics of 2(2m+1)th (m=1-3) orders. The ionization potentials of the investigated gases are quite close: I_p=15.6eV for Ar [79], I_p=15.7eV for N_2 [146], and I_p=13.77eV for CO_2 [147]. Following the three step model that predicts the cutoff as $E_{cutoff}=I_P+3.17U_P$, we can estimate that the cutoff of the HH spectrum for only the $2\omega_0$ field should be at $13.7h\omega_0$~21.3eV for Ar and N_2 and at $12.6h\omega_0$~19.5eV for CO_2, which is in good agreement with the cutoffs for the even harmonics, and it shows that the 14th HH from CO_2 is already above the cutoff and therefore should be suppressed as is observed in the experiment (Figure 6.8). For the initial fundamental (red) beam we obtain the cutoff values $28.4h\omega_0$~44eV for Ar and N_2 and at $27.2h\omega_0$~42.2eV for CO_2, which is beyond the shortest wavelength measured in the experiment (21st HH).

Strong harmonic generation is possible due to the selection of the short quantum path component, which has denser electron wave packet, and high ionization rate [145]. In the two-color case, the longer integration time of the electron to the laser field leads to more divergent harmonics, and the long trajectory contribution is smaller to the HH yield. Due to having relative phase between the fundamental and second harmonic fields, the two-color case enhances the short path contribution while diminishing other electrons paths, resulting in a clean high harmonic spectrum [137]. The ionization probability in the two-color laser field is higher than the case in the fundamental field, leading the enhanced HHG. Also vibration of electron is quicker, and its amplitude is bigger in the two-color laser fields than the case in the fundamental field. With the quicker vibration, the electron leaves and returns to ion core quickly, providing that the electron most likely returns and recombines with ion core, radiating high energy photons. So the more probability of the electron is, the higher conversion efficiency of HHG is [148]. These possibilities can contribute to the generation of even harmonics with the two-color case compared to the only $2\omega_0$ field [143], and that may explain the addition of the ω_0 field to $2\omega_0$ field increase the even harmonic amplitude as seen in Figure 6.3, Figure 6.7, and Figure 6.8.

There are two electron trajectories under the monochromatic field, long and short trajectories of the returning electron. The long trajectory of the electron is neglected because of the spread of the electron wave function, and also the electron is exposed the intensity variation longer time so the electron most likely miss the its core. The harmonic generation mostly comes from short trajectory, and electron ionized in this region (short

trajectory) is the main contributor to efficient harmonic generation because the harmonic phase is insensitive to variation of the laser field [143].

6.5 Conclusion and Outlook

We observe efficient high order harmonic generation with two-color fields of parallel or orthogonal mutual orientations of polarizations of both fields. The enhancement of HHs yield with the two-color field is by more than one order of magnitude compared to the ω_0 field alone. We also look at even harmonic generation with the two-color case of horizontal polarization of ω_0 and vertical polarization of $2\omega_0$ field. We find that the intensities of even order harmonics are comparable to odd harmonics. Moreover, the even order harmonics are generated with significant intensities that cannot be generated with only $2\omega_0$ field. In addition, the generation of even harmonics of the fundamental field, which corresponded to the odd harmonics of the second harmonic field with orders (2(2m+1), (m=1-3))) are observed. The output of the latter is increased up to 300 times with addition of the ω_0 field to the $2\omega_0$ field.

The application of a two-color driven field for the HHG in gases can reveal some new features related with the ionic transitions of the gas medium and specific relations between the phases of two waves. A very intense 14^{th} harmonic, alongside the strong 13^{th} or 15^{th} harmonic, appears in the plateau region, and it can be that the enhancement of this harmonic is caused by the closeness with the same ionic transition, which induces the strong 13^{th} or 15^{th} harmonic generation.

We repeat the experiment with three different gases, and it is highly probable that the properties of the harmonics are governed by the propagation of the free electron in the continuum subject to driving fields rather than the structure of the used gas mediums. Moreover, the small deviations from perfect perpendicular or parallel polarization may alter the harmonic spectrum, and the variation of the frequencies of both fields' phase affect the intensity ratio of harmonics [149]. These effects give possible interpretation of the experimentally observed harmonics spectra for our experimental configuration.

In two-color field the output of harmonics depends on the mutual orientation of polarizations. With two parallel polarized fields much stronger odd harmonics are generated compared to the perpendicularly polarized two fields, since the possibility of the returning electron into ionized position is high with the same polarized fields, leading to a more efficient harmonic generation. The harmonics produced with perpendicularly polarized fields provide a combination of even-odd harmonics of the fundamental beam, and strong even harmonics are observed with perpendicular polarized field. This technique is promising way to further enhance harmonic yields, especially for the even harmonic orders in the XUV range.

By adjusting the relative intensities and polarizations of the ω_0 and $2\omega_0$ fields, one can control the even/odd harmonics and their relative signal without changing the parameters of the fundamental driving laser. These experimental observations prove that an enhancement of the conversion efficiency of HHs and generation of isolated odd/even harmonics can be obtained with the two-color laser field in a simple setup, and it is a useful source for practical applications ranging from engineering to scientific studies- as it can

act as a broad range XUV beam splitter that can be implemented for XUV pump-XUV probe experiment.

CHAPTER VII

STUDIES OF IMAGING OF A MESH WITH DIFFERENT HARMONIC ORDERS

7.1 Introduction

The coherent diffraction imaging (CDI) technique has potential to capture high resolution images of nano-micron sized structures. When the sample is exposed by HHG source, a diffraction pattern of the object is created. Then, the object image can be reconstructed by using an algorithm to retrieve the structure of the sample. Recently, JILA group at University of Colorado performed an imaging experiment [150], where four narrow harmonics with ~30nm wavelengths were simultaneously used as the illumination source to image the sample, and an algorithm was employed to reconstruct images for each harmonic order. The CDI experimental application by using HHG source is promising for imaging of nano-micron objects with a table-top femtosecond laser system.

There are different techniques for the imaging at the microscopic and the nanoscopic scale, namely optical, electron, X-ray microscopies, which have broad applications. But, they have also some drawbacks. For example, optical microcopy is limited by a diffraction limited spot of the optical wavelength (~$\lambda/2$) [151]. Electron microscopy is limited by the fact that the interaction of an electron with matter results in its short mean free path, since the electron is a charged, strongly interacting particle. The X-ray microscopy provides high resolution imaging of thick samples, but it is limited in broader applications due to fabrication complexity of the X-ray optics.

Recent progress in the imaging techniques with HHG approach makes the soft X-ray microscopy more applicable for broader use. The diffractive imaging technique from coherent table top X-ray beams have made possible nanometer-scale resolution imaging by replacing the imaging optics with a computer reconstruction algorithm [152, 153], and advances in the coherent HHG make it possible to use tabletop sources with enough photon flux for soft X-ray imaging [154, 155].

In CDI with tabletop soft X-ray sources further progress can be expected, since with HHG fully coherent beams with sufficient photon flux for diffractive microscopy can be produced, and the generated wavelength can be 13nm and shorter, where the nonlinear photon energy up-conversion efficiency can be improved by phase matching [155]. Although, the photon flux with HHG reduces at higher photon energies, i.e in the "water window" spectral region, which is important for biological studies [144, 156], it can be enhanced several orders of magnitude with the application of phase matching technique [136, 157].

In this study, we present our initial work to diffractive imaging using a tabletop X-ray source. The initial investigation of the application of a HHG source with a micron sized object is performed by using an optimized HHG source.

7.2 Experimental Setup

In our experiments, we used the amplified femtosecond radiation from a Ti:sapphire chirped-pulse amplification system (Spectra Physics, Spitfire). Our system produces ~50fs laser pulses at a repetition rate of 1kHz. The central wavelength is 800nm, and the energy per pulse is ~1mJ. The output radiation is focused on the gas jet filled with Ar. Following

the gas jet, the generated HHs propagate through the McPherson spectrometer. We placed a square mesh, having period of ~135µm (Figure 7.2), in the path of the HH radiation at three different positions from the spectrometer (40cm, 96cm, and 148cm), Figure 7.1. For each imaging experimental run, we insert only one mesh into the path of the radiation at the positions 1, 2 and 3 in Figure 7.1.

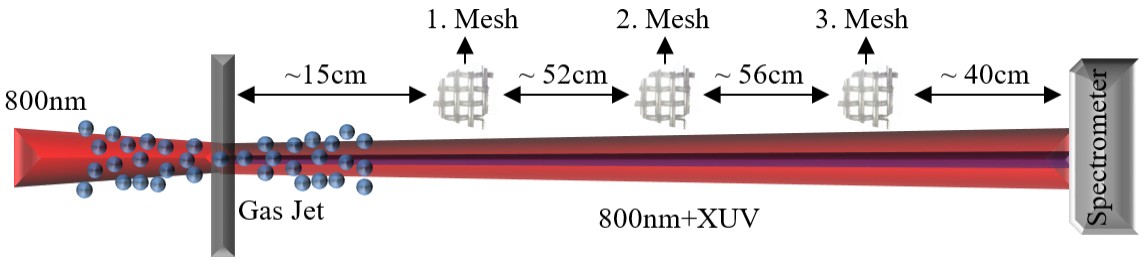

Figure 7.1 Schematic of the imaging experiment setup

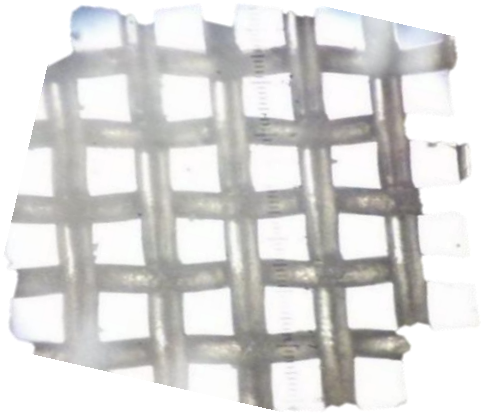

Figure 7.2 Mesh image under view of the microscope; the period of the mesh is ~135µm

7.3 Experimental Results

We performed the experiment at different conditions. Initially, the mesh sample is removed from the path of the HHs radiation to take the reference harmonic spectrum. Figure 7.3 shows the typical harmonic spectrum from 13^{th} to 21^{st} orders when the mesh is removed.

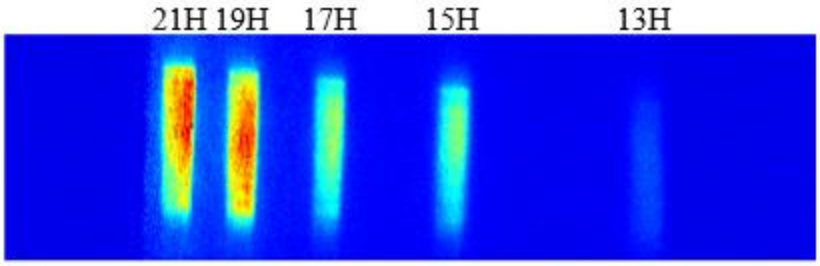

Figure 7.3 Harmonic spectrum with no mesh in the path of HHs

When the mesh is placed far (148cm) from the spectrometer, the far field conditions are satisfied, and the separations of the intensity peaks within each HH are increased. We observed the image features spreading in the horizontal and vertical directions for each harmonic order, as seen in Figure 7.4.

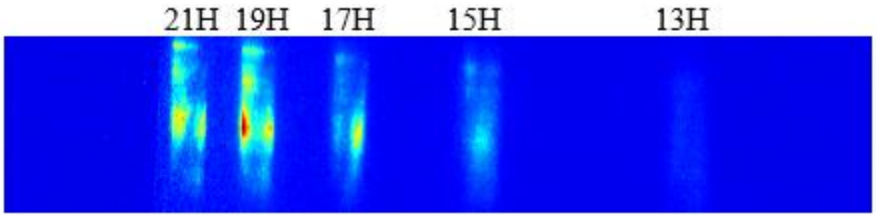

Figure 7.4 Harmonic spectrum with mesh placed at a distance of 148cm from the spectrometer

Placing the mesh position closer to the spectrometer allows to see more intensity maxima and minima in the visible portion of the diffraction pattern. For the mesh placed 96cm from the spectrometer, the image is shown in Figure 7.5.

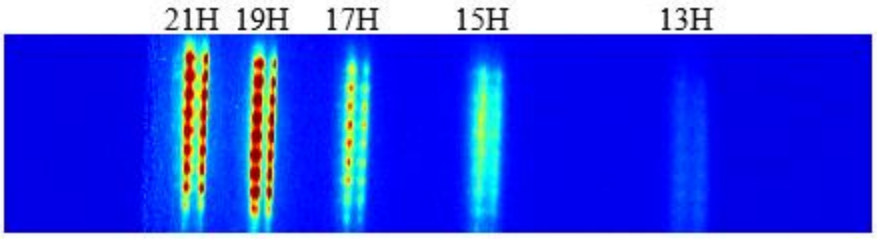

Figure 7.5 Harmonic spectrum with mesh placed at a distance of 96cm from the spectrometer

When the mesh is placed closer to the spectrometer at about 40cm, which corresponds to be reduced diffraction divergence, even more intensity maxima and minima in the horizontal and vertical direction are observed, as seen in Figure 7.6.

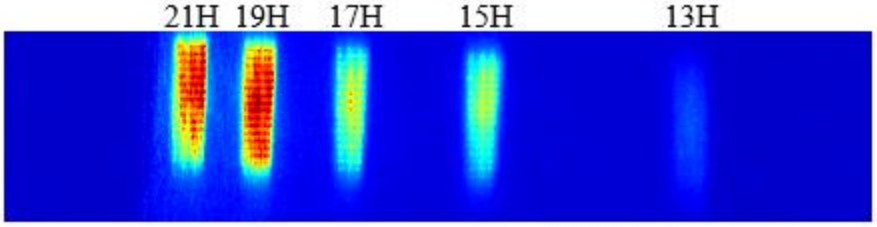

Figure 7.6 Harmonic spectrum with mesh placed at a distance of 40cm from the spectrometer

7.4 Discussion

Since the best image was obtained for the second mesh position, we analyzed the second mesh image (Figure 7.5) and estimated the period of the mesh in vertical direction by using the diffraction formula. Since the size of the MCP is 40mm, which corresponds to

~960pixels on the captured image of the MCP by the CCD camera, the separation of the peaks can be calculated. We examined the diffraction pattern for harmonics orders of 17th, 19th, and 21st of the Figure 7.5.

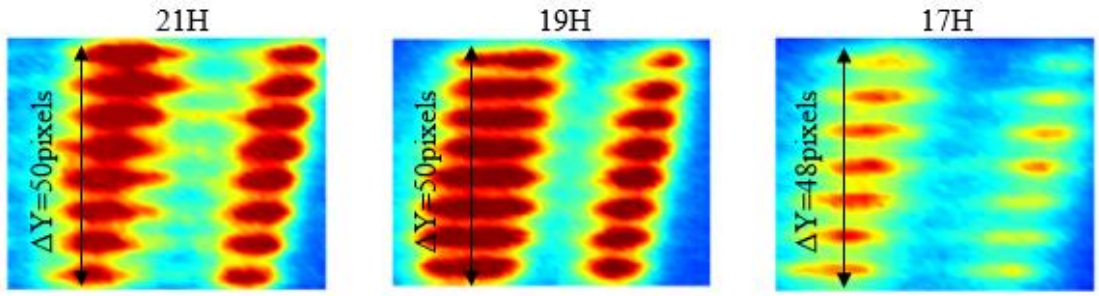

Figure 7.7 Zoomed harmonic spectrum of Figure 7.5

There are seven separations of the peaks in vertical direction for the 19th and 21st harmonics, and six separations for the 17th harmonic order. The mean separation of the peaks ΔY is estimated in terms of pixels (from raw data), in Figure 7.7. By considering the size of the MCP in mm (40mm) and the size of the MCP in pixels captured by the CCD camera (~960 pixels), the separation of peaks in mm can be evaluated for each separation: $\Delta y = \Delta Y/7 = 0.29$mm for the 19th and 21st orders, and $\Delta y = \Delta Y/6 = 0.33$mm for the 17th order. Then, θ is estimated for each Δy separation, $\Delta y_1 = y_1 - y_0$, $\tan(\theta) = \Delta y_1 / l$, and $\theta = \tan^{-1}(\Delta y_1 / l)$. Thus, the d value that is the period of the mesh is found from the experimental value for Δy, the separation between the intensity maxima, (see Figure 7.8). By using the formula $m\lambda = d\sin(\theta), m=1$, the d value is found 131μm for the 17th and the 19th harmonic, and 141 μm for the 21st harmonic. These values are close to the value of the mesh period measured with the microscope.

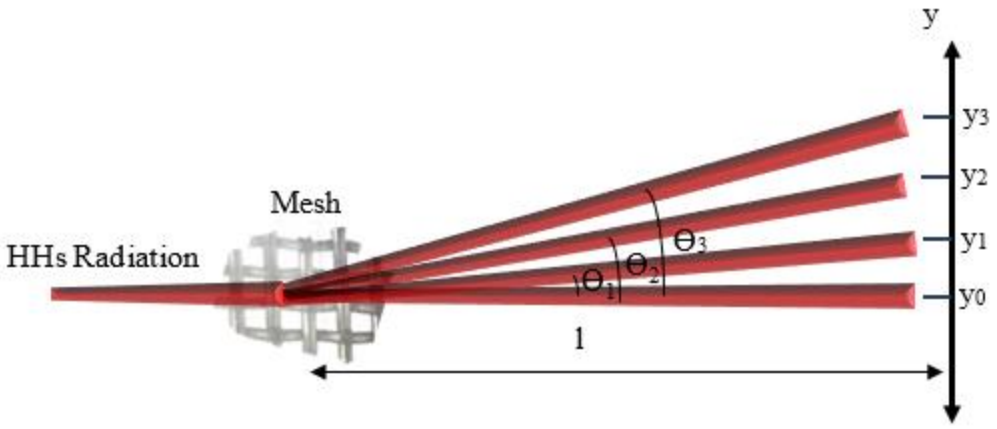

Figure 7.8 Estimation the period of the mesh from experimental result

7.5 Conclusion

The field of the lens-less imaging has been improving over the years. The imaging technique can be applied to many important research fields achieving with XUV and soft-X-ray radiation very high spatial resolution. In this study, we presented a simple application of the HHs radiation to a small size object. Though not as informative as the coherent diffractive imaging, diffraction fringes from the micron-sized mesh produced by HHs radiation and captured by the spectrometer's CCD allowed to estimate the period of the mesh from measurements with harmonics of different orders that gives the additional advantage of cross-checking of the obtained results.

CHAPTER VIII

OVERALL CONCLUSIONS

In this dissertation, spectra of HHs in the XUV region were observed with a table-top laser system at the 800nm excitation wavelength, 50fs pulse duration. The dissertation consists of five different experiments, namely pressure optimization of HHs in a differentially pumped gas cell, gas mixture of H_2 and Ne gas, HHs emission from molecular alignment, HHs with two color fields, and finally an application of the HHs radiation on the micron-sized mesh.

In the pressure optimization study, the optimal conditions and phase matching issues are experimentally investigated and theoretically discussed. In the study of HHG in a gas mixture, the dependence of the HH yield on the mixture composition was investigated. This yield from a pure Ne gas is low due to high ionization potential of Ne. However, in gas mixtures of H_2 and Ne, an enhancement of the HH flux was observed compared to pure gases were studied, and the developed theoretical description with performed simulations showed agreement with the experimental results. Another mechanism of HHG enhancements by using aligned molecules was demonstrated by using pump-probe technique. About twofold increase of the harmonic amplitude output was observed. N_2 and C_2H_2 gases were studied to observe the HH signal at aligned, anti-aligned, non-aligned conditions. The two-color study have shown the possibility to generate enhanced even or odd harmonics. Moreover, the polarization dependence of the two-color HHs was investigated. Finally, after optimizing the HHs radiation

and improving the efficiency of the HHs source, we have studied an application of the HH radiation on the mesh sample. The micron-sized object is used, the coherent HHs radiation is shined on the mesh, and the diffraction pattern is obtained for different harmonic orders and different mesh positions relative to the XUV spectrometer. The period of the mesh is retrieved from the experimental results by using the diffraction formula, and it is in close agreement with the value of the mesh period measured with a microscope.

The further enhancement and optimization of HH radiation may lead to more advanced imaging applications of the HHs source, i.e. for biological imaging. In addition, the generation of more energetic HHs pulses may also become useful for XUV pump and XUV probe for gas characterization experiments.

REFERENCES

[1] Microchannel Plates (MCP), www.dmphotonics.com/. Accessed 06/20/2016.

[2] M. Sayrac, Physics and Astronomy, Texas A&M University, Texas A&M University, (2013).

[3] K.C. Kulander, F.H. Mies, K.J. Schafer, Phys. Rev. A 53 (1996) 2562.

[4] J. McKenna, A.M. Sayler, F. Anis, B. Gaire, N.G. Johnson, et al., Phys. Rev. Lett. 100 (2008) 133001.

[5] P.M. Paul, E.S. Toma, P. Breger, G. Mullot, F. Augé, et al., Science 292 (2001) 1689.

[6] J.T. Lin, T.F. Jiang, Phys. Rev. A 63 (2000) 013408.

[7] J. Ludwig, H. Rottke, W. Sandner, Phys. Rev. A 56 (1997) 2168

[8] A.D. Bandrauk, H.Z. Lu, Phys. Rev. A 73 (2006) 013412.

[9] A. Rudenko, B. Feuerstein, K. Zrost, V.L.B.d. Jesus, T. Ergler, et al., J. Phys. B: At. Mol. Opt. Phys. 38 (2005) 487.

[10] M.Y. Shverdin, D.R. Walker, D.D. Yavuz, G.Y. Yin, S.E. Harris, Phys. Rev. Lett 94 (2005) 033904.

[11] A. Gürtler, F. Robicheaux, W.J.V.D. Zande, L.D. Noordam, Phys. Rev. Lett. 92 (2004) 033002.

[12] G.G. Paulus, F. Grasbon, H. Walther, P. Villoresi, M. Nisoli, et al., Nature 414 (2001) 182-184.

[13] V. Roudnev, B.D. Esry, Phys. Rev. Lett. 99 (2007) 220406

[14] M.F. Kling, C. Siedschlag, A.J. Verhoef, J.I. Khan, M. Schultze, et al., Science 312 (2006) 246.

[15] T. Rathje, A.M. Sayler, S. Zeng, P. Wustelt, H. Figger, et al., phy. Rev. Lett. 111 (2013) 093002.

[16] T. Brabec, F. Krausz, Rev. Mod. Phys. 72 (2000) 545.

[17] A. Azarm, S. Ramakrishna, A. Talebpour, S. Hosseini, Y. Teranishi, et al., J. Phys. B: At. Mol. Opt. Phys. 43 (2010) 235602.

[18] X. Xie, K. Doblhoff-Dier, H. Xu, S. Roither, M.S. Schöffler, et al., Phy. Rev. Lett. 112 (2014) 163003.

[19] F. Krausz, M. Ivanov, Rev. Mod. Phys. 81 (2009) 163.

[20] A.H. Zewail, J. Phys. Chem. A 104 (2000) 5660.

[21] R.J. Glauber, Rev. Mod. Phys. 78 (2006) 1267.

[22] J.L. Hall, Rev. Mod. Phys. 78 (2005) 1279.

[23] T.W. Hansch, Rev. Mod. Phys. 78 (2005) 1297.

[24] S.A. Diddams, D.J. Jones, J. Ye, S.T. Cundiff, J.L. Hall, et al., Phy. Rev. Lett. 84 (2000) 5102.

[25] T. Udem, R. Holzwarth, T.W. Hansch, Nature 416 (2002) 233.

[26] T. Popmintchev, M.-C. Chen, D. Popmintchev, P. Arpin, S. Brown, et al., Science 336 (2012) 1287.

[27] C. Hernández-García, J.A. Pérez-Hernández, T. Popmintchev, M.M. Murnane, H.C. Kapteyn, et al., Phy. Rev. Lett. 111 (2013) 033002.

[28] S.L. Voronov, I. Kohl, J.B. Madsen, J. Simmons, N. Terry, et al., Phy. Rev. Lett. 87 (2001) 133902.

[29] A. L'huillier, T. Auguste, P. Balcou, B. Carré, P. Monot, et al., J. Nonlinear Opt. Phys. Mater. 04 (1995) 647.

[30] E. Constant, D. Garzella, P. Breger, E. Mével, C. Dorrer, et al., Physical Review Letters 82 (1999) 1668.

[31] A. L'Huillier, X.F. Li, L.A. Lompré, JOSA B 7 (1990) 527.

[32] K.H. Hong, C.J. Lai, J.P. Siqueira, P. Krogen, J. Moses, et al., Opt. Lett. 39 (2014) 3145.

[33] O.H. Heckl, C.R.E. Baer, C. Kränkel, S.V. Marchese, F. Schapper, et al., Appl. Phys. B 97 (2009) 369.

[34] C. Jin, G. Wang, H. Wei, A. T. Le, C.D. Lin, Nat. Commun. 5 (2014) 1.

[35] W. Li, A.A. Jaroń-Becker, C.W. Hogle, V. Sharma, X. Zhou, et al., PNAS 107 (2010) 20219.

[36] L. Miaja Avila, G. Saathoff, S. Mathias, J. Yin, C. La-o-vorakiat, et al., Phy. Rev. Lett. 101 (2008) 046101.

[37] M. Bauer, C. Lei, K. Read, R. Tobey, J. Gland, et al., Phy. Rev. Lett. 87 (2001) 025501.

[38] R. Haight, Surf. Sci. Rep. 21 (1995) 275.

[39] M.D. Seaberg, D.E. Adams, E.L. Townsend, D.A. Raymondson, W.F. Schlotter, et al., Opt. Express 19 (2011) 22470.

[40] A. Ravasio, D. Gauthier, F.R.N.C. Maia, M. Billon, J.P. Caumes, et al., Phys. Rev. Lett. 103 (2009) 028104.

[41] F. Brizuela, I.D. Howlett, S. Carbajo, D. Peterson, A. Sakdinawat, et al., IEEE J. Sel. Top. Quantum Electron 18 (2012) 434.

[42] J. Larsson, E. Mevel, R. Zerne, A. L'Huillier, C.-G. Wahlstrom, et al., J. Phys. B: At., Mol. Opt. Phys. 28 (1995) L53.

[43] C. Vozzi, F. Calegari, E. Benedetti, J.P. Caumes, G. Sansone, et al., Phys. Rev. Lett. 95 (2005) 153902.

[44] T. Kanai, S. Minemoto, H. Sakai, Nature 435 (2005) 470.

[45] P. Salières, A. L'Huillier, M. Lewenstein, Phy. Rev. Lett. 74 (1995) 3776.

[46] M.B. Gaarde, F. Salin, E. Constant, P. Balcou, K.J. Schafer, et al., Phy. Rev. A 59 (1999) 1367.

[47] A. Rundquist, C.G. Durfee, Z. Chang, C. Herne, S. Backus, et al., Science 280 (1998) 1412.

[48] E.A. Gibson, A. Paul, N. Wagner, R.a. Tobey, D. Gaudiosi, et al., Science 302 (2003) 95.

[49] S.E. Harris, J.J. Macklin, T.W. Hänsch, Optics Communications 100 (1993) 487.

[50] R. Kienberger, E. Goulielmakis, M. Uiberacker, A. Baltuska, V. Yakovlev, et al., Nature 427 (2004) 817.

[51] E. Goulielmakis, M. Uiberacker, R. Kienberger, A. Baltuska, V. Yakovlev, et al., Science 305 (2004) 1267.

[52] A. Pierre, F.D. Louis, Rep. Prog. Phys. 67 (2004) 813.

[53] M. Drescher, M. Hentschel, R. Kienberger, M. Uiberacker, V. Yakovlev, et al., Nature 419 (2002) 803.

[54] M. Murakami, Department of Physics and Astronomy, Louisiana State University, Louisiana State University, (2006) 103.

[55] P.B. Corkum, Phy. Rev. Lett. 71 (1993) 1994.

[56] K.J.S. J. L. Krause, K. C. Kulander, Phy. Rev. Lett. 68 (1992) 3535

[57] M. Lewenstein, P. Balcou, M.Y. Ivanov, A. L'Huillier, P.B. Corkum, Phys. Rev. A 49 (1994) 2117.

[58] M. Sayrac, A.A. Kolomenskii, S. Anumula, Y. Boran, N.A. Hart, et al., Rev. Sci. Instrum. 86 (2015) 043108.

[59] P. Salières, B. Carré, L. Le Déroff, F. Grasbon, G.G. Paulus, et al., Science 292 (2001) 902.

[60] F. Schapper, M. Holler, T. Auguste, A. Zaïr, M. Weger, et al., Opt. Express 18 (2010) 2987.

[61] P. Balcou, A.S. Dederichs, M.B. Gaarde, A. L'Huillier, J. Phys. B: At., Mol. Opt. Phys. 32 (1999) 2973.

[62] M.P. Poudel, Department of Physics and Astronomy, Texas A&M University, Texas A&M University Library, (2009).

[63] G. Scoles, Atomic and molecular beam methods:volume 1, Oxford University Press (1988)

[64] SXR and EUV Rowland Circle Monochromator, www.mcphersoninc.com/. Accessed 10/17/2016.

[65] Grating Information, www.ridl.cfd.rit.edu/. Accessed 10/19/2016.

[66] P. Balcou, C. Cornaggia, A.S.L. Gomes, L.A. Lompre, A. L'Huillier, J. Phys. B: At., Mol. Opt. Phys. 25 (1992) 4467.

[67] A. L'Huillier, P. Balcou, Phy. Rev. Lett. 70 (1993) 774.

[68] C.G. Wahlström, J. Larsson, A. Persson, T. Starczewski, S. Svanberg, et al., Phys. Rev. A 48 (1993) 4709.

[69] S.C. Rae, Opt. Commun. 97 (1993) 25.

[70] M.S. Kim, T. Scharf, A.d.C. Assafrao, C. Rockstuhl, S.F. Pereira, et al., Opt. Express 20 (2012) 28929.

[71] L.A. Lompré, A. L'Huillier, M. Ferray, P. Monot, G. Mainfray, et al., J. Opt. Soc. Am. B 7 (1990) 754.

[72] E. Constant, D. Garzella, P. Breger, E. Mével, C. Dorrer, et al., Phys. Rev. Lett. 82 (1999) 1668.

[73] C. Altucci, T. Starczewski, E. Mevel, C.G. Wahlström, B. Carré, et al., J. Opt. Soc. Am. B 13 (1996) 148.

[74] S. Rae, K. Burnett, J. Cooper, Phys. Rev. A 50 (1994) 3438.

[75] J.F. Hergott, M. Kovacev, H. Merdji, C. Hubert, Y. Mairesse, et al., Phys. Rev. A 66 (2002) 021801.

[76] E. Takahashi, Y. Nabekawa, T. Otsuka, M. Obara, K. Midorikawa, Phys. Rev. A 66 (2002) 021802.

[77] P. Rudawski, C.M. Heyl, F. Brizuela, J. Schwenke, A. Persson, et al., Rev. Sci. Instrum. 84 (2013) 073103.

[78] A. Hage, B. Landgraf, M. Taylor, M. Wünsche, T. Gangolf, et al., Rev. Sci. Instrum. 85 (2014) 103105.

[79] R. Womer, Phys. Rev. 38 (1931) 454.

[80] W. Bleakney, Phys. Rev. Lett. 40 (1932) 496.

[81] T. Popmintchev, M.-C. Chen, A. Bahabad, M. Gerrity, P. Sidorenko, et al., Proc. Nat. Acad. Sci. 106 (2009) 10516.

[82] K.B. Dinh, H.V. Le, P. Hannaford, L.V. Dao, J. Phys. Chem. Biophys. 4 (2013) 1.

[83] E. Gibson, A. Paul, N. Wagner, R.a. Tobey, S. Backus, et al., Phys. Rev. Lett. 92 (2004) 033001.

[84] R.W. Boyd, J. Opt. Soc. Am. 70 (1980) 877.

[85] G. Guzzinati, P. Schattschneider, K. Bliokh, F. Nori, J. Verbeeck, Phys. Rev. Lett. 110 (2013) 093601.

[86] B.L. Henke, E.M. Gullikson, J.C. Davis, Atom. Data Nucl. Data 54 (1993) 181.

[87] S. Kazamias, S. Daboussi, O. Guilbaud, K. Cassou, D. Ros, et al., Phy. Rev. A 83 (2011) 063405.

[88] R. Jan, K. Manuel, H. Steffen, D. Stefan, L. Jens, et al., New J. Phys. 16 (2014) 1-15.

[89] K. Ishikawa, Phys. Rev. Lett. 91 (2003) 043002.

[90] E.J. Takahashi, T. Kanai, K.L. Ishikawa, Y. Nabekawa, K. Midorikawa, Phy. Rev. Lett. 99 (2007) 053904.

[91] F. Brizuela, C.M. Heyl, P. Rudawski, D. Kroon, L. Rading, et al., Sci. Rep. 3 (2013) 1410.

[92] T. Kanai, E.J. Takahashi, Y. Nabekawa, K. Midorikawa, Phy. Rev. Lett. 98 (2007) 153904.

[93] Y. Liang, S. Augst, Y. Beaudoin, M. Chaker, H. Yu, et al., J. Phys. B: At Mol. Opt. Phys. 28 (1995) 3661.

[94] G. Cirmi, C.J. Lai, E. Granados, S.W. Huang, A. Sell, et al., J. Phys. B: At Mol. Opt. Phys. 45 (2012) 205601.

[95] J. Sutherland, E. Christensen, N. Powers, S. Rhynard, J. Painter, et al., Opt. Express 12 (2004) 4430.

[96] K. Mishima, K. Nagaya, M. Hayashi, S.H. Lin, Phys. Rev. A 70 (2004) 063414.

[97] A. Requate, A. Becker, F.H.M. Faisal, Phys. Rev. A 73 (2006) 033406.

[98] M. Protopapas, C.H. Keitel, P.L. Knight, Rep. Prog. Phys. 60 (1997) 389.

[99] H. Mineo, K. Nagaya, M. Hayashi, S.H. Lin, J. Phys. B: At Mol. Opt. Phys. 40 (2007) 2435.

[100] T. Remetter, P. Johnsson, J. Mauritsson, K. Varju, Y. Ni, et al., Nat. Phys. 2 (2006) 323.

[101] A.B. Saloman, C.J. Sansonetti, J. Phys. Chem. Ref. Data 33 (2004) 1113.

[102] T. Popmintchev, M.C. Chen, P. Arpin, M.M. Murnane, H.C. Kapteyn, Nat. Photon. 4 (2010) 822.

[103] T. Rumph, S. Bowyer, S. Vennes, Astron. J. 107 (1994) 2108.

[104] M. Sayrac, A.A. Kolomenskii, J. Strohaber, H.A. Schuessler, JOSA B 32 (2015) 2400.

[105] T. Sekikawa, T. Katsura, S. Miura, S. Watanabe, Phys. Rev. Lett. 88 (2002) 193902.

[106] P. Lee, G.L. Weissler, Phys. Rev. 99 (1955) 540.

[107] X. Wang, M. Chini, Y. Cheng, Y. Wu, X.M. Tong, et al., Phy. Rev. A 87 (2013) 063413.

[108] W. Boutu, S. Haessler, H. Merdji, P. Breger, G. Waters, et al., Nat. Phys. 4 (2008) 545.

[109] S. Haessler, J. Caillat, W. Boutu, C. Giovanetti-Teixeira, T. Ruchon, et al., Nat. Phys. 6 (2010) 200.

[110] K.B. Dinh, Faculty of Engineering and Industrial Sciences, Swinburne University of Technology Melbourne, Australia, Swinburne University of Technology Melbourne, Australia, (2012) 180.

[111] N. Hay, R. Velotta, M. Lein, R. de Nalda, E. Heesel, et al., Phy. Rev. A 65 (2002) 053805.

[112] M. Comstock, V.V. Lozovoy, M. Dantus, Chem. Phys. Lett. 372 (2003) 739.

[113] H. Stapelfeldt, T. Seideman, Rev. Mod. Phys. 75 (2003) 543.

[114] T.a.E.H. Seideman, Adv. At. Mol. Opt. Phy. 55 (2006) 289.

[115] J. Itatani, J. Levesque, D. Zeidler, H. Niikura, H. Pepin, et al., Nature 432 (2004) 867.

[116] S. Henrik, Physica Scripta 2004 (2004) 132.

[117] R.A. Bartels, T.C. Weinacht, N. Wagner, M. Baertschy, C.H. Greene, et al., Phy. Rev. A 88 (2001) 013903.

[118] R.J. Gordon, L. Zhu, W.A. Schroeder, T. Seideman, J. Appl. Phys. 94 (2003) 669.

[119] Y. Gao, C. Wu, N. Xu, G. Zeng, H. Jiang, et al., Phy. Rev. A 77 (2008) 043404.

[120] F. Rosca-Pruna, M.J.J. Vrakking, Physical Review Letters 87 (2001) 153902.

[121] B. Friedrich, D. Herschbach, Phy. Rev. Lett. 74 (1995) 4623.

[122] C.M. Dion, A. Keller, O. Atabek, A.D. Bandrauk, Phy. Rev. A 59 (1999) 1382.

[123] F.H.M. Faisal, A. Abdurrouf, Phys. Rev. Lett. 100 (2008) 1.

[124] J. Ortigoso, M. Rodríguez, M. Gupta, B. Friedrich, J. Chem. Phys. 110 (1999) 3870.

[125] V. Renard, M. Renard, S. Guérin, Y.T. Pashayan, B. Lavorel, et al., Phy. Rev. Lett. 90 (2003) 153601.

[126] H. Cai, J. Wu, A. Couairon, H. Zeng, Opt. Lett. 34 (2009) 827.

[127] B.H. Bransden, C.J. Joachain,Physics of Atoms and Molecules, Prentice Hall, Englewood Cliffs, (2003)

[128] D.A. McQuarrie, J.D. Simon,Physical Chemistry: A Molecular Approach, University Science Books, Sausalito, (1997)

[129] H. Li, W. Li, Y. Feng, J. Liu, H. Pan, et al., Phy. Rev. A 85 (2012) 052515.

[130] A.V. Veltheim, B. Borchers, G. Steinmeyer, H. Rottke, Phy. Rev. A 89 (2014) 023432.

[131] R. Torres, N. Kajumba, J.G. Underwood, J.S. Robinson, S. Baker, et al., Phy. Rev. Lett. 98 (2007) 203007.

[132] E. Goulielmakis, Z.-H. Loh, A. Wirth, R. Santra, N. Rohringer, et al., Nature 466 (2010) 739.

[133] K.H. Lee, S.B. Park, H. Singhal, C.H. Nam, Opt. Lett. 38 (2013) 1253.

[134] D.G. Lee, J.J. Park, J.H. Sung, C.H. Nam, Opt. Lett. 28 (2003) 480.

[135] R. Kienberger, M. Hentschel, M. Uiberacker, C. Spielmann, M. Kitzler, et al., Science 297 (2002) 1144.

[136] J. Seres, V.S. Yakovlev, E. Seres, C. Streli, P. Wobrauschek, et al., Nat. Phys. 3 (2007) 878.

[137] I.J. Kim, G.H. Lee, S.B. Park, Y.S. Lee, T.K. Kim, et al., Appl. Phys. Lett 92 (2008) 021125.

[138] G. Lambert, J. Gautier, C.P. Hauri, Z. Ph, C. Valentin, et al., New J. Phys. 11 (2009) 083033.

[139] N. Ben-Tal, N. Moiseyev, A. Beswick, J. Phys. B At. Mol. Opt. Phys. 26 (1993) 3017.

[140] D. Shafir, Y. Mairesse, D.M. Villeneuve, P.B. Corkum, N. Dudovich, Nat Phys 5 (2009) 412.

[141] Y. Zheng, Z. Zeng, P. Zou, L. Zhang, X. Li, et al., Phy. Rev. Lett. 103 (2009) 043904.

[142] X. Feng, S. Gilbertson, H. Mashiko, H. Wang, S.D. Khan, et al., Phy. Rev. Lett. 103 (2009) 183901.

[143] I.J. Kim, C.M. Kim, H.T. Kim, G.H. Lee, Y.S. Lee, et al., Phy. Rev. Lett. 94 (2005) 243901.

[144] Z. Chang, A. Rundquist, H. Wang, M.M. Murnane, H.C. Kapteyn, Phy. Rev. Lett. 79 (1997) 2967.

[145] T.T. Liu, T. Kanai, T. Sekikawa, S. Watanabe, Phy. Rev. A 73 (2006) 063823.

[146] J.T. Tate, P.T. Smith, Phys. Rev. 39 (1932) 270.

[147] L.-S. Wang, J.E. Reutt, Y.T. Lee, D.A. Shirley, J. Electron. Spectrosc. Relat. Phenom. 47 (1988) 167.

[148] C. Zhang, X. Liu, P. Ding, J. Appl. Math. Chem. 43 (2008) 1429.

[149] S. Long, W. Becker, J.K. McIver, Phy. Rev. A 52 (1995) 2262.

[150] B. Zhang, D.F. Gardner, M.H. Seaberg, E.h.R. Shanblatt, C.L. Porter, et al., Opt. Express 24 (2016) 18745.

[151] S.W. Hell, Science 316 (2007) 1153.

[152] C. Song, D. Ramunno-Johnson, Y. Nishino, Y. Kohmura, T. Ishikawa, et al., Phy. Rev. B 75 (2007) 012102.

[153] J. Miao, P. Charalambous, J. Kirz, D. Sayre, Nature 400 (1999) 342.

[154] G. Vaschenko, C. Brewer, F. Brizuela, Y. Wang, M.A. Larotonda, et al., Opt. Lett. 31 (2006) 1214.

[155] R.A. Bartels, A. Paul, H. Green, H.C. Kapteyn, M.M. Murnane, et al., Science 297 (2002) 376.

[156] C. Spielmann, N.H. Burnett, S. Sartania, R. Koppitsch, M. Schnürer, et al., Science 278 (1997) 661.

[157] X. Zhang, A.L. Lytle, T. Popmintchev, X. Zhou, H.C. Kapteyn, et al., Nat. Phys. 3 (2007) 270.

APPENDIX A

High Harmonic Generation Data Acquisition Flow Chart Program

HHG data acquisition program helps to optimize and also compare to XUV signal. It automatically saves the data in a folder named with current day's date. The analysis of data is much easier as background is already subtracted. M. Sayrac would like to acknowledge to Dr. S. Anumula for helping with writing of the LABVIEW program.

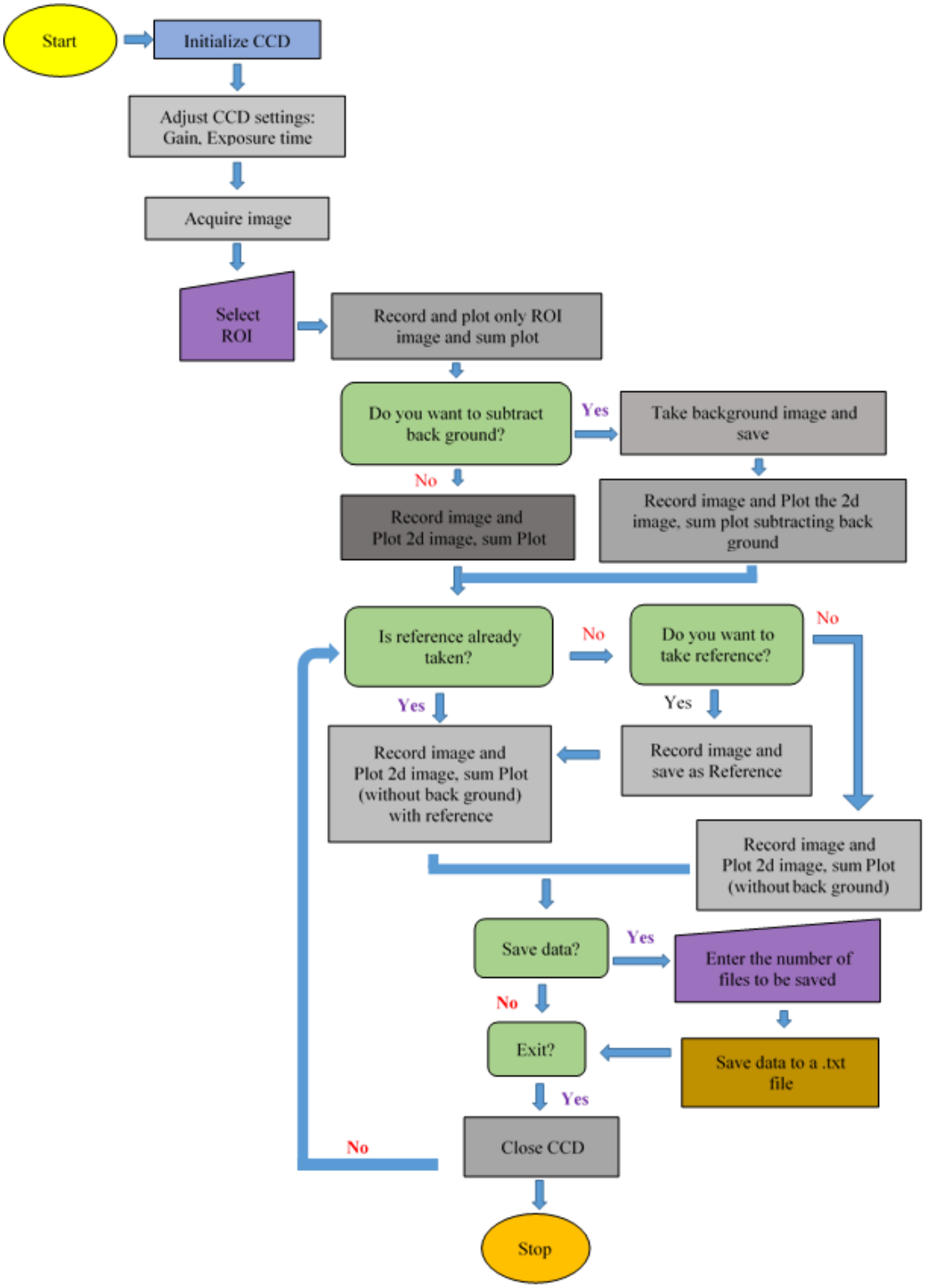
Start
Initialize CCD
Adjust CCD settings: Gain, Exposure time
Acquire image
Select ROI
Record and plot only ROI image and sum plot
Do you want to subtract back ground?
Yes
Take background image and save
No
Record image and Plot 2d image, sum Plot
Record image and Plot the 2d image, sum plot subtracting back ground
Is reference already taken?
No
Do you want to take reference?
No
Yes
Yes
Record image and Plot 2d image, sum Plot (without back ground) with reference
Record image and save as Reference
Record image and Plot 2d image, sum Plot (without back ground)
Save data?
Yes
Enter the number of files to be saved
No
Exit?
Save data to a .txt file
Yes
No
Close CCD
Stop

APPENDIX B

Rowland Circle Counter Reading (Fitting Position) of Harmonic Spectra Code

```
(*****************************************)
 (*Setting of the file directory*)

SetDirectory["C:\\Users\\sayrac\\Desktop"];

(*Initialization parameters, Rowland circle position, Rowland circle radius*)
POSITIONS=(5.3,5.0,5.5,6.0,6.5,7.0,7.5,8.0);(*Counter reading of Rowland circle*)
RRADIUS=998.8/2*0.03937; (*radius of Rowland circle (inch)*)
POSITIONSα=POSITIONS/RRADIUS;
TING=(1,1,1,1,1,1,1,1,1,1,1,1,1,1,1,1);
Initiali=1; LL=1.5; k=0; WAV40H=();

(*Diffraction order, incident angle, grating groove, initial wavelength, harmonic
position, counter distance*)
NN1=3; alf=87.6*π/180; dd=1000/133.6; lam=0.8;
Nmax=35; (*Maximum HH order*)
RR=998.9; (*Concave grating radius*)
HH=(); HH1=(); HHW=(); HHW1=(); (*Creating list array*)

(Label[SSS];
alf1=ArcSin[Sin[alf]-(lam/NN1/dd)]; (*Diffraction angle*)
xx=RR*ArcCos[Sin[alf]-lam/NN1/dd]/25.4; (*Distance (inches)*)
HH=Append[HH,(xx,NN1)]; (*Harmonic position*)
HH1=Append[HH1,(xx,LL)];
HHW=Append[HHW,(1000*lam/NN1,NN1)];
HHW1=Append[HHW1,(1000*lam/NN1,LL)]; (*Harmonic position combined*)
NN1=NN1+2;If[NN1<Nmax,Goto[SSS]];) (*Distance of McPherson*)

(*File name, converting .jpg image to its pixel values and 2D image dimensions*)
k=k+1;
NNAME=k-1;
NAME=ToString["0Ne-40H_t1sec_0.jpg"]; (*File name*)
G1 = Import[NAME];
Clear[NAME];
CHG1=ColorSeparate[G1]; G1Gr=CHG1[[1]];
LG1=ImageData[G1Gr]; DG1=ImageDimensions[G1Gr]; (*Image dimensions*)
D1=DG1[[2]]; D2=DG1[[1]];
```

```
(*Subtracting background for better signal to noise ratio*)
NAMEBACK=ToString["background_t1sec_0.jpg"]; (*Background file name*)
G1BACK = Import[NAMEBACK];
Clear[NAMEBACK];
CHG1BACK=ColorSeparate[G1BACK]; G1GrBACK=CHG1BACK[[1]];
LG1BACK=ImageData[G1GrBACK];
DG1BACK=ImageDimensions[G1GrBACK]; (*Background Image dimensions*)
D1BACK=DG1BACK[[2]]; D2BACK=DG1BACK[[1]];


(*Selection region of interest for 2D plot*)
NEWD2=1000; (*Maximum pixels along the x direction*)
CMIN=515; (*Minimum point for region of interest along y direction*)
CMAX=585; (*Maximum point for region of interest along y direction*)
NN=1;

(**************************)
(*Size of the MCP and finding HH position on the captured image, list of wavelengths*)
mcpsize=NEWD2/2;
y=Table[(40/25.4)*(950/NEWD2)*((i-mcpsize-6)/(NEWD2+1)),(i,1,NEWD2)];
x0=POSITIONS[[k]];
α1=ArcCos[x0/(2*(RR/2/25.4))];
α3=π/2- α1;
α2=ArcTan[y*Cos[α1]/(x0-y*Sin[α1])];
α4= α1+ α2;
x1=2*(RR/2/25.4)*Cos[α4];

(*2D Plot*)
ADX=Table[x1[[i]],(i,1,NEWD2)];
LAMHH=Table[N[NN*dd*(Sin[alf]-Cos[ADX[[NEWD2-
i]]*25.4/RR])],(i,1,NEWD2)];
(*Wavelength list corresponding to position of the counter reading*)

AMPL=(Table[Sum[LG1[[D1+1-i,j]],(i,CMIN,CMAX)],(j,227,227+NEWD2)]-
Table[Sum[LG1BACK[[D1BACK+1-i,j]],(i,CMIN,CMAX)],(j,227,227+NEWD2)]);
(*HH amplitude from the selected region of interest*)

WAV40H=Table[(LAMHH[[i]]*1000,AMPL[[i]]/TING[[k]]),(i,1,NEWD2)];

NGG40H=ListPlot[WAV40H, FrameLabel->("Wavelength (nm)","Intensity (arb.
unit)")]
(*Plotting final HH spectrum with subtracted background*)
```